

**MODELING AND DESIGN OF SINGLE
PHOTON AVALANCHE DIODES FOR
LIDAR APPLICATIONS**

**MODELING AND DESIGN OF SINGLE PHOTON
AVALANCHE DIODES FOR LIDAR
APPLICATIONS**

By

Xuanyu Qian

B.Eng. University of Electronic Science and Technology of China, 2021

A Thesis Submitted to the School of Graduate Studies in Partial Fulfillment of the
Requirements for the Degree of Master of Applied Science

McMaster University © Copyright by Xuanyu Qian, August. 2023

TITLE: Modeling and design of single-photon avalanche diodes
for LiDAR applications

AUTHOR: Xuanyu Qian,
B. Eng. University of Electronic Science and Technology
of China, Chengdu, China

SUPERVISOR: Prof. M. Jamal Deen

NUMBER OF PAGES: 144

Lay Abstract

Light detection and ranging (LiDAR) is a popular system that is widely used in the modern automotive industry. One crucial component within LiDAR systems is the Single-Photon Avalanche Diode (SPAD) due to their high sensitivity. Being able to combine with other circuit components, the SPADs can achieve continuous photon detections. In this thesis, the applications of SPADs in LiDAR systems are reviewed first. Then, SPAD models that are used to describe SPAD's performance are reviewed. Based on the discussion on SPAD's performance and SPAD models, a new SPAD modeling process is proposed in the article to have better simulation results. In addition to the simulation results based on the proposed models, SPADs are designed to validate the proposed model. The measured data has a good fit with the simulations, which indicates the improvement of the proposed SPAD models. Finally, research challenges and potential directions are summarized for future investigation.

Abstract

Single-photon avalanche diodes (SPADs) hold great potential as optical detectors in single-photon-counting (SPC) applications. With a primary focus on the fast-developing field of light detection and ranging (LiDAR) systems in automotive market, this thesis explores the important role of SPADs in achieving extended detection ranges, higher resolutions, and fast response times. As advanced complementary-metal-oxide-semiconductor (CMOS) technologies becomes more available, the cost-effective solutions of SPADs also become more achievable.

First, a detailed review of recent SPAD applications within LiDAR systems is presented. This discussion encompasses both commercial products and research works based on various CMOS technologies. SPADs fabricated using different technologies exhibit significant variations in the performances. Therefore, SPAD models that are used to simulate critical performances prior to fabrication are very important. Subsequently, a comprehensive review introduces the evolution of SPAD models, from key fundamentals to the modeling process. Based on the 65 nm standard CMOS technology and information from literature review, an enhanced SPAD modeling process is introduced. This model, considering a 2-D distribution of electric field, improves the accuracy of dark count rate (DCR) predictions. To validate its effectiveness, SPADs are meticulously designed using the TSMC 65 nm standard CMOS technology for the calibration and comparison purposes. Measured results indicate negligible afterpulsing probability ($\sim 0\%$) and decent DCR level (~ 14 kHz at a 0.7 V excess voltage), thanks to the implementation of output buffers. The measured wavelength dependence of photon detection probability (PDP) also agrees with the simulations. Additional discussions are conducted to figure out some deviations between simulations and measurements.

Finally, important research challenges are proposed based on the simulation and measurement results. Aiming to address these challenges, potential directions for optimizing SPAD models and design are presented, followed by conclusions.

ACKNOWLEDGEMENTS

I would like to express my greatest gratitude to Distinguished University Professor, Dr. M. Jamal Deen, for his unwavering support and guidance throughout my academic journey. I have been improving as a student and a researcher continuously influenced by his life philosophy.

Dr. M. Jamal Deen's profound understanding of fundamental physics and his approach to research have been instrumental in shaping my academic path. He has taught me the importance of grounding my work in foundational knowledge and how to effectively explain complex concepts in a scientific and logical manner. Under his mentorship, I have learned to approach research with a rigorous and systematic mindset.

I am always amazed by Dr. Deen's remarkable work efficiency. Whenever I submit a paper for Dr. Deen's feedback, Dr. Deen always gives me responses promptly, and with very detailed corrections. Especially, I am amazed that Dr. Deen can even notice the mistake of an extra space in a very long review paper. For every paper that I submit to Dr. Deen, he always reviews and revises them carefully. Being influenced by Dr. Deen's attitude and work efficiency, I also gradually improve myself, such as checking the references style, checking the spelling errors, checking the punctuation before finalizing any paper. Under Dr. Deen's supervision, I successfully published 4 papers during my master's study, which is way beyond my expectations. I really appreciate Dr. Deen's guidance and mentorship throughout my master's program.

In addition to the academic instructions, I am deeply influenced by Dr. Deen's life philosophy, particularly his perspective on education. Before, I thought becoming a professor would not be one of my options in the future since I think it is so boring. While my mind has changed upon witnessing Dr. Deen's remarkable example of what a professor can be. His model of a professor left an indelible impression on me, inspiring me to improve myself as a person. In this case, I try to improve my teaching skills and keep improving my attitude to everyone. And I believe that one day I can be someone like Dr. Deen, who always help others selflessly.

I would also like to express my appreciation to Dr. M. Jamal Deen, Dr. Chih-Hung (James) Chen, Dr. Jiang Wei, for their superb teaching and continuous support in the course ECE 742 Sensor technology, ECE 746 RF ICs for communications, and ECE 6EK4 Microelectronics.

I would express my great appreciation to Dr. Jiang Wei. Dr. Jiang has taught me a lot in academic learning and gives me many assistances in daily life. He is so kind to everyone. Sometimes I am affected by the low mood or stress, he always provides support to me whenever he is busy. I am so lucky that I have met such a good instructor, teacher, and a friend. Without his support in the research and daily life, I couldn't make many achievements in the course and papers.

In the research group, I have had a great experience working with Sophini, Subramaniam, Leo, Junzhi, Mahtab, Faisal, and many other members. They always offer their best attitude and willingness to help others.

Lastly, I am grateful that I have the best family in the world. My parents support my decisions all the time. During the two-year master's study, I couldn't spend time to take care of them, however, they always try to give their best to me. Without their love and encouragement, I would not be here today, pursuing my dreams. I would also like to express gratitude to myself for my enduring determination and continuous personal growth. My commitment to self-improvement drives me to strive for excellence and, ultimately, to contribute meaningfully to the society that has generously provided me with numerous opportunities and benefits.

LIST OF ABBREVIATIONS

ADAS	Advanced Driver-Assistance Systems
ADC	Analog to Digital Converters
AP	Afterpulsing Probability
AQR	Active Quench and Reset
APD	Avalanche Photodiode
ARC	Anti-Reflection Coating
AMCW	Amplitude-Modulated Continuous-Wave
BPF	Bandpass Filter
BV	Breakdown Voltage
BSI	Backside-Illuminated
BTBT	Band-to-Band Tunneling
CCD	Charge-Coupled Device
CIS	CMOS Image Sensor
CMOS	Complementary Metal-Oxide-Semiconductor
CMC	Canadian Microelectronics Corporation
dToF	Digital Time-of-Flight
DCR	Dark Count Rate
DNW	Deep N-Well
DSM	Deep Sub-Micron
FET	Field Effect Transistor
FoM	Figure-of-Merit
FWHM	Full-Width Half-Maximum
FMCW	Frequency-Modulated Continuous-Wave
FSI	Frontside-Illuminated
GND	Ground
GR	Generation-Recombination
IAT	Inter-Arrival Time
IC	Integrated Circuit
IMD	Inter-Metal-Dielectric
I-V	Current-Voltage
LIDAR	Light Detection and Ranging
LSB	Least Significant Bit
MCP	Microchannel Plate
MCS	Monte-Carlo Simulation
MOS	Metal-Oxide-Semiconductor
MOSFET	Metal-Oxide-Semiconductor Field-Effect Transistor
MPE	Maximum Permissible Energy
MEMS	Micro-Electro-Mechanical Systems
NIR	Near Infra-Red
ND	Neutral Density
NW	N-Well
PDP	Photon Detection Probability

PCB	Printed Circuit Board
PEB	Premature Edge Breakdown
PET	Positron Emission Tomography
PMT	Photo-multiplier Tube
PQ	Passive Quenching
PVT	Process Voltage Temperature
REF	Reference
SiPD	Silicon Photodiode
SPAD	Single Photon Avalanche Diode
SNR	Signal-to-Noise Ratio
SRH	Shockley-Read-Hall
STI	Shallow Trench Isolation
SPC	Single-Photon-Counting
TAT	Trap-Assisted Tunneling
TCSPC	Time Correlated Single Photon Counting
TDC	Time to Digital Converter
TG	Time Gated
TJ	Timing Jitter
ToF	Time of Flight
TCAD	Technology-Aided Design
VB	Valence Band
VCS	Voltage-Controlled Switches

Table of Contents

LAY ABSTRACT	III
ABSTRACT.....	IV
TABLE OF CONTENTS	IX
LIST OF FIGURES.....	XII
LIST OF TABLES	XV
CHAPTER 1 INTRODUCTION.....	1
1.1. MOTIVATIONS AND APPLICATIONS OF LIGH DETECTION AND RANGING	1
1.2. LIDAR PRINCIPLES	3
1.2.1. Non-Single-Photon-Counting LiDAR Architectures	4
1.2.2. Single-Photon-Counting LiDAR Architecture.....	7
1.3. OPTICAL SENSORS	10
1.3.1. Photomultiplier Tubes (PMTs)	10
1.3.2. APDs.....	11
1.3.3. SPADs.....	12
1.4. SPAD PERFORMANCE METRICS	14
1.4.1. Dark Count Rate (DCR).....	14
1.4.2. Afterpulsing Probability (AP).....	15
1.4.3. Photon Detection Probability (PDP).....	15
1.4.4. Timing Jitter (TJ)	16
1.4.5. Dead Time.....	17
1.5. SPAD MODELING	18
1.6. RESEARCH CONTRIBUTIONS	19
1.7. THESIS ORGANIZATION.....	21
CHAPTER 2 REVIEW OF SPADS IN LIDAR APPLICATIONS AND SPAD MODELS	24
2.1. RECENT PROGRESS OF SPAD AND APPLICATION IN LIDAR SYSTEMS.....	24
2.1.1. 2D SPAD Array & SiPM Array.....	27
2.2. SPAD MODELS – PRINCIPLES, PROGRESS, AND CHALLENGES	29
2.2.1. SPAD Operational Principles.....	30
2.2.2. DCR Models	32
2.2.3. PDP Models	35

2.2.4. Challenges for the SPAD Modeling.....	43
2.3. CONCLUSION	45
CHAPTER 3 CHARACTERIZATION AND SIMULATION OF SPADS.....	46
3.1. MODELING FUNDAMENTALS.....	47
3.1.1. Avalanche Triggering Probability.....	47
3.1.2. Dark Count Rate (DCR).....	49
3.1.3. Photon Detection Probability (PDP).....	52
3.2. DEVICE BUILDING.....	53
3.3. MESH SETTING.....	55
3.4. DEVICE SIMULATION.....	56
3.4.1. Physical Models.....	57
3.4.2. Breakdown Voltage (BV)	59
3.4.3. Avalanche Triggering Probability.....	62
3.4.4. Dark Count Rate (DCR).....	64
3.4.5. Photon Detection Probability (PDP).....	68
3.5. EXTEND FROM 1-D MODEL TO 2-D MODEL.....	70
3.6. AUTOMATED SIMULATION PROCESS.....	78
CHAPTER 4 DESIGN AND OPTIMIZATION OF CMOS SPADS AND CIRCUITS..	81
4.1. SPAD STRUCTURE DESIGN IN 65NM CMOS TECHNOLOGY.....	81
4.2. SPAD DESIGN	82
4.3. FRONT-END CIRCUIT DESIGN	85
4.3.1. Front-end Circuit Simulation	86
4.3.2. Output Buffers	90
4.3.3. Whole-chip Layout Design	92
4.4. MEASURED RESULTS AND DISCUSSIONS	93
4.4.1. Measurement Setup.....	93
4.4.2. Results and Discussions	94
4.5. CONCLUSION	98
CHAPTER 5 DESIGN AND MEASUREMENTS OF CMOS SPADS AND CIRCUITS	99
.....	99
5.1. PCB AND MEASUREMENT SETUP	99
5.2. MEASUREMENTS OF SPADS AND DISCUSSION	100
5.2.1. Breakdown Voltage (BV)	100

5.2.2. Dark Count Rate (DCR).....	102
5.2.3. Photon Detection Probability (PDP).....	108
5.3. SPAD's 2-D MODELING DISCUSSION	112
5.4. CONCLUSIONS	116
CHAPTER 6 CONCLUSIONS AND FUTURE WORK	118
6.1. CONCLUSIONS	118
6.2. FUTURE WORKS.....	121
REFERENCES.....	125
APPENDIX A COPYRIGHT PERMISSION	138
APPENDIX B CODES FOR SIMULATION AUTOMATION.....	141

List of Figures

Figure 1-1. Comparison among pulsed time-of-flight (ToF) LiDAR, amplitude amplitude-modulated continuous-wave (AMCW) LiDAR, and frequency-modulated continuous-wave (FMCW) LiDAR.	3
Figure 1-2. Waveforms of AMCW-modulated LiDAR.....	5
Figure 1-3. Waveforms of frequency-modulated continuous-wave (FMCW) LiDAR.	6
Figure 1-4. Operational principle of a pulsed time-of-flight LiDAR with flash and scanning configurations, (MEMs): micro-electro-mechanical system; (OPA): optical phase array.	8
Figure 1-5. Current-voltage characteristic of APD and SPAD.....	13
Figure 1-6. Schematic of biasing-temporal response relation, (BV): breakdown voltage; (FWHM): full-width-at-half-maximum.....	17
Figure 2-1. SPAD/SiPM array's relation to the image resolution.	28
Figure 2-2. (a) Simple SPAD diagram (b) Current-voltage (I-V) characteristics	31
Figure 2-3. SPAD models graphical diagram with process-related parameters	32
Figure 2-4. Four major mechanisms of DCR in SPADs.....	33
Figure 2-5. Summary of future research perspectives and potential outcomes	43
Figure 2-6. Realistic structure of SPAD based on TSMC 65 nm Standard CMOS technology (a) Layout view (top view) (b) Cross-sectional view of the design.	44
Figure 3-1. Triggering probability diagram. Creative commons License.	48
Figure 3-2. Structure of (a) Simple PN junction (b) Realistic SPAD structure.....	54
Figure 3-3. Mesh refinement for accurate avalanche simulation.....	55
Figure 3-4. Contact definition in SDEVICE.....	56
Figure 3-5. SPAD device details used for simulating breakdown voltage.	60
Figure 3-6. Simulated reverse I-V of SPAD.....	61
Figure 3-7. Simulated Electric Field of SPAD with a 10-V biasing voltage.	62
Figure 3-8. Specification of (a) depletion region's width and (b) electron ionization coefficient.	63
Figure 3-9. Simulated avalanche triggering probability in the depletion region.	64
Figure 3-10. Simulated SRH generation rate across the depletion region.....	65
Figure 3-11. Simulated BTBT generation rate across the depletion region	65

Figure 3-12. Comparison between SRH generation rate and the field enhanced SRH generation rate	67
Figure 3-13. Simulated DCR voltage dependence of SPAD based on initial BV of 9.45 V	68
Figure 3-14. Simulated Photon absorption rate of different wavelengths	70
Figure 3-15. 25 Streamlines created in the 2-D SPAD model.....	71
Figure 3-16. Avalanche triggering probability P_t of different streamlines of a 10- μ m-diameter SPAD at 10.5 V bias.....	72
Figure 3-17. (a) Dark count rate of each streamline and (b) Photon detection probability of each streamline of a 10- μ m-diameter SPAD at 10.5 V bias.....	73
Figure 3-18. 5 SPAD with diameter of 6 μ m, 10 μ m, 12 μ m, 16 μ m, 20 μ m.....	74
Figure 3-19. Original axis and normalized axis for plotting DCR versus position. ...	74
Figure 3-20. The simulated normalized DCR of 5 SPADs at 10.55 V bias	75
Figure 3-21. Photon detection probability of different streamlines of a 5 SPADs at 10.55 V bias and wavelength of 400 nm.	76
Figure 3-22. Normalized DCR of different SPADs.....	77
Figure 3-23. Normalized PDP of different SPADs.....	77
Figure 3-24. Proposed automated simulation process of 2-D SPAD model.....	79
Figure 4-1. Layout design of a single SPAD (a) N-well regions; (b) N ⁺ and P ⁺ regions; (c) Metal 1 and contacts.....	83
Figure 4-2. Special layers designed for SPADs: (a) Block layer M5; (b) Special layers RH and RPO.	84
Figure 4-3. Simplified cross-sectional illustration and the complete layout of a 10- μ m diameter SPAD.	85
Figure 4-4. Two PQR circuits that have positive original output pulses: (a) Output at cathode; (b) Output at anode.....	86
Figure 4-5. Schematic of SPAD SPICE model.....	87
Figure 4-6. Operating principles of the designed SPICE schematic.....	88
Figure 4-7. Simulated results of the SPICE model: (a) Single pulse waveform; (b) I-V curve.	89
Figure 4-8. Simulated results of the SPICE model: (a) SPICE schematic; (b) Single pulse with 15-pF load capacitor.....	91
Figure 4-9. Simulated waveforms of incident photon, original output, and output of the output buffer (From top to the bottom).....	92
Figure 4-10. Complete layouts of 5 SPADs, 5 output buffers, and dummy layers (Top); Connections and pins (Bottom).	93

Figure 4-11. Measurement setup and expected results for SPAD' single output pulse and I-V characteristics under illumination.	94
Figure 4-12. Comparison between simulation and measurements of avalanching current	95
Figure 4-13. Comparison of measured I-V between 3 SPAD with different sizes of active region.....	96
Figure 5-1. Breakdown voltage (BV) and dark count rate (DCR) measurement setup.	100
Figure 5-2. Comparison between the simulation and measurement of breakdown voltage.....	101
Figure 5-3. Definition of inter-arrival-time and ideal distribution	103
Figure 5-4. Inter-arrival-time plot of a 10- μ m-diameter SPAD at 0.7 V excess voltage	104
Figure 5-5. Inter-arrival-time plot of a 10- μ m-diameter SPAD at (a) 0.9 V excess voltage; (b) 1 V excess voltage.....	106
Figure 5-6. Comparison between simulated DCR and measured DCR of a 10- μ m-diameter SPAD	107
Figure 5-7. Diagram that explains the sudden drop of DCR at small biasing voltages	108
Figure 5-8. Photon-detection-probability (PDP) measurement setup.....	109
Figure 5-9. Comparison between simulated PDP and measured PDP at 0.5 V biasing voltage.....	111
Figure 5-10. Measured PDP at three different biasing voltages: (blue) $V_{ex}=0.5$ V, (red) $V_{ex}=0.6$ V, orange (0.7 V).	112
Figure 5-11. Comparison among 1-D DCR, 2-D DCR, and measured data.....	113
Figure 5-12. Comparison of normalized DCR of 5 SPADs based on measured data	114
Figure 5-13. Measured PDP at 10.75 V biasing voltage, 680-nm incident light with different intensity.....	115
Figure 6-1. Simulation of time window at two different temperatures.....	122
Figure 6-2. Layout and the micrograph of the designed SPAD array.	122
Figure 6-3. An example of (a) Cross-sectional view and (b) SEM image of a BSI SPAD [47], Copyright © 2022, <i>IEEE</i>	123

List of Tables

Table 1-1. Examples of Commercial LiDAR Products	9
Table 1-2. Comparison among common optical sensors in LiDAR.....	14
Table 2-1. Recent Progress of SPAD Detectors and Important Performance Metrics	25
Table 2-2. DCR Models	33
Table 2-3. Commonly Used Ionization Coefficient Models in Sentaurus [108]	37
Table 2-4. PDP Models.....	40
Table 3-1. Parameters used for Modeling Minority Carrier Lifetime	51
Table 3-2. Basic Parameters for Silicon Material.....	58
Table 3-3. Default values for okuto-crowell model.....	59
Table 3-4. Some Initial Parameters for the 1-D SPAD Simulation	60
Table 5-1. Basic Parameters used in the Simulation of BV.....	102
Table 5-2. Comparison of SPAD's performances	116

Chapter 1

INTRODUCTION

1.1. Motivations and Applications of Light Detection and Ranging

Distance sensing systems widely used in vehicles are important, as they need to provide accurate and reliable raw data for decision-making. Various distance sensing systems can fulfill different roles in autonomous vehicles, including adaptive cruise control, localization, navigation, automatic braking systems, and parking assistance [1]. Numerous investigations have been explored in various sensing systems, such as stereo cameras, radar systems, ultrasonic systems, and light detection and ranging (LiDAR) systems. When considering the application of autonomous vehicles, radar systems demonstrate exceptional ability in detecting long-range objects with minimal interference caused by dust, fog, or other adverse weather conditions. However, radar systems also possess disadvantages, such as limited spatial resolution and bulky size. Ultrasonic sensing systems can detect objects within the sub-meters range to prevent collision [2]. These systems can detect the range between vehicles and objects by measuring the time delay between the emission and reflection of the ultrasonic waves. Nevertheless, due to the limited velocity of the acoustic signal in air, they cannot be employed for long-distance sensing in autonomous vehicles moving at very high speeds. In comparison to radar systems and ultrasonic sensing systems, LiDAR systems can achieve high accuracy and wide detection range while maintaining high reliability. Consequently, LiDAR systems are commonly used in autonomous vehicles for collision avoidance and active braking systems [3].

Adapted from X. Qian, W. Jiang, A. Elsharabasy, and M. J. Deen, "Modeling for Single-Photon Avalanche Diodes: State-of-the-Art and Research Challenges," *Sensors* 2023, vol. 23, no. 7, p. 3412, Mar. 2023, doi: 10.3390/S23073412. (Appendix A)

The advancement in algorithm development and the evolution of communication techniques have significantly increased the popularity of LiDAR systems in their applications for autonomous vehicles. More specifically, algorithms used to process raw data from LiDAR systems can enhance visualization quality and predictions, while the high-bandwidth communication technology makes the transmission of large-volume data feasible. Relying on accurate images from LiDAR systems, the localization and navigation of autonomous vehicles become both simpler and more reliable [4]–[11]. Despite the research focus on various algorithms for feature extraction and optimization, the parameters of optical sensors and circuits have the most direct influence on the overall performance of LiDAR systems, affecting factors such as detection range, distance resolution, image resolution, and frame rate. In particular, the development of advanced complementary metal-oxide-semiconductor (CMOS) technologies has reduced the cost of high-performance LiDAR systems in autonomous vehicles.

CMOS-based LiDAR systems have attracted a lot of research interests. For instance, an in-depth review of LiDAR architectures was provided in [12]. Micro-electro-mechanical system (MEMS) structures employed in LiDAR were discussed in [13]. Recent advancements in nanophotonic-based systems were discussed in [14]. For the visualization fusion in LiDAR, several comprehensive summaries have been presented in [10], [11]. The study of the detectors' material is detailed in [15].

With the development of the LiDAR systems in the automotive industry, single-photon detection techniques are becoming increasingly important. Three prevalent LiDAR architectures have been applied widely: pulsed time-of-flight (ToF) LiDAR, amplitude-modulated continuous-wave (AMCW) LiDAR, and frequency-modulated continuous-wave (FMCW) LiDAR. In Figure. 1-1, a comparison of the three different LiDAR architectures illustrates the differences in their detection range.

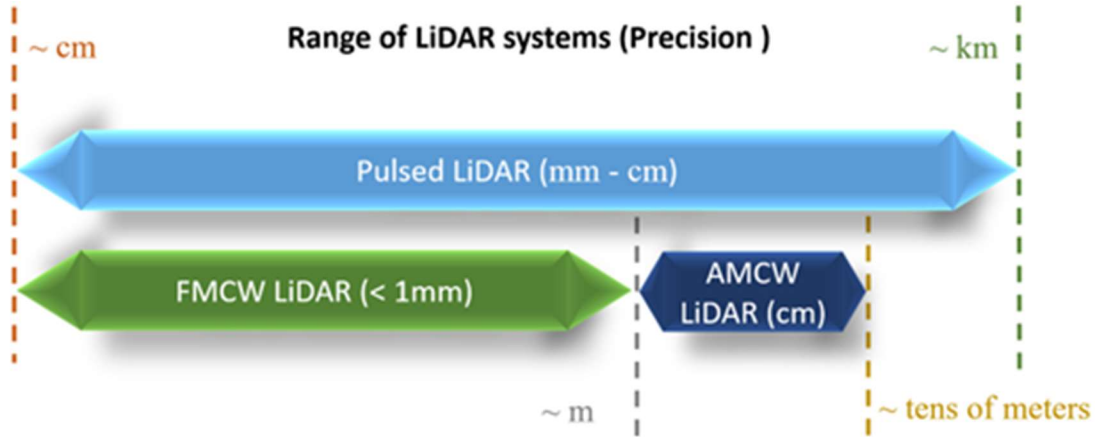


Figure 1-1. Comparison among pulsed time-of-flight (ToF) LiDAR, amplitude amplitude-modulated continuous-wave (AMCW) LiDAR, and frequency-modulated continuous-wave (FMCW) LiDAR.

Among these architectures, pulsed ToF LiDAR has the advantages of low-cost, extensive detection range, and decent spatial resolution. More importantly, pulsed ToF LiDAR can achieve detection down to single photon level through the implementation of single-photon detectors like SPADs.

1.2. LiDAR Principles

In comparison to traditional cameras, radar, and ultrasonic devices, LiDAR systems have the capability to capture precise distance information and achieve a wide detection range, depending on the employed configuration. The detection distance of a LiDAR system in autonomous vehicles can cover the range from centimeters to hundreds of meters, and even kilometers [12]. For each type of the LiDAR configurations, there are different architectures, principles, performance metrics and fabrication cost. Therefore, it is necessary to understand the configuration before discussing single photon detectors in LiDAR systems. Generally, three different modulated LiDAR systems are used for automotive applications: pulsed time-of-flight (ToF) LiDAR, amplitude-modulated continuous wave (AMCW) LiDAR and frequency-modulated continuous wave (FMCW) LiDAR. A detailed comparison of these three configurations is discussed in [12]. Currently, all LiDAR systems utilize

actively emitted signals to achieve detection, and they can be characterized into two sub-systems: transmitting stage and receiving stage.

In general, a higher transmitting power translates into a higher probability that optical sensors can detect the reflected signals, thus achieving a longer detection range. However, the maximum transmitting power is limited by the laser source and eye-safety regulations [12]. The power requirements are different for different configurations and lasers used in the system. This is because laser-induced injuries are dependent on the total energy absorbed by the eye's tissue, and the total energy is related to the energy of the photons and the illumination duration. In this case, for laser with different wavelengths, this time duration may vary [16], [17]. In an early experiment conducted on monkeys, a pulse at a 580 nm wavelength with a 600-fs pulse duration caused small foci of retinal pigment epithelium and retinal disruption [16]. For human eyes, there are different pulse durations for different light sources that can cause a threshold lesion [16]. For LiDAR applications, most of the lasers used are in Class 1, which has a transmitted power less than 0.39 MW. According to [18], the maximum permissible exposure (MPE) is $5 \times 10^{-7} \text{ J/cm}^2$ in the 520-530 nm range. The laser energy is limited by the standard IEC 60825 [19]. If the pulse is repetitive, then the MPE must be reduced by the factor of $N^{-0.25}$, where N is the total number of the pulses. For example, for visible light, the exposure is limited to 0.25 seconds, or converted to 1250 pulses at a fixed 5 kHz pulse repetitive frequency. In real cases, the MPE is also dependent on the laser beam motion, divergence of the light, and the beam diameter.

1.2.1. Non-Single-Photon-Counting LiDAR Architectures

An amplitude-modulated continuous-wave (AMCW) LiDAR can achieve continuous detection. AMCW LiDAR systems detect modulated light intensity. However, in contrast to pulsed LiDAR systems, the emitted light signal is a continuous wave with varying amplitudes. The peak power of the light signal in AMCW LiDAR systems is usually smaller than the pulsed ToF LiDAR, due to the average power constraint for eye-safety [12], [14]. Therefore, the maximum detection range of an AMCW LiDAR is less than that of the pulsed LiDAR system. Due to the delay, the detected signals usually have a phase shift compared to the emitted signals. In this case, the time delay cannot be directly measured, but it is calculated according to the phase

difference. An illustration of the AMCW LiDAR timing response is shown in Figure. 1-2.

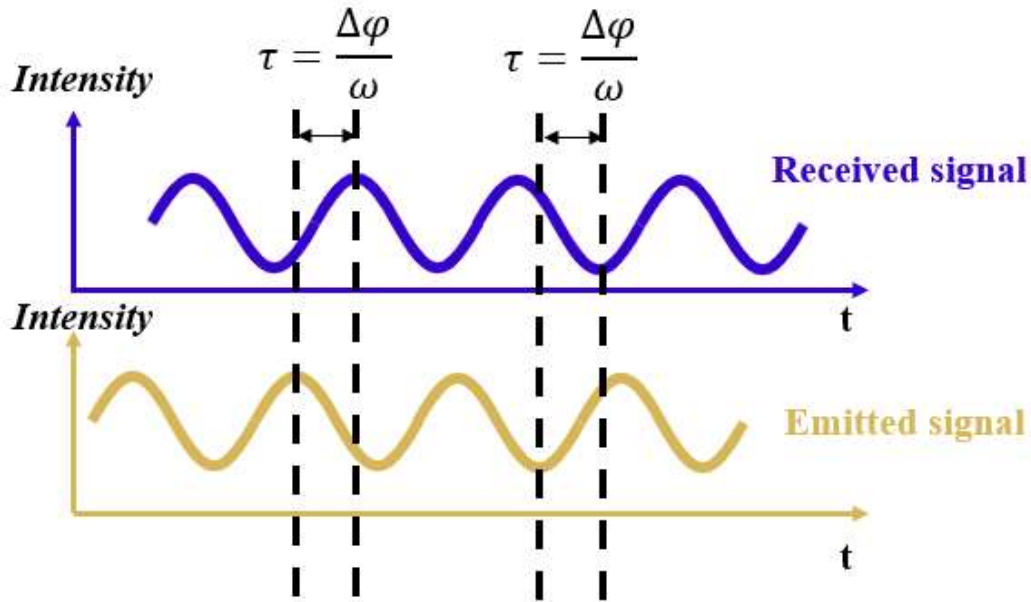


Figure 1-2. Waveforms of AMCW-modulated LiDAR

If the frequency of the modulated light signal is fixed to be f , and the detected phase difference between the transmitted signal and the received signal is $\Delta\phi$, then the distance can be calculated according to Eq. 1-1 [14]

$$D = c \times \frac{\tau}{2} = c \times \frac{\Delta\phi}{2 \times \omega} = c \times \frac{\Delta\phi}{4\pi f}. \quad 1-1$$

In the equation, τ refers to the time of flight. $\Delta\phi$ and f are the detected phase difference and frequency of the modulated signal, respectively. By correlating the reference signal with the backscattered signal, it is possible to measure the ToF by varying the phase of the reference signal. The typical value of the frequency used is 10-100 MHz, depending on the specific applications scenarios [20]. The equations used for comparing the three different modulation techniques are only for ideal cases. However, in real cases, there are more complicated conditions, such as interference, crosstalk, and background noise. These factors must be considered in the real implementation of the techniques.

Frequency-modulated continuous-wave (FMCW) LiDAR achieves detection by modulating the frequency of the light signal. The detected signals will be compared with reference signals. In this way, the distance can be calculated indirectly. A simple illustration of FMCW LiDAR and its timing response is shown in Figure. 1-3. where

the term Δf is the frequency difference between the reference signal and the received signal at a specific time.

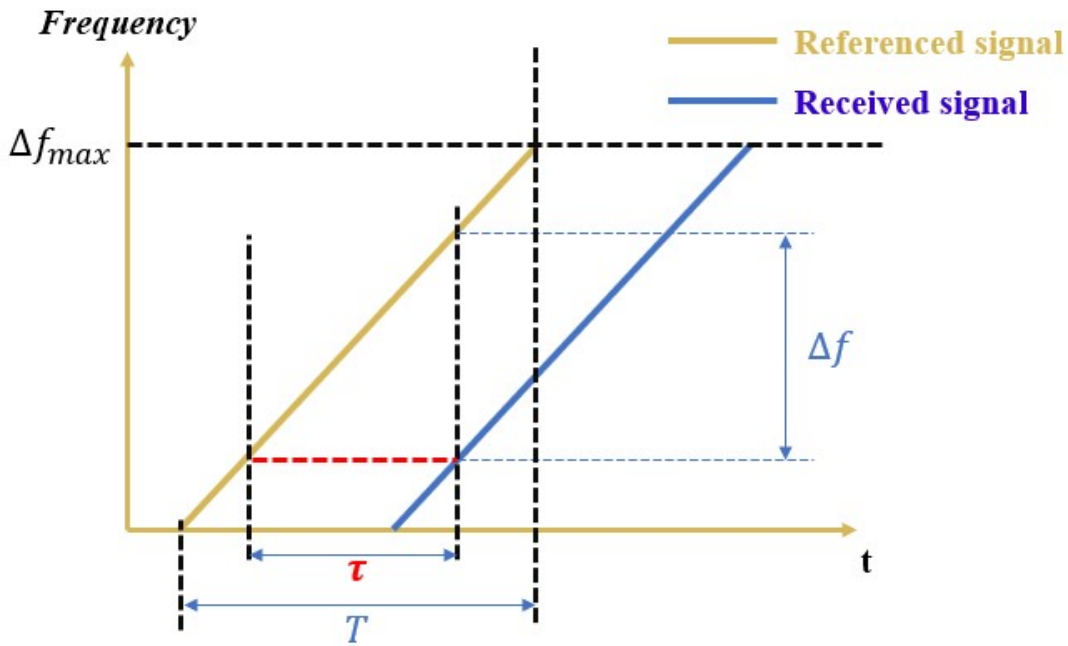


Figure 1-3. Waveforms of frequency-modulated continuous-wave (FMCW) LiDAR.

The distance calculation of the system can be expressed in Eq. 1-2 [12].

$$D = c \times \frac{\tau}{2} = c \times \frac{\Delta f \times T}{2 \times \Delta f_{max}}. \quad 1-2$$

In this equation, the time difference between the two signals is calculated using frequency difference Δf and the rate of frequency change $\frac{\Delta f_{max}}{T}$. Note that the equation does not consider the Doppler effect. However, the Doppler effect must be considered for distance accuracy in autonomous vehicles. Compared to pulsed LiDAR and AMCW LiDAR, FMCW LiDAR has the strongest ability to suppress interference from ambient light due to its ability to amplify the signal before the detection [12]. One of the limitations of FMCW LiDAR systems is the detection range, as seen in the Figure. 1-1; most of them cannot exceed a few hundred meters of detection range due to the strict power requirements. Therefore, FMCW LiDAR is suitable to detect objects close to vehicles for applications such as parking assistance. There are some recently proposed mixed-iToF-dToF LiDAR systems to combine both FMCW LiDAR and pulsed LiDAR for high maximum detection range and improved accuracy at short range [21], [22].

FMCW LiDAR is more accurate than the commonly used ultrasonic sensor for parking assistance, as it has faster response time, a lower air attenuation, and longer range [23].

1.2.2. Single-Photon-Counting LiDAR Architecture

A pulsed ToF LiDAR sends discrete modulated light pulses. Optical signals are emitted from lasers in the form of pulses with specific time durations. The emitted photons then travel until being reflected by objects after diffusing through optics. Upon detecting the reflected photons, the time difference between emission and detection can be recorded to calculate the distance between the car and objects. Pulsed ToF LiDAR is widely used due to its simple mechanisms, reasonable detection range, and good precision, compared to other continuous wave-modulated LiDAR systems [12]. In pulsed ToF LiDAR, time-to-digital converters (TDCs) are commonly used to timestamp the effective outputs from optical sensors. Then, the recorded time delay between the emission and detection can be used to calculate the distance by assuming a constant and uniform light velocity in the air. For LiDAR systems in autonomous vehicles, this velocity is 3×10^8 m/s. A typical pulsed ToF LiDAR system is illustrated in Figure. 1-4. It consists of a flash-pulsed LiDAR system and a scanning pulsed LiDAR system. For a flash-pulsed LiDAR system, the whole target view is illuminated at one time, while the scanning-pulsed LiDAR relies on mechanical structures or optical phase arrays (OPAs) to direct the light beam. During detection, the laser generates short-duration pulses with pulse widths ranging from less than a nanosecond to tens of nanoseconds [12], [24], [25].

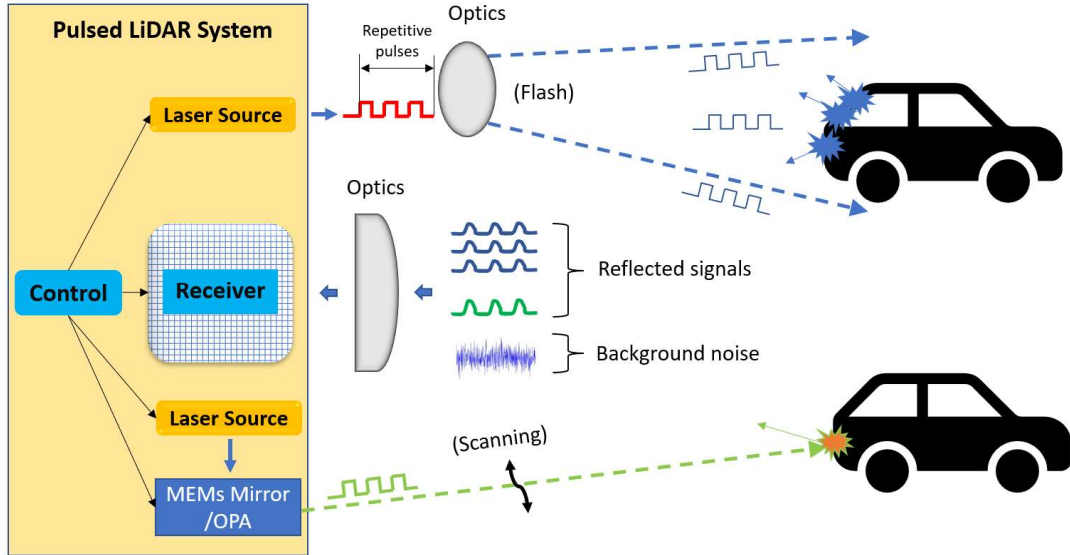


Figure 1-4. Operational principle of a pulsed time-of-flight LiDAR with flash and scanning configurations, (MEMs): micro-electro-mechanical system; (OPA): optical phase array.

The pulse width of the laser can affect the range or distance resolution of the sensing system. By reducing the pulse width, the bandwidth of the pulse is increased, thus decreasing the minimum distinguishable distance between different objects (improved distance resolution) [12]. The pulse repetition rate is also an important factor that affects accuracy. A higher pulse repetition rate can potentially reduce range ambiguity if the limitations of detectors are not considered. However, as mentioned in the power limitation discussion, the power of the laser pulse should be reduced when the repetition rate increases due to the limitation of the total power. Also, the repetition rate depends on the LiDAR configuration. For a flash LiDAR, the pulse repetition rate can be simply set to be the same as or higher than the required frame rate of the whole system. For a scanning LiDAR, such a repetition rate may be significantly higher than that of the flash LiDAR, depending on the number of scanned pixels [26]. The distance can be simply calculated using Eq. 1-3,

$$D = \frac{c \times \tau}{2}, \quad 1-3$$

where the D represents the distance from the vehicle to the object, τ stands for the time of flight, and the c is the light speed in the air. In a pulsed LiDAR system, all photons are emitted during a short time duration in each detection period, and the farther the distance, the fewer photons the detectors will receive. Therefore, there is a compromise

among illumination area, maximum detection range, laser power, and detector sensitivity. Pulsed LiDAR systems can achieve a longer detection range over other LiDAR systems because a higher peak power of the laser can be utilized [12], [14]. In addition, when pulsed LiDAR systems are employed to detect moving objects, multiple detections are required [19]. In automotive LiDAR applications, around 50 to 100 measurements are necessary for a single frame to reduce the influence of noise, thus improving the accuracy [26].

The dToF LiDAR has advantages in terms of cost, simplicity, and detection range, it is commonly adopted in the commercial LiDAR systems for automotive applications. If the sensors used in the dToF LiDAR system are detectors that have very high sensitivity, the LiDAR system can be described as a single-photon-counting (SPC) LiDAR. From Table 1-1, some examples of commercial products from various manufacturers are briefly introduced [27]–[32].

Manufacturer	Product Example	Release Date	Key features	Other
Elmos [27]	16 channel scanning LiDAR	2020	Range: 192 m Resolution: 3 mm Frame rate: 30 fps (@ 905 nm)	(dToF)
MAVIN [28]	DS0140020 Rev B MAVIN	2023	Range: > 220 m Frame rate: 30 fps (@ 905 nm)	Dynamic FOV
Innoviz [29]	Innoviz One	2023	Range: 250 m Frame rate: 10/20 fps (@ 905 nm)	(dToF)
	Innoviz Two	unknown	Range: 300 m Frame rate: 10/15/20 fps	(dToF)
	Innoviz 360	unknown	Range: 300 m Frame rate: 0.5-25 fps	(dToF)
Velodyne [30]	Puck	2019	Range: 100 m Accuracy: 3 cm Frame rate: 5-20 fps (@ 903 nm)	16 channels 360° horizontal
	Ultra Puck	2019	Range: 200 m Accuracy: 3 cm Frame rate: 5-20 fps (@ 903 nm)	32 channels 360° horizontal
	Alpha Prime	2019	Range: 245 m Accuracy: 3 cm Frame rate: 5-20 fps (@ 903 nm)	128 channels 360° horizontal
Sony [31]	IMX459 597×168 SPAD Array	2022	Range: 300 m Precision: 15/30 cm (@ 905 nm)	(dToF)
ams-Osram [32]	TMF 8801/8805	unknown	Range: 2.5 m (@ 940 nm)	Not for automotive application (dToF)
	TMF 8820/8821/8828	unknown	Range: 5 m (@ 940 nm)	

Most of the automotive LiDAR products have a detection range > 100 m, which is important for advanced driver-assistance system (ADAS) and autonomous driving. From the table of commercial products, dToF LiDAR systems that are based on pulsed detection technology have shown a dominant popularity. Therefore, the investigation on the optical sensors used in the dToF LiDAR systems is of great significance.

1.3. Optical Sensors

Optical sensors detect the light reflected by various objects. Once the emitted laser power and the LiDAR configuration are determined, important performance parameters of LiDAR systems, such as resolution and detection range, become significantly influenced by the optical detector's capabilities. To improve the overall system performance, selecting and designing suitable optical sensors is of necessity. In typical LiDAR systems, several different types of optical sensors are used, including photomultiplier tubes (PMTs), avalanche photodiodes (APDs), and single-photon avalanche diodes (SPADs). The general requirements for ideal optical detectors include high sensitivity, low dark noise, compact size, and low cost. However, different types of optical sensors may have their own advantages and disadvantages. In this section, detailed discussions among these three optical sensors are presented.

1.3.1. Photomultiplier Tubes (PMTs)

PMTs can serve as optical detectors in LiDAR applications because they possess high gain and speed characteristics. A typical PMT sensor consists of a photocathode, an anode, a vacuum channel, and a series of dynodes. When a photon is absorbed at the photocathode, electrons are generated due to the photoelectric effect. These generated electrons then get accelerated and energized by the high electric field between the photocathode and the first dynode. When the energized electrons hit the dynode, more electrons are generated, which are called secondary electrons [33]. After that, the newly generated secondary electrons will undergo another acceleration and generation process, achieving a sequentially amplified signal. Finally, a large current can be detected at the anode of the PMTs. The outputs of PMTs are analog pulses with varying amplitude, which means a discriminator circuit is needed to convert these original outputs. Due to a multi-stage ionization path in PMTs, the histogram of the effective

output pulse is usually wider than the output pulses of a SPAD, which has a much shorter acceleration path. Therefore, it is easier to have pileups in a PMT-based system due to the overlaps of consecutive output pulses [34], [35].

In addition to the conventional PMTs, micro-channel plate PMTs (MCP-PMTs) are used in some LiDAR applications [36], [37]. Different from the series of plates used in the conventional PMTs, MCP-PMTs have multiple micro-channels to achieve electron multiplication. Both conventional PMTs and MCP-PMTs require a vacuum environment, which results in reduced dark counts, with the penalty of increased cost and size [33], [37]. Additionally, a magnetic shield may be needed for PMTs so the electrons traveling in the vacuum tube will not be affected by the magnetic field. In particular, when PMTs are used in applications where a strong magnetic field exists, such as in a positron emission tomography (PET) system, a magnetic shield is necessary. In LiDAR applications, the earth magnetic field (around 50 μT) is much smaller than in a clinical PET-CT medical system, but further investigations are needed on whether a shield is necessary for PMTs in automotive LiDAR applications. These disadvantages have limited the PMT's use in LiDAR systems, especially when high integration is required.

1.3.2. APDs

APDs are photodiodes that work in the reverse-biased region. Normally, when diodes are reverse biased below their breakdown voltages, the barrier between the n-type region and p-type region is high so that carriers are unable to flow. In this case, only a small reverse current which is called the dark current exists. When the reverse voltage increases, the current of APDs will increase with a near-linear relation to the voltage. When incident photons are absorbed by the APDs, photon-generated carriers will move under the influence of the high electric field and gain energy. Once carriers have gained enough energy, they are called energized carriers [38]. These energized carriers can ionize bound electrons and generate more carriers, without the need of dynodes. Finally, a chain of impact ionization events occurs. And this is the reason why the name “avalanche” is used for such detectors.

Due to the avalanche process in APDs, the current will be amplified after the detection of photons, without the need for external amplifiers. Compared to PMTs,

APDs can save a lot of space since they do not need a vacuum environment or a series of dynodes. High internal gain and compact size of an APD makes it an ideal candidate as a detector in LiDAR systems.

In modern ToF-based LiDAR systems for autonomous vehicles, it is important to improve the speed of detection, especially when multiple wavelengths are used. In this case, multi-channel APDs can be utilized for optimized speed and throughput. For example, a 12-channel APD array is utilized to achieve detection at different wavelengths, and the number of channels can be adjusted as needed [39]. Furthermore, APDs can be implemented in arrays for LiDAR applications where 3-D imaging is required, such as autonomous vehicles [40].

Limitations of APDs include their analog output signal and moderate sensitivity. Due to the linear operating mode, the output of the APD is with respect to the number of detected photons. Therefore, for signal processing in the following stages, analog-to-digital converters (ADCs) are needed. Moreover, the intrinsic layers in APDs for an expanded photon absorption may not be available in some standard CMOS technologies. In [41], the APD-based LiDAR and the silicon photomultipliers (SiPM)-based LiDAR were compared in both indoor and outdoor environments. The comparison indicated a shorter detection range of APDs. An APD array with Ge-on-Si technology was fabricated to reduce the cost of conventional APDs with III-V materials [42].

1.3.3. SPADs

Similar to APDs, SPADs are reverse-biased diodes, but are working above the breakdown voltage. When the applied reverse voltage across the SPAD's junction is greater than the breakdown voltage, the operation mode is called the Geiger mode, in comparison with the linear operation mode in APDs [43].

In the Geiger mode, the avalanche current increases rapidly with the increase of biasing voltage. Therefore, the effective outputs of a typical SPAD are more like digital pulses instead of the linear current-voltage response of APDs. A simple current-voltage (I-V) characteristic of SPAD and APD are shown in Figure. 1-5.

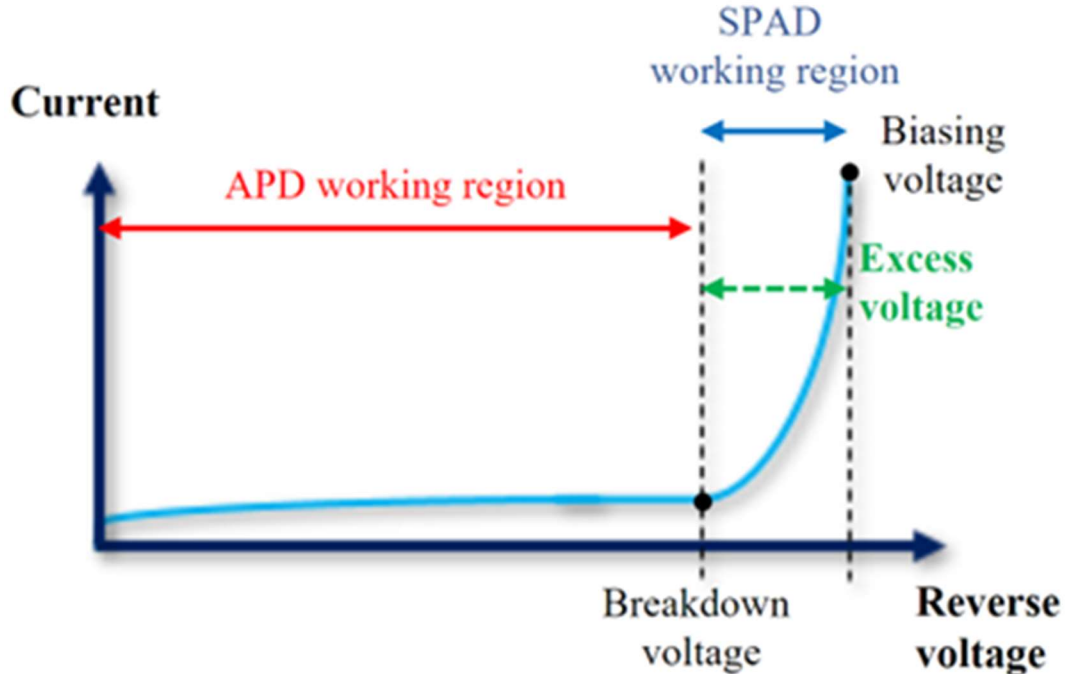


Figure 1-5. Current-voltage characteristic of APD and SPAD

Typically, SPADs are biased above the breakdown voltage, the difference between this biasing voltage and the breakdown voltage is called the excess voltage. So, there is no big difference between an APD and a SPAD's actual structure [44]–[47]. Due to the heating effect of the very large avalanche current, SPADs need to be quenched timely by reducing the reverse voltage below the breakdown voltage to suspend the avalanche quickly. After a certain dead time (quench, reset, and hold-off time), the SPADs will be reset, being ready for the next photon detection. The quench and reset time for AQR SPAD and time-gated SPAD are almost not reconfigurable [48]–[50]. However, the hold-off time can be adjusted for the balance between DCR and detection rate but is only achievable with certain hold-off circuit [51].

It is easy to achieve high integration using SPADs due to their compact size and high sensitivity. Moreover, the intrinsic digital property of SPADs makes it possible to remove ADCs in a LiDAR system, which are required in the APD-based and PMT-based detectors. Regarding the application in LiDAR systems, several important parameters of SPADs are crucial to the performance of the whole system. They include dark count rate (DCR), photon detection probability (PDP), timing jitter (TJ), area, and pixel numbers. Reviews of SPADs, SPAD design issues and SPAD models can be found in [52]–[55].

Based on the discussed basics of PMTs, APDs, and SPADs, a simple comparison among them is summarized in Table 1-2, with some recent examples of publications [35], [37], [39], [41], [56]–[58]. Benefiting from the high sensitivity and high speed of SPADs, LiDAR systems can achieve single photon detection with a compact detector and at a higher rate.

Parameters	PMT	APD	SPAD
Sensitivity	High	High	Very High
Dark noise	Low	Technology-dependent	Technology-dependent
Size	Large	Small	Small
Integration level	Low	High (APD array)	High (SPAD/SiPM array)
CMOS compatibility	×	√	√
Output form	Analog	Analog	Analog/Digital
Magnetic-safe	×	√	√
Recent examples	[35], [37]	[39], [41]	[56]–[58]

Benefiting from the high sensitivity of SPADs, LiDAR systems can achieve single photon detection. Therefore, the SPAD's performance metrics, SPAD's figure-of-merit and TDC's performance metrics for LiDAR applications need to be developed to describe their performances.

1.4. SPAD Performance Metrics

As the detector of single photon counting LiDAR systems, SPAD's parameters have significant influence on the system's performance. In this section, important parameters include dark count rate (DCR), photon detection probability (PDP), afterpulsing probability (AP), and timing jitter (TJ) will be briefly introduced.

1.4.1. Dark Count Rate (DCR)

Generally, SPADs have higher sensitivity compared to other detectors. However, they are also more sensitive to various noise sources. As one of the major sources of noise, DCR is an important parameter to describe their noise performance when there is no incident light. SPADs fabricated using different CMOS technologies may have

different defect levels, thus giving rise to different DCR performance [54]. In addition to the strong dependence on temperature and biasing voltages, the DCR level of SPADs has a significant dependence on specific technologies. For example, for our recently designed SPAD based on standard CMOS technologies, the DCR falls in the range of tens to hundreds of kilohertz [48], [51], [59]. For CMOS image sensor technologies, the DCR achieved sub-100 Hz in 180 nm, 130 nm, and 90 nm technology more than ten years ago [60]–[62]. However, the integration and cost should also be considered, especially for industrial applications where mass production is needed. In a LiDAR application, when the background illumination is weak, the DCR may become one of the major limitations to the sensitivity. The choice of technology nodes has a significant influence on the SPAD's DCR level.

1.4.2. Afterpulsing Probability (AP)

Afterpulsing (AP) is caused by the release of trapped carriers during or after a SPAD's reset process, thus introducing additional false counts. For PQR SPAD, the reset time is usually longer than the minority carrier lifetime, so afterpulsing is more likely to happen during the reset process. In the faster AQR SPAD, the afterpulsing can happen both during and after the reset process. When measuring the AP, we mainly refer to the measured inter-arrival-time (IAT) of the output pulses. A complete characterization of afterpulsing and retriggering phenomenon of PQR SPADs was explored in detail in [63]. The SPAD's AP is obtained by measuring the IAT based on the accumulation of a histogram [64]. Low AP will increase the maximum count rate of SPADs. AP can be intentionally eliminated by increasing the hold-off time of SPADs to empty the trapped carriers before the reset process, but the penalty is a lower counting rate.

1.4.3. Photon Detection Probability (PDP)

PDP is a dimensionless term that describes the detection efficiency of SPADs. In general, the higher the PDP is, the more sensitive will be the LiDAR system. However, a higher detection probability also implies that detectors are more sensitive to the noise caused by environmental light. In this case, monochromatic lasers are preferred over other light sources for LiDAR applications. However, a SPAD with high PDP peak at

a specific wavelength does not mean it will also have good performance in certain LiDAR applications. Therefore, the evaluation of the SPAD's performance in LiDAR applications must be based on specific wavelengths since the PDP has a strong wavelength dependence. In addition to a strong wavelength dependence, PDP also has a strong excess voltage dependence. Generally, the higher the excess voltage, the higher is the PDP. However, an unsuitably high excess voltage may saturate the SPAD, thus reducing the PDP because the DCR is at a fixed level. So, the biasing conditions should be chosen properly for optimized PDP. Temperature will also affect the PDP by affecting the bandgap of the device, DCR, and the breakdown voltage of the SPAD [49], [51], [65]

1.4.4. Timing Jitter (TJ)

The TJ is a nonideal property which can affect the distance resolution of the LiDAR systems. The origin of TJ in SPADs is the time delay between the detection and electric output caused by the drifting and diffusion of charges. In a SPAD, photons absorbed within one diffusion length away from the depletion region can diffuse to the depletion region and trigger an avalanche. According to the physical mechanism of TJ, measured temporal response of SPADs can be modeled with three major parts: a Gaussian distribution due to the detected photons being absorbed in the depletion region, detected photons being absorbed within one diffusion length away from the depletion region, and random background photons absorbed.

TJ is commonly characterized by full-width-at-half-maximum (FWHM). In this figure, it is shown that the TJ (FWHM) mainly depends on the drifting of carriers in the depletion region. The diffusion tail represents excess counts that are caused by the later diffused carriers from the neutral region. Therefore, the excess voltage applied across to the junction may affect the TJ value due to a varying avalanche build-up time. The higher the excess voltage is, the faster a sustainable avalanche is formed. A simple schematic explaining this dependence is shown in Figure. 1-6.

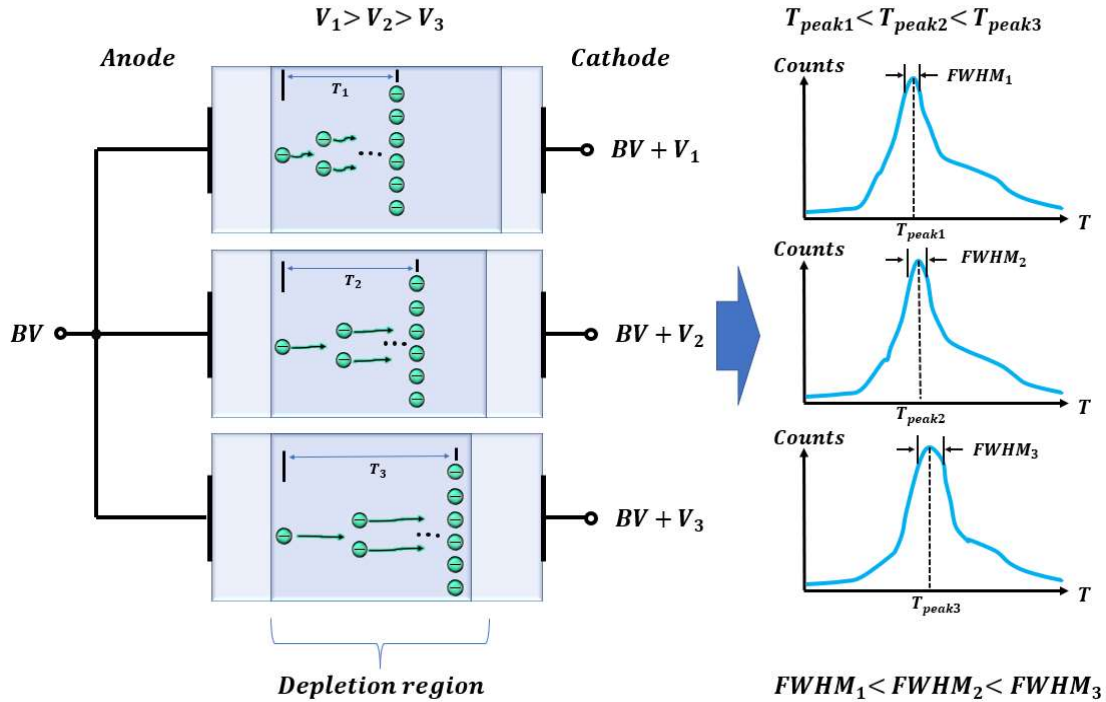


Figure 1-6. Schematic of biasing-temporal response relation, (BV): breakdown voltage; (FWHM): full-width-at-half-maximum

Similar to the voltage dependence of the previously discussed PDP, the temporal response of SPADs is also related to the biasing voltage. Considering three different excess voltages V_1 , V_2 , and V_3 , the higher the excess voltage, the less time it takes for an electron/hole to gain enough energy for inducing ionizations. In this case, the time delay between the photon absorption and the effective output pulse is different. Also, the FWHM of the output pulse will vary.

1.4.5. Dead Time

The dead time of SPADs influence their maximum count rate, thus affecting the frame rate of LiDAR systems. The maximum count rate of a SPAD can be expressed as Eq. 1-4.

$$CR = \frac{1 - P_{AP}}{T_D} \quad 1-4$$

In this equation, P_{AP} is the afterpulsing probability, and T_D stands for the dead time. The origin of dead time is due to the quench and reset process of the SPAD. Due to the time needed for the charge and the release of the carriers, SPADs are not fully prepared for the next detection. However, in some AQR-based SPAD circuits, a hold-off circuit can be intentionally adopted to eliminate the afterpulsing.

From the discussion of SPAD's parameters, a SPAD-based LiDAR system may have a higher precision and accuracy compared to APD-based LiDAR systems due to a higher electric field across the junction. With a higher electric field, the time delay between the absorption of photons and the effective output pulses are comparatively short, thus increasing the accuracy. From the same point of view, the timing jitter of a SPAD caused by the diffusion of minority carriers is generally smaller than the timing jitter in an APD, which means a better precision.

1.5. SPAD Modeling

Since SPADs have various advantages over PMTs and APDs in LiDAR applications to achieve single photon counting probability, it becomes necessary to have good SPAD design. In ToF-PET applications, SPADs can be integrated into arrays with time-to-digital converters (TDCs) to form silicon photomultipliers (SiPMs) or digital silicon photomultipliers (dSiPMs) to further improve the timing resolution and increase the compactness of ToF systems. In LiDAR applications, SPADs can be integrated into arrays for higher throughput and improved noise performance [66]–[71]. With the advancement of silicon manufacturing technologies, many SPADs are fabricated using various CMOS technologies, from standard technologies to custom technologies, depending on the specific applications. With CMOS technologies, SPADs can be easily integrated with different readout circuits for following-stage signal processing, such as active quench and reset circuits, time-gated circuits, analog counters, and TDCs [72], [73].

SPADs fabricated using specific CMOS technologies may suffer from reduced photon detection probability (PDP) due to passivation layers above the device and the thin depletion region of the junctions. They may also suffer from high dark count rates (DCR) due to the increased doping concentration in advanced CMOS technology nodes [74]. Therefore, SPAD models are important to simulate and predict the performance before fabrication. However, few studies focusing on the SPAD model development were presented. Therefore, it is important to discuss the progress of SPAD models, ranging from the conventional multiplication models in 1960s to 2-dimensional SPAD models published in recent years [75]–[78].

Many researchers have contributed to the development of SPAD modeling from different perspectives. For good SPAD models, basic operational principles and technology-related parameters should be considered concurrently. For SPADs, two major types of models, physical models and circuit models, will be discussed in this article. More specifically, physical SPAD models are developed to simulate physical mechanisms of individual devices. Such mechanisms are usually related to intrinsic properties of the material, structures, and the operating principles of the device. SPAD circuit models are proposed to describe SPADs' behavior in real circuits. Without either one of these two types of models, the actual performance of SPAD-based detection systems cannot be accurately predicted, which makes the design and optimization of SPADs more challenging. For PDP models, the most considered aspects are light absorption and avalanche triggering. The material, SPAD structures, doping concentration, and optical properties of any layers of the device can significantly affect SPADs' PDP, making the modeling process more complicated. Some of the above-mentioned parameters are confidential and not accessible to users. Therefore, estimated values for some parameters are used in the model development, which may cause large differences between simulations and measurements.

For DCR models, dark carriers have replaced photon-generated carriers as the research focus. These carriers generated under total dark conditions can initiate undesirable avalanche events when the electrical field is high enough. The generation of dark carriers in SPADs is due to two major mechanisms: thermal generation and tunneling [79], [80]. For each mechanism, there are several different types of models, which are usually categorized by the existence of traps, or recombination-generation centers. The contribution of these different mechanisms largely depends on external operational conditions such as voltage and temperature.

1.6. Research Contributions

The research focuses on the design and modeling process of SPADs that have single photon counting ability. Targeting CMOS-based SPADs, this work aims to present the influence of the different fabrication processes. Especially, the process' influence on the SPAD's important parameters: DCR and PDP. Based on the discussion

on the SPAD's performance in various applications, a further step was taken to investigate the SPAD modeling process. The main research contributions of this work are summarized as follows:

- **A literature review on the SPAD's application in the single-photon-counting LiDAR systems.**

From the review, the optical sensors and the related circuits architectures used in LiDAR systems were discussed, focusing on automotive applications. The principles, architectures, emerging techniques, research challenges and future directions were discussed, respectively. Based on the literature review, the research challenges, and importance of the SPAD design were also presented.

- **A literature review of various SPAD models.**

In the review, the development of SPAD modeling process was discussed with the focus on several important SPAD parameters. The effectiveness of different SPAD models from multiple research groups were compared to show the fundamental modeling process and crucial design considerations. The review can provide a good reference for designers to optimize the CMOS-based SPAD design.

- **SPAD modeling fundamentals and procedures using TCAD and MATLAB.**

Based on the literature review of SPAD's applications in LiDAR systems and SPAD models for optimized design, a new, more efficient modeling process was proposed in the research. In addition to the efficient modeling process, a new 2-D SPAD model was developed to consider the effect of the electric field degradation near the edge of the junction. The proposed 2-D SPAD model achieved closer predictions on the DCR of SPADs and shows a good agreement with the measurements.

- **Design and measurement of passive quench SPADs and output buffers.**

Passive quench SPADs were designed to validate the effectiveness of the proposed 2-D SPAD model. P+/N-well SPADs with dedicated size and shape were designed and measured. All the passive quench SPADs were connected to output buffers to drive the measurement devices.

Publications:

1. **X. Qian**, W. Jiang, and M. J. Deen, “Single Photon Detectors for Automotive LiDAR Applications: State-of-the-Art and Research Challenges”, *IEEE Journal of Selected Topics in Quantum Electronics*. doi: 10.1109/JSTQE.2023.3304294 (Accepted August 8, 2023, Published with early access).
2. **X. Qian**, W. Jiang, A. Elsharabasy, and M. J. Deen, “Modeling for Single-Photon Avalanche Diodes: State-of-the-Art and Research Challenges,” *Sensors* 2023, vol. 23, no. 7, p. 3412, Mar. 2023, doi: 10.3390/S23073412.
3. **X. Qian**, W. Jiang, M.J. Deen. “Enhanced Photon Detection Probability Model for Single-Photon Avalanche Diodes in TCAD with Machine Learning,” *2022 IEEE International IOT, Electronics and Mechatronics Conference (IEMTRONICS)*, Toronto, ON, Canada, 2022, pp. 1-6, doi: 10.1109/IEMTRONICS55184.2022.9795802. (Best Presenter Award)
4. R. Scott, W. Jiang, **X. Qian**, and M. J. Deen, “A Multi-Time-Gated SPAD Array with Integrated Coarse TDCs,” *Electronics* 2022, vol. 11, no. 13, p. 2015, Jun. 2022, doi: 10.3390/ELECTRONICS11132015.

1.7. Thesis Organization

In Chapter 1, the motivation and application of SPADs were introduced. As one of the most important applications of SPADs in the industry, LiDAR systems were briefly introduced that include the discussion on the basic operation principles, commercial products, common optical sensors, and important sensor parameters. The discussions highlighted SPAD’s potential in single-photon-counting LiDAR systems, emphasizing the importance of SPAD modeling in optimizing SPAD’s various performances. Then, the research contributions were summarized, followed by the thesis organization at the end of the Chapter.

In Chapter 2, a literature review of SPAD’s application in LiDAR systems is presented first. Then SPAD’s performance based on different technologies was discussed. Based on the state-of-the-art SPAD’s parameters, figure-of-merit (FoM) was adopted to compare different CMOS technologies. Realistic SPAD’s performances was

demonstrated, followed by an exploration of SPAD models development. The SPAD models are introduced from the basic physical procedures to the various modeling methods. The review of SPAD models can provide as a good reference for improved SPAD modeling process that has higher accuracy and more convenience.

In Chapter 3, a complete modeling process of SPAD based on 65 nm standard CMOS technology was developed. First, the modeling fundamentals are introduced, including different physical mechanisms, definitions, and equations of different parameters. Second, the key considerations in each modeling step are described, from the basic structure definition to the extraction of simulation results. Based on the proposed 1-D SPAD modeling process, a further investigation is conducted to improve the accuracy of the model by extending the proposed 1-D model to a 2-D SPAD model. The comparison between the 1-D simulation and 2-D simulation is discussed accordingly.

In Chapter 4, the design procedure of SPADs based on 65 nm standard CMOS technology is explored. Key considerations such as the layer definition, size definition, shape, output buffers, and front-end circuits are discussed. The simulated results of SPAD's performance based on SPICE model are introduced. After that, the measurement of SPAD's current-voltage characteristics is shown to calibrate the SPICE model. In this Chapter, the simulation and measurement are considered together to have improved understanding of SPAD's design and circuit model.

In Chapter 5, the measurement of SPAD's key performance is conducted, including the DCR and PDP. The DCR is characterized to show the voltage dependence with negligible afterpulsing. And the PDP is measured at different biasing voltages and wavelengths. The measured DCR and PDP are compared to the simulated value obtained from the proposed 1-D and 2-D SPAD model in Chapter 3. Based on the measured results, discussions on the modeling process and parameters are presented to improve the future development of SPADs.

In Chapter 6, research challenges are summarized according to the literature review, SPAD modeling and design process, and measurements. Based on the summarized challenges, we outlined some potential future research directions which

may further improve the performance of SPADs. Finally, conclusions are given to summarize the whole work.

Chapter 2

REVIEW OF SPADS IN LIDAR APPLICATIONS AND SPAD MODELS

In this chapter, a comprehensive review of the application of Single-photon avalanche diodes (SPADs) in the latest light detection and ranging (LiDAR) systems for automotive vehicles is presented, highlighting the critical importance of selecting appropriate optical sensors. The chapter delves into the recent advancements in SPAD-based LiDAR systems and examines key figures-of-merit (FoMs) associated with their performance. Given the substantial potential of Time-of-Flight (ToF) applications, an additional exploration of various SPAD models is conducted. These models wield significant influence over SPAD design and performance, therefore further enhancing the scope and effectiveness of SPAD-based applications.

2.1. Recent Progress of SPAD and Application in LiDAR Systems

Based on the brief introduction of SPAD' operating principles and important parameters given in Chapter 1, a detailed review of recent progress of SPAD and its applications is presented in this section. Among all the CMOS SPADs, different technologies exhibit significantly different performance. Therefore, a comparison is necessary when designing SPADs for specific applications. From a general point of view, the shrinking size of CMOS technologies can bring higher speed circuits and higher integration. However, dark counts may also be increased due to the increasing doping concentration in advanced CMOS technologies.

The comparison of SPADs is shown in Table 2-1. We listed some SPADs by following the order of technology node size. From Table 2-1, it is seen that custom

Adapted from X. Qian, W. Jiang, A. Elsharabasy, and M. J. Deen, "Modeling for Single-Photon Avalanche Diodes: State-of-the-Art and Research Challenges," *Sensors* 2023, vol. 23, no. 7, p. 3412, Mar. 2023, doi: 10.3390/S23073412. (Appendix A)

Table 2-1. Recent Progress of SPAD Detectors and Important Performance Metrics

Reference Year	Peak PDP	PDP @ (~ 900 nm)	DCR (cps/ μm^2)	AP (%)	Dead time(ns)	TJ (ps)	Size (μm) [*]	Material	Technology	FoM _t	FoM _i
[81] [82] 2019	31.8 %	7%	55.4	2.2	100	10 7.7	11.08	Si	45nm CIS/65nm CMOS	0.0039	0.014
[83] 2022	62%	4.2% (940 nm)	0.1	0.97	0.97	52	8.8 (diameter)	Si	55nm BCD	38.49**	501.53**
[84] 2022	11%	-	0.7	-	-	18 5	18.5 (pitch)	Si	55nm BCD	-	-
[85] 2022	20.3 %	5%	19.1	-	-	-	12 (diameter)	Si	55nm BCD	-	-
[86] 2018	8%	2%	2800	<10	100	7.8	20 (diameter)	Si	65nm standard CMOS	0.0017	0.0025
[51] 2021	23.8 %	0.6%	233	0	3.5	13 9	10 (diameter)	Si	65nm standard CMOS	0.032	0.0042
[87] 2021	22%	22%	20	0.1	6	30 0	10 (diameter)	Si	90nm/40nm Back illumination	0.027	0.48
[88] 2022	21.8 %	21.8 % (940 nm)	0.25	<0.1	6	21 4	2.5 (pitch)	Si	90nm Back illumination	0.34	4.24
[89], [90] 2021	64%	10% (850 nm)	0.4	2.7	500	<2 00	78 μm^2	Si	110nm CIS	0.010	0.15
[91] 2023	73%	7% (850 nm)	12.6	0.15	3000***	68	78.5 μm^2	Si	110nm CIS	0.001	0.002
[92] 2019	25%	5.3%	50	-	-	12 7	23.78 (pitch)	Si	130nm CIS	-	-
[93] 2020	-	-	3.48	-	-	23 3	23.78 (pitch)	Si	130nm HV-CMOS	-	-
[94] 2021	48% /34%	4.2%	0.19	0.14 /0.09	0.9/1.9	75	10/20/30 (diameter)	Si	160nm BCD	16.30**	256.97
[95] 2018	47.8 %	4.7%	0.49	0	25	10 6	28.5 (pitch)	Si	180nm CIS	0.26	29.40
[96] 2020	33.5 %	3%	2.5	0.21	10	88	3 (diameter)	Si	180nm CIS	0.24	0.096
[97] 2020	26.7 %	2.5%	0.4	-	-	-	9.4 (pitch)	Si	180nm CIS	-	-
[98] 2021	55%	8.4%	0.23	<3	50	16	50 (pitch)	Si	180nm CIS	1.39	1107.07
[99] 2017	67%	18.5 %	0.5-0.8	-	-	-	25 (pitch)	Si	Custom	-	-
[100] 2018	49%	5.3%	9	2	8.3	35	50 (diameter)	Si	Custom	0.56	39.72
[101] 2017	30%	-	-	0	40000 (hold-off)	15 4	25 (diameter)	InGaAs/InP	Custom	-	-
[102] 2019	38%	-	-	1	50000 (hold-off)	31 0	100-200 (diameter)	Ge-on-Si	Custom	-	-

*The size is estimated based on circular SPAD if a diameter is specified, and based on rectangular SPAD if a pitch size is specified.** The optimum value is used for calculations***The dead time is set for eliminating afterpulsing.

CMOS image sensor (CIS) and Bipolar-CMOS-DMOS (BCD) technologies can have very small DCR level, which improves the performance of SPADs in LiDAR systems, especially in a low-level light environment. In contrast, the DCR level of SPADs fabricated using standard CMOS technologies is dozens to hundreds of times higher than CIS and BCD-based detectors.

Based on the important parameters listed, figure-of-merit (FoM) can be developed to have a general estimation of SPAD's performance. Here, we propose two simple SPAD FoMs for LiDAR applications. The first FoM which focus on the performance at ~ 900 nm wavelength is given by

$$FoM_l = \frac{PDP(@900nm)}{DCR} \times Area \times \frac{1 - P_{AP}}{TJ \times T_D}. \quad 2-1$$

In the equation of FoM_l , the unit of DCR is $\text{cps}/\mu\text{m}^2$, and Area is estimated according to given diameters or pitch size. We also calculated the FoM_t for each SPAD, derived from [53]. We made some modifications as we have already calculated the value of per-unit-area DCR, as shown in Eq. 2-2.

$$FoM_t = \frac{PDP_{peak} \times (1 - P_{AP})}{TJ \times T_D \times \sqrt{DCR}}. \quad 2-2$$

From Eq. 2-1 and 2-2, the larger the FoM_l and FoM_t are, the better the performance. Both FoM_t and FoM_l are calculated as shown in the table. The significant difference of DCR, dead time, and TJ affect the final FoM value of different SPADs listed in Table II. However, for the PDP value of each SPAD, there are no major differences in magnitude. In this case, for evaluating the SPADs in different technologies, the timing performance and noise performance are considered in the current scheme. In [81], [82], a 3D-stacked CMOS technology is used to improve the total area efficiency. The first tier of the chip is based on 45 nm CIS technology, and the second tier is based on 65nm CMOS technology for SPAD signal processing circuits. With the high integration, the SPAD can achieve around 60% fill factor. SPADs fabricated using CIS technologies can achieve peak PDP generally higher than 25% [89]–[92], [95]–[98]. SPADs fabricated using BCD processes also have good PDP, DCR and TJ [83]–[85], [94]. For standard CMOS, low dead time and jitter are advantages when a high counting rate in LiDAR applications such as a real-time fast imaging is needed [51], [86]. In addition to frontside-illuminated SPADs, backside-illuminated SPADs also have good area

efficiency. However, it is expected that BSI SPADs have a high timing jitter due to the location of junction is away from the backside [87], [88]. For high-voltage technology, the timing jitter is found to be higher, due to a wider depletion region [93]. Both SPADs fabricated based on silicon custom technologies have good peak PDP and PDP at ~900 nm, compared to other SPADs [99], [100]. In Table 2-1, we also list III-V SPADs and Ge-on-Si SPAD for long wavelength LiDAR applications [101], [102].

2.1.1. 2D SPAD Array & SiPM Array

In LiDAR systems, 2D SPAD arrays are commonly adopted as the focal plane array (FPA) [103]. Each SPAD of the array can generate individual signals to trigger the corresponding TDC unit. In contrast, multiple SPADs are used in a SiPM array to generate a single output to trigger the shared TDCs. Compared to the 2D SPAD array, SiPMs have two major advantages: high integration and improved noise performance. By sharing the TDC with multiple SPADs, the total number of electronic components in the whole array can be reduced, thus being more area efficient. However, image resolution may suffer due to less individual pixels being available. In addition to the parameters of the individual SPAD and TDC mentioned earlier, the size, pixel number, and total power consumption need to be considered.

Size

The size of a 2D SPAD array depends on the size of the individual pixel and the number of pixels. For an individual pixel in a 2D SPAD array, a larger size means that the pixel can potentially receive more photons than small-sized pixels. However, when the size of individual pixel increases, the total DCR of the specific pixel can also increase, which will lower the signal-to-noise ratio. In severe cases, the pixel may always be triggered by noise, thus losing its function. In addition to the design issues, some properly designed individual pixels may still become “hot pixels”, which have abnormally higher DCR than other pixels. This is mainly due to defects during the fabrication process [48].

Pixel Number

To achieve a high image resolution, more pixels can be designed in a SPAD/SiPM array by reducing the pixel size. However, a certain pixel area is needed to guarantee

that the pixel can collect enough photons. Therefore, a trade-off is made between the individual pixel size and the number of pixels. Figure 2-1 shows a schematic illustration of how the pixel numbers can affect the image resolution, assuming that the total size is fixed.

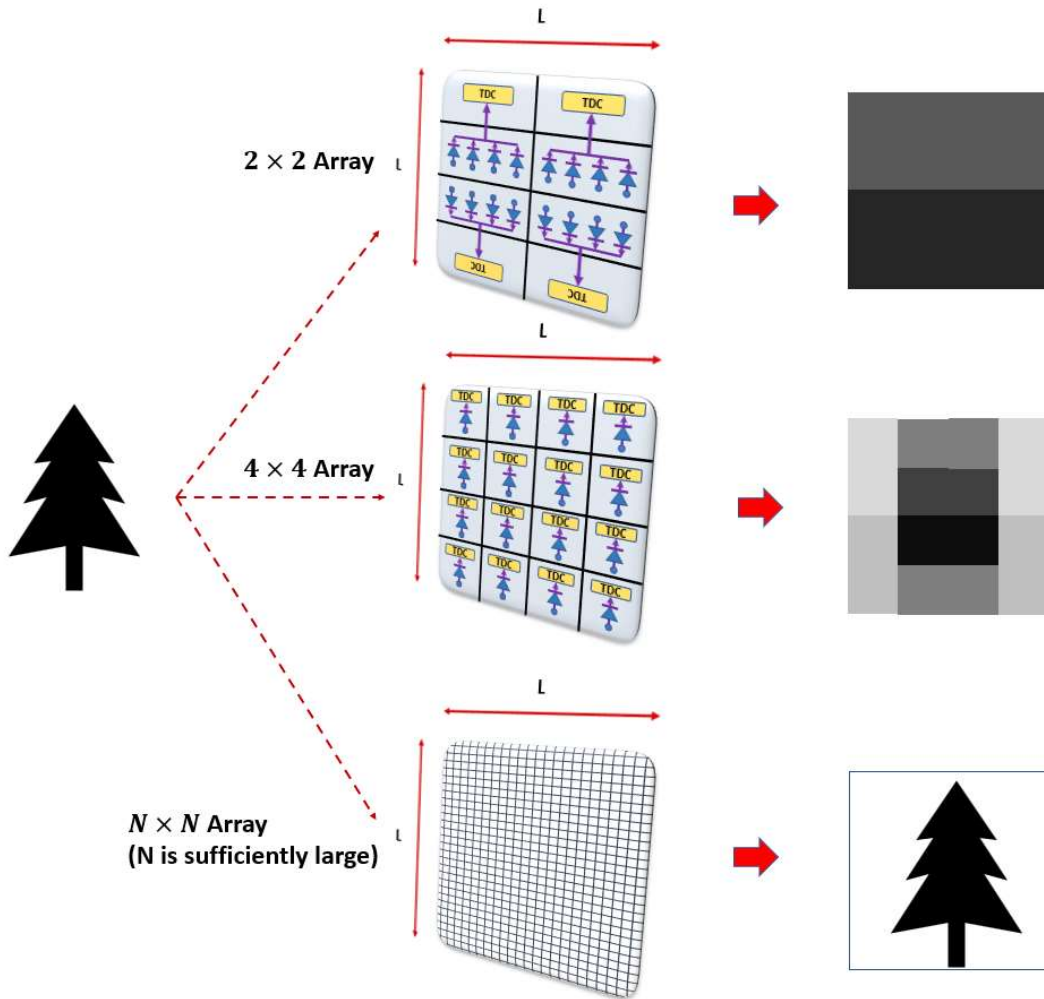


Figure 2-1. SPAD/SiPM array's relation to the image resolution.

Both size and pixel numbers have a significant influence on the total performance of the system. However, when the total size of the array is fixed, a trade-off between the pixel numbers and the single pixel size must be made. When the size of single pixel is decreased, the detection efficiency and noise performance may be affected. In this case, the SPAD models are required to predict the performance of single pixels before any fabrication for better performances. Therefore, we further discuss the progress of the SPAD modeling process.

2.2. SPAD Models – Principles, Progress, and Challenges

Many researchers have contributed to the development of SPAD modeling from different perspectives. For good SPAD models, basic operational principles and technology-related parameters should be considered concurrently. For SPADs, two major types of models, physical models and circuit models will be discussed in this paper. More specifically, physical SPAD models are developed to simulate the physical mechanisms of an individual device. Such mechanisms are usually related to intrinsic properties of the material, structures, and operating principles of the device. SPAD circuit models are proposed to describe SPADs' behavior in real circuits. Without either one of these two types of models, the actual performance of SPAD-based detection systems cannot be accurately predicted, which makes the design and optimization of SPADs more challenging.

For PDP models, the most considered aspects are light absorption and avalanche triggering. The material, SPAD structures, doping concentration, and optical properties of any layers of the device can significantly affect SPADs' PDP, making the modeling process more complicated. Some of the above-mentioned parameters are confidential and not accessible to users. Therefore, estimated values for some parameters are used in the model development, which may cause large differences between simulations and measurements.

For DCR models, dark carriers have replaced photon-generated carriers as the research focus. These carriers generated under total dark conditions can initiate undesirable avalanche events when the electrical field is high enough. The generation of dark carriers in SPADs is due to two major mechanisms: thermal generation and tunneling [79], [80]. For each mechanism, there are several different types of models, which are usually categorized by the existence of traps, or recombination-generation centers. The contribution of these different mechanisms largely depends on external operational conditions such as voltage and temperature.

Timing jitter models have been developed to evaluate the timing performance of SPADs. In SPADs, there is some delay for photon absorptions to successfully trigger output pulses, which means a lag between the detection of a photon and an effective

avalanche output. However, the timing performance of SPADs is susceptible to false detection events caused by dark counts. Therefore, the measurement of SPADs' and SPAD arrays' temporal response is usually based on a statistical method by measuring a certain number of repetitive output pulses to generate a histogram [104]–[106]. This method is also known as the time-correlated single photon counting (TCSPC) technique. In a typical histogram response of SPADs, the time response of detections varies, which may also be caused by the timing jitter. Accurate timing jitter models can help designers to optimize the timing performance of SPADs, so that the fluctuation measured in a histogram can be improved.

The SPAD physical models and SPAD circuit models have enabled designers to have more freedom to adjust their design for optimized performances prior to fabrication, especially for the SPAD designs using advanced CMOS technologies. In recent years, many models have been proposed for the accurate and comprehensive description of SPAD-based detection systems. Therefore, discussion of SPAD principles and recent progress of models can provide a clearer idea and guidance for designers to improve their own models and designs.

2.2.1. SPAD Operational Principles

SPADs are reverse biased above their breakdown voltages [107], and this is commonly known as operating in the Geiger Mode. In the Geiger Mode, the avalanche current increases rapidly with increased reverse biasing. Therefore, the effective output of a typical SPAD is like a digital pulse, which means that we do not need an analog to digital converter (ADC), thus reducing the cost. A simple SPAD structure and its current-voltage (I-V) characteristics are shown in Figure 2-2.

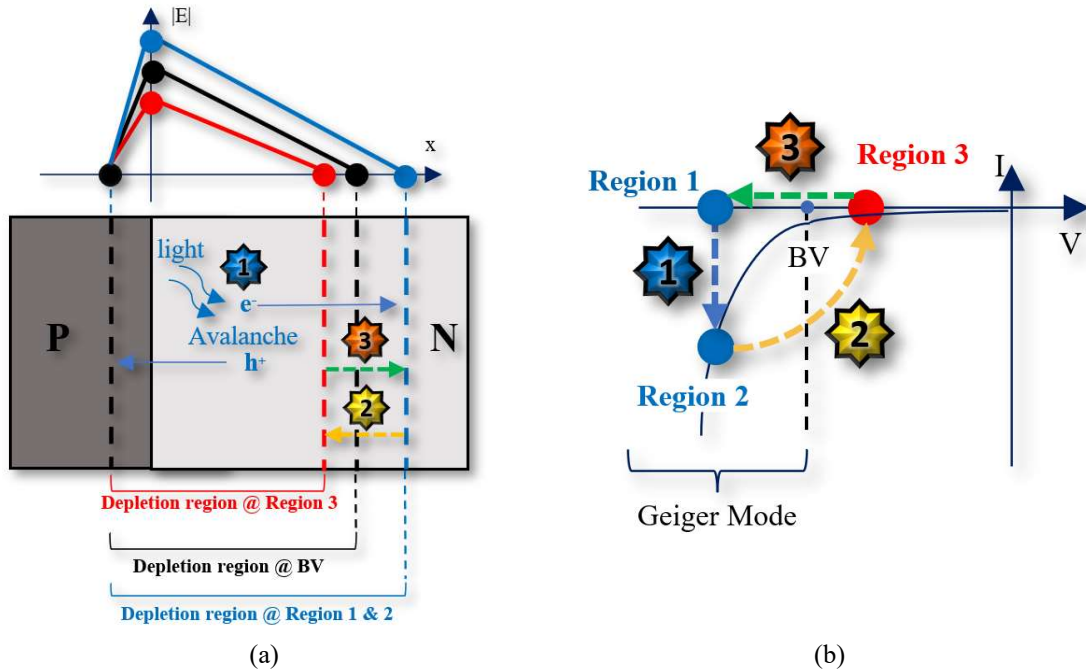


Figure 2-2. (a) Simple SPAD diagram (b) Current-voltage (I-V) characteristics

Ideally, SPADs will be biased above the breakdown voltage. The difference between this bias voltage and the breakdown voltage is called the excess voltage. When there is no carrier, there will be no avalanche current, and SPADs will stay in region 1 until there is an incident photon or dark carrier that initiates an avalanche. When the avalanche is triggered, the SPAD's current will increase rapidly, thus entering Region 2. However, SPADs are not able to stay in this region for a long time, due to the heating effect of the huge self-sustained avalanching current, which can burn the device. As a result, SPADs must be quenched properly. The most common way to achieve this is to reduce the reverse voltage below the breakdown voltage to suspend the avalanche. Then, successfully quenched SPADs can enter Region 3, after which they will be reset to region 1, to be ready for the next detection.

Based on the actual physical process of the detection of SPADs, researchers are focusing on the development of accurate SPAD models. These models are based on various technology-computer-aided design (TCAD) tools such as Sentaurus and Silvaco [108], [109]. A comprehensive review of these models can help to identify future improvements that can be made. Different from many basic analytical models, SPAD models and SPAD circuit models must consider the actual CMOS technology-

related parameters, such as doping concentrations, traps' population and defects level, as shown in Figure 2-3.

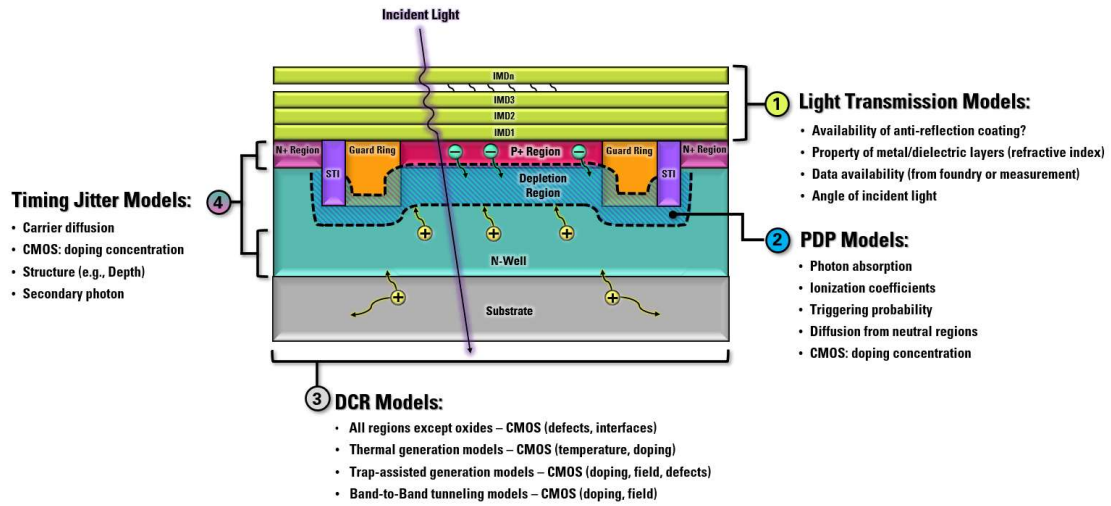


Figure 2-3. SPAD models graphical diagram with process-related parameters

2.2.2. DCR Models

CMOS SPADs' DCR performances vary considerably, which pose challenges for the design and measurements of SPADs. For example, if a SPAD was fabricated with a large active region using standard CMOS technologies, the DCR measurement may easily saturate the oscilloscope [110]. As a result, photon detection events can no longer be measured. choosing proper models for DCR also should take the physical process into consideration. Some CMOS technologies can achieve very low dark counts, while others can achieve more compact integration with the penalty of much higher dark counts. For a 0.35 μm high-voltage CMOS (HV-CMOS) technology, it can easily achieve over 10 times smaller DCR, compared to a 130 nm standard CMOS technology [111]. Therefore, the influence from the CMOS process is significant in DCR modeling. The difference between PDP models and DCR models is that optical property is one of the key characteristics being investigated in PDP models, but the defects and temperature properties are more frequently discussed in DCR models.

The energy required to excite electrons from the valence band to the conduction band can be from charge carrier other than from the absorption of photons in DCR models. The most challenging work in DCR modeling is to investigate the accurate contribution of different mechanisms shown in Figure 2-4.

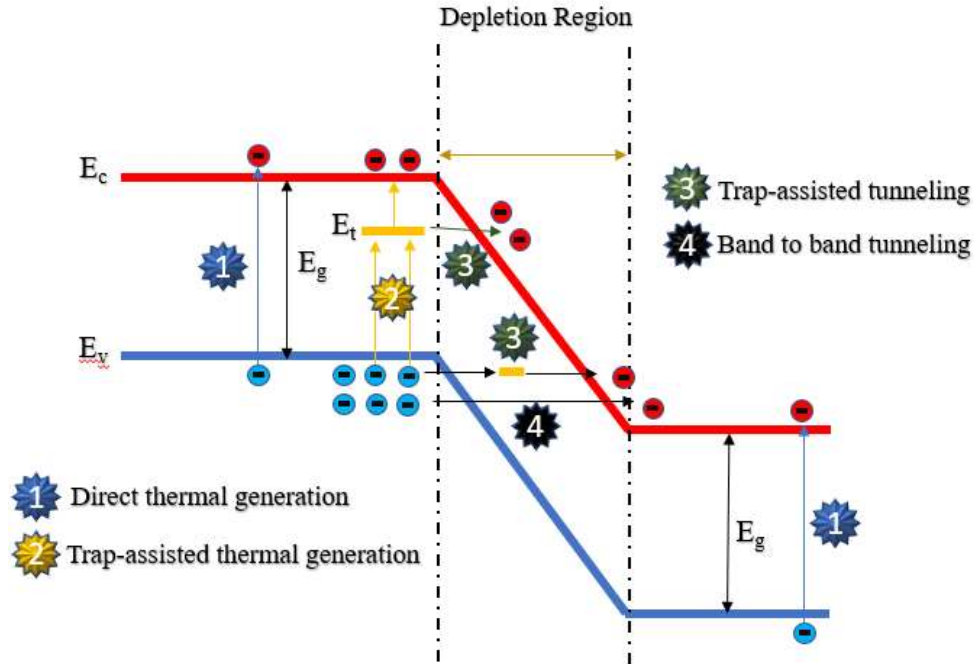


Figure 2-4. Four major mechanisms of DCR in SPADs

Detailed fundamentals regarding each DCR mechanism are analyzed in the modeling process part in Chapter 3. A summary of recently developed DCR models is shown in Table 2-2.

Ref	SRH*	TAT**	BTBT***	Tools/Methods	Comments
[112]	Yes	Yes	Yes	Analytical	<ul style="list-style-type: none"> Assume electrons and holes' lifetime are equal. A mid gap trap energy was assumed
[113]	Yes	Yes	Yes	Analytical	<ul style="list-style-type: none"> 7 parameters were obtained by fitting measurements with simulations
[114]	-	Yes	-	Analytical	<ul style="list-style-type: none"> Only depletion region was considered. Single trap energy level was assumed.
[79]	Yes	Yes	Yes	TCAD****	<ul style="list-style-type: none"> Use trap population as fitting parameter. Use doping concentration and gradient coefficients as fitting parameters. No change to the SRH and BTBT model.

[78]	Yes	Yes	Yes	TCAD	<ul style="list-style-type: none"> • Trap energy is assumed to be 0.15 eV higher than the middle bandgap. • Compared different guard ring structure. • Assuming a pure Boron process.
[115]	Yes	-	Yes	TCAD	<ul style="list-style-type: none"> • Doping and trap information are obtained from measurement. • Considered the contribution from neutral regions. • Trap energy level is 0.19 eV for SRH model. • Fitting parameters are obtained at 125K and 325K.
[116]	Yes	-	Yes	TCAD	<ul style="list-style-type: none"> • Considered the damage of implantation

*Shockley-Read Hall recombination; ** Trap-assisted tunneling; *** Band to band tunneling.
**** Technology-aided computer design.

In [79], trap density, doping concentration and doping gradient coefficients are all set to fitting parameters used in the SRH and BTBT model developed by Kindt and Hurkx. The convenience of implementing traditional models with user-modified parameters is assisted by TCAD simulation tools. The proposed model in [79], simulated results were compared with the measured DCR of a different device fabricated in different technologies, including 0.15 μm CMOS and 0.13 μm CIS technologies [117], [118]. The good predictions associated with these works indicate that this modeling approach can be used in different technologies. For the BTBT component of the DCR model proposed in [79], a larger parameter of B in Equation 5 was chosen. $8 \times 10^{15} \text{ cm}^{-3} \cdot \text{s}^{-1}$ was chosen in lieu of $4 \times 10^{14} \text{ cm}^{-3} \cdot \text{s}^{-1}$ by explaining a faster growth of DCR with high biasing voltage. Note that the power factor of the electric field was the same as the value used in traditional BTBT models [112], [119]. The experimental results showed that DCR was highly related to doping concentrations.

A similar idea was studied by Knežević *et al.* in [78], where the influence of guard ring structures was investigated. With a lower doping concentration of the guard ring, the total DCR of devices was simulated to be much smaller than the device without guard rings or with higher-doped guard rings. In this model [78], several assumptions related to the trap energy were made. However, the fitting parameter of trap energy has a different value in the SRH model than in the BTBT model, indicating the influence from other physical parameters. An improvement of their model is that they adopted

the process-related simulation tool **Sprocess**, which is more accurate compared to the simulation based solely on ideal geometric structures. The simulated results were compared to the measurements in [120], which also shows a good accuracy. However, the fitted value of trap energy was obtained after assuming a certain doping concentration. This means that different doping concentration assumptions will give different fitted values of trap energy. Due to the lack of information from foundries, the only way for researchers to determine the exact doping concentration is from real measurements. The inaccurate doping information did give rise to unexpected DCR performances, which was proven in [115]. In [115], the doping concentrations used in DCR modeling were from measurements. More importantly, the DCR contribution from upper and bottom neutral regions also needs to be considered. For the BTBT models, default values from the Hurkx model are used. The energy level was regarded as a fitting parameter, but the actual doping concentration was used. Thermal generation was also neglected in the neutral regions. Apart from the analysis of DCR from the neutral and depletion regions, the DCR contributions were also modeled in different regions, from the central uniform region to the guard ring region.

Compared to [78], the DCR model was further developed with additional quantitative analysis of contributions from different regions. DCR generated from guard ring structures is believed to dominate the total DCR of SPADs, due to the previous underestimation of its doping concentration. In addition to these impurity-related DCRs, the accuracy of temperature-dependent DCR performance was improved by extracting fitting parameters at different temperatures. Moreover, the influence of some specific fabrication steps has been analyzed. For example, the increased DCR caused by implantation damage has been investigated [116]. Most recent DCR models which are based on TCAD software have considered the bandgap narrowing effect, which is caused by the high doping concentration, and carriers' density of junctions [121]. This effect can be activated in some widely used simulation tools, like Sentaurus.

2.2.3. PDP Models

PDP models are developed to simulate the accurate detection probability of SPADs. It is challenging to predict the PDP accurately because fabricated SPADs may suffer from worsening PDP due to technology-related issues such as the depletion region

width, doping concentration, and defects [72]. Therefore, modeling of PDP should be based on physical processes and take technology-specific parameters into consideration. PDP models are also divided into two parts: photon absorption model and avalanche triggering model.

Photon absorption refers to how many photons are absorbed in certain regions. For a given incident photon, its energy determines whether it can successfully excite an electron from the valence band to the conduction band. Without enough energy, the photon will pass through the "transparent" material to such photons. Before the light passes through SPADs and gets absorbed, a certain portion of light has already been reflected at the interfaces of different layers with different refractive indices. However, diverse modern CMOS technologies may have different layers above the active region of SPADs, and these layers may have different optical properties.

The avalanche triggering probability models focus on the possibility of a carrier successfully initiating an avalanche event. A carrier must obtain enough energy to trigger impact ionization events. Therefore, there is no physical equation rigorously describing the triggering probability. Considering the requirements of both accuracy and simplicity for the triggering probability model, two differential equations were proposed to generally represent the triggering probability, which can be expressed as:

$$\frac{dP_n(x)}{d(x)} = [1 - P_n(x)] \times \alpha_n(x) \times [P_n(x) + P_p(x) - P_n(x)P_p(x)] \quad 2-3$$

$$\frac{dP_p(x)}{d(x)} = -[1 - P_p(x)] \times \alpha_p(x) \times [P_n(x) + P_p(x) - P_n(x)P_p(x)] \quad 2-4$$

The terms $P_n(x)$ and $P_p(x)$ are the desired triggering probability of electrons and holes, respectively. $\alpha_n(x)$ and $\alpha_p(x)$ are the ionization coefficients that have significant influence on the total triggering probability. Detailed derivation and discussions are presented in Chapter 4.

From Eq. 2-3 and 2-4, the ionization coefficients are important in the modeling of PDP. There are many models for ionization coefficients. In 1966, McIntyre assumed that the holes' ionization coefficients are k times the electrons' ionization coefficients [75]. However, some improvements can be made to this. First, the ionization coefficients used by McIntyre are not used for PDP modeling but rather used for calculating noise spectral density where a linear relation derived from the current

multiplication theory was assumed. Such a linear relationship is hard to measure from modern SPADs. Second, there will be an effective output pulse as long as a self-sustained avalanche occurs. So, ionization coefficient models obtained from APD may not be accurate enough at the high electric field in SPADs. There are many other ionization coefficients models developed which are available for simulation under high electric fields. Recent PDP models based on commercial simulators have adopted different ionization coefficient models according to their SPADs' structures and applications, and they are shown in Table 2-3. It should be noted that terms used in different models have varying meanings as shown in the last column of Table 2-3.

Table 2-3. Commonly Used Ionization Coefficient Models in Sentaurus [108]				
Model [Ref]	General Form (Electric Field)	Electric Field Range ($10^5 V/cm$)	Investigated Parameters	Key Characteristics
Van Overstraeten Model [122]	$\alpha = \gamma \times a \times \exp\left(-\frac{\gamma b}{E}\right)$	1.75 - 6	<ul style="list-style-type: none"> Temp dependence: γ Constants: a, b Electric field dependence: E 	<ul style="list-style-type: none"> 2 sets of coefficients Editable coefficients
Okuto-Crowell Model [123]	$\alpha = a(1 + c(T - T_0))E^\gamma \exp\left(-\left(\frac{b(1 + d(T - T_0))}{E}\right)^\gamma\right)$	1 - 10	<ul style="list-style-type: none"> Constants: a, b, c, d, T_0, γ Temp dependence: T Electric field dependence: E 	<ul style="list-style-type: none"> Empirical Model Editable coefficients Wide electric field range
Lackner Model [124]	$\alpha = \frac{\gamma \times a}{Z} \exp\left(-\frac{\gamma b}{E}\right)$	1 - 10	<ul style="list-style-type: none"> Temp dependence: γ, Z Electric dependence: Z, E 	<ul style="list-style-type: none"> Wide electric field range Editable coefficients
Bologna Model [125]	$\alpha = \frac{E}{a + b \times \exp\left(\frac{d}{E + c}\right)}$	0.5 - 6	<ul style="list-style-type: none"> Temp dependence: a, b, c, d Electric dependence: E 	<ul style="list-style-type: none"> Wide temperature range Full-temperature calibration

Van-Overstraeten Model

The Van Overstraeten-de Man Model is based on the Chynoweth law [108], [122]. There are two different sets of coefficients used in the equations. One set for low

electric field and another set for high electric field. The parameters were obtained from the measurements [122]. This ionization coefficient can be used when the electric field is between $1.75 \times 10^5 \text{ V/cm}$ and $6 \times 10^5 \text{ V/cm}$.

Okuto-Crowell Model

Different from the Van Overstraeten-de Man model, the Okuto-Crowell model is an empirical model, which means that the model takes input and output data from experiments to find the best fit [123]. In this model, a detailed physical process is regarded as a “black box”. Therefore, there are many fitting parameters for this ionization coefficient model compared to others. The effective electric field of this model is between 10^5 V/cm and 10^6 V/cm , based on default values provided in [108]. However, users can adjust the parameters to fit the specifications of their own measurements.

Lackner Model

The Lackner model has a similar form as the Van Overstraeten-de Man model, since they are both based on Chynoweth’s law [124], [126]. The difference between these models is that the Lackner model has introduced the electric field dependence in the coefficient part of the exponential equation. As shown in Table 2-3. the model is effective when the electric field is between 10^5 V/cm and 10^6 V/cm , a large electric field range compared to the Van Overstraeten-de Man Model.

Bologna Model

This model is more suitable to simulate the junctions when the reverse electric field is small [125]. The highest electric field of the model is $6 \times 10^5 \text{ V/cm}$, the same as Van Overstraeten–de Man model, but the minimum electric field of this model is $5 \times 10^4 \text{ V/cm}$. Such a value is relatively small in the SPAD’s working region since SPADs are usually biased above the breakdown voltage. This model is suitable when simulating SPADs with a wide depletion region (which has a smaller electric field). Another advantage of this model is the wide applicable temperature range, making it suitable for simulating devices with large currents caused by the heating effect.

Local Model versus Non-Local Model

These ionization models can be applied to simulating avalanche triggering probability, as shown in Eq. 2-3 and 2-4, depending on the SPAD structure, electric

field and temperature. The parameters in the equations used are all related to specific positions. Since the ionization coefficients are related to the electric field, the electric field is a function of position. Therefore, they can be called “local models”. However, a generated carrier must travel a certain distance to gain enough energy to have an ionization collision. This distance is usually called “dead space” since impact ionization cannot occur inside this region, regardless of the electric field [127], [128]. To address this problem, some non-local models have been developed [129].

Non-local models have become important due to the shrinking of the depletion region’s width with the advancement of silicon technology nodes. Most of the developed non-local models are based on the multiplication theory of APDs, which have intrinsic layers (multiplication layers). In traditional local models, the ionization coefficients are high when the electric field is high, regardless of whether the carrier is newly generated or has traveled a long distance. In non-local models, ionization coefficients are dependent on both the electric field and the distance of being accelerated. For a certain electric field, E_c , a carrier must be accelerated by the field for a distance of d_c to acquire enough energy to trigger an impact ionization event. Okuto and Crowell proposed their idea of non-local property as early as 1974 [130]. Hayat *et al.* continued to develop the non-local model by using recurrence equations, which take all carriers into consideration [131]. They also extended their work to determine a more accurate distribution of avalanche events [132]. They split the whole multiplication region into several small segments and applied an iterative method to solve the equations. However, this results in added complexity to the PDP modeling process compared to local models.

Pseudo-local models have the same form as local ionization coefficient models, but with calibrated parameters obtained from experiments. One possible solution is to use pseudo-local models to include the dead space effect. The data extracted from the experiment has already been considered the dead space effect. Cheong proposed a possible way to link the experimentally obtained coefficients with the non-local ionization coefficients models [133]. Considering this, the local model of ionization coefficients appears to be more convenient and reasonable for SPADs, compared to the models used in similar APDs.

With the development of photon absorption simulations and avalanching triggering probability models, there are many recently proposed PDP models of SPADs that are summarized in Table 2-4.

[Ref] Year	[134] 2021	[135] 2020	[136] 2021	[137] 2021
Technology	180 nm Standard CMOS	800 nm Custom CMOS	350 nm High-voltage CMOS	350 nm High-voltage CMOS – With ARC***
Excess Voltage	15%-30% of BV****	3 V	3.3 V	6.6 V
Incident Light Wavelength Range	450-900 nm	450-900 nm	450-850 nm	450-850 nm
Wavelength @ Peak Response*	~ 500 nm	~ 500 nm	~ 600 nm	~ 650 nm
PDP/PDE Difference** @ Peak Response	~ 12 %	~ 38 %	~ 1.3 %	~ 1.1 %
Method	TCAD + MATLAB	TCAD + MATLAB	CST Microwave Studio + TCAD	CST Microwave Studio + TCAD
Key Information	•Passivation layer information from foundry (SiO ₂ and Si ₃ N ₄).	•Process related parameters are known and used.	•A 80 µm-diameter SPAD.	•PDP was improved for short wavelengths
Additional Comments	Achieved improved accuracy.	Fitting parameter free. High difference at short wavelengths.	Readout circuits limit the PDP measurement below 2V excess.	PDP vs. ARC thickness. PDP versus incident angle.
[Ref] Year	[137] 2021	[138] 2016	[139] 2010	[140] 2009
Technology	350 nm High-voltage CMOS – Without ARC***	150 nm Standard CMOS	Custom Technology	Custom Technology
Excess Voltage	6.6 V	3 V	5 V	3 V
Incident Light Wavelength Range	450-850 nm	350-850 nm	400-1000 nm	400-1000 nm
Wavelength @ Peak Response*	~ 600 nm	450 nm	550 nm	550 nm
PDP/PDE Difference** @ Peak Response	~ 3.2 %	~ 0 %	~ 68 %	~ 61 %

Method	CST Microwave Studio + TCAD	TCAD	TCAD	TCAD
Key Information	<ul style="list-style-type: none"> •Long wavelength response was enhanced •Lower doped epi-layer used 	-	•Okuto-Crowell ionization coefficient model	<ul style="list-style-type: none"> •Okuto-Crowell ionization coefficient model •A 200 μm-diameter SPAD
Additional Comments	Without anti-reflection layer.	Light transmission was not included.	Limited information on layers above the active region.	Limited information on layers above the active region.
<p>*Peak response refer to the simulated result; ** $\left \frac{\text{Measured Data} - \text{Simulated Data}}{\text{Measured Data}} \right$ data estimated from published sources, with a step of 50nm-wavelength; ***ARC: anti-reflection coating layer; **** Breakdown voltage from measurements</p>				

Regarding photon absorption, some models simply followed the absorption law, which mainly depends on the absorption coefficient, depth and thickness of the SPAD depletion region [74], [141]. In this case, the wavelength dependence of the PDP will certainly be a smooth curve, with different peak values. The different positions of the peak indicate the depth of the junction. For example, in [139], a deep and thick depletion region was adopted to achieve enhanced PDP at a longer wavelength. These types of PDP models are good for indicating the general detection efficiency in the whole wavelength range. However, when it comes to the measured data, there are always some ripples in the PDP response of SPADs fabricated using different technologies [79], [118], [134], [136]–[138], [142]–[149]. These ripples are related to the complex transmission between dielectric and passivation layers above the active region of SPADs [136], [142], [150].

If researchers are interested in the detailed spectral distribution of the PDP over the whole range, then they must pay attention to the modeling of the light transmission through the different layers. If the parameters and properties of these layers above the active region are known to designers, then they may simply introduce Monte-Carlo simulation (MCS) to determine the light transmission. However, it is more likely that researchers may not have access to the detailed specifications of the technologies they are using, which means that the thickness and the property of the materials used in the

fabrication are confidential. Under these conditions, the accurate modeling of light transmission will be very difficult.

Some specific technologies have the option of using ARC layers to reduce light reflection. For example, the light reflection was reduced to 0.1% after a single-layer ARC was applied, when the wavelength was 504 nm, and no ripples were observed in the measured data [135]. In [137], the researchers modeled the PDP with and without the ARC layer, and also tried to find the PDP dependence on the thickness of the ARC layer at different wavelengths. Moreover, in the CMOS imaging sensor (CIS) process, the optimization of stacking passivation and dielectric layers are available, thus increasing the total detection efficiency [118], [151].

Most of the listed PDP models in Table 2-4 did not consider the edge effect. Some PDP models claim that the edge effect is small compared to the large central active region so that the problem can be simplified to a 1-D problem. Some other models simply neglected the edge effect due to the 1-D differential equation used to calculate the triggering probability. However, the edge region will undoubtedly have more effect on the total detection efficiency as the sizes of SPADs are scaling down in modern CMOS technologies. In this case, the conventional 1-D model may not be accurate enough to predict the total PDP and the PDP is usually overestimated. To solve the accuracy issue of the conventional 1-D PDP models, Liu C *et al.* proposed a 2-D PDP model to investigate the edge effect, by calculating the 1-D differential equations following the actual direction of the local electric field [77]. In this way, the total PDP is the summation of each PDP distributed through the whole active region, with the area as the weighting factor. A similar simulation for finding the SPAD's edge effect was conducted in [152].

The decreased PDP caused by the edge effect is also believed to be more dominant in the short wavelength range because the junction area is close to the surface. For longer wavelengths, the diffusion of the carriers from the neutral region may have a greater contribution, thus having the highest triggering probability at the boundary. Under this condition, the edge effect is more significant in short wavelengths for shallow SPADs. Therefore, the dependence of the edge effect on the wavelengths deserves further investigation.

2.2.4. Challenges for the SPAD Modeling

From the discussions above, improvements of SPAD models can help to improve the design and performance of various imaging systems. However, there are still some challenges that need to be addressed to further improve the accuracy and efficiency in modeling SPADs. Current challenges and future research areas are summarized in Figure 2-5, and further described thereafter.

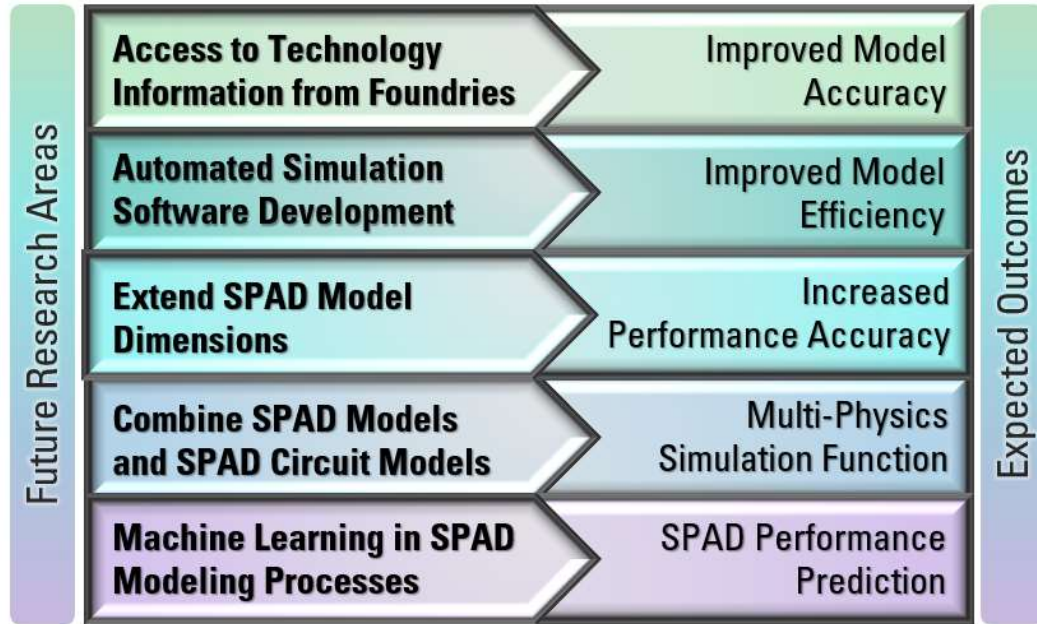


Figure 2-5. Summary of future research perspectives and potential outcomes

Confidential technology information from foundries has led to difficulties for researchers to develop more accurate models. To have accurate estimation of certain key parameters in SPAD models, it is important to know the doping profile of each region, depth and thickness of each region, material of dielectric layers and defect information, etc. Researchers can extract these parameters directly or indirectly from experimental measurements, but these may be complicated and time consuming. For example, it may be possible to guess the doping profile by measuring the breakdown voltage. It is also possible to measure the thicknesses of the metal layers and/or passivation layers above the active region from the cross-sectional images using scanning electron microscope (SEM), thus improving the accuracy of PDP and DCR models.

For a realistic SPAD fabricated using advanced CMOS technologies, it is challenging to get accurate information of each passivation layer. Figure 2-6 (a) and (b) shows an illustration of the cross-sectional and layout view of a SPAD design using the TSMC 65 Standard CMOS technology which has 9 metal layers and many inter-metal dielectric layers. The fifth metal layer M5 in the dotted boxes is used to shield the SPAD, with an opening window to reduce the reflection of the light above the active region. However, there are still many inter-metal-dielectric (IMD) layers with different thickness and properties which deserve more investigation for the future improvement of SPAD models.

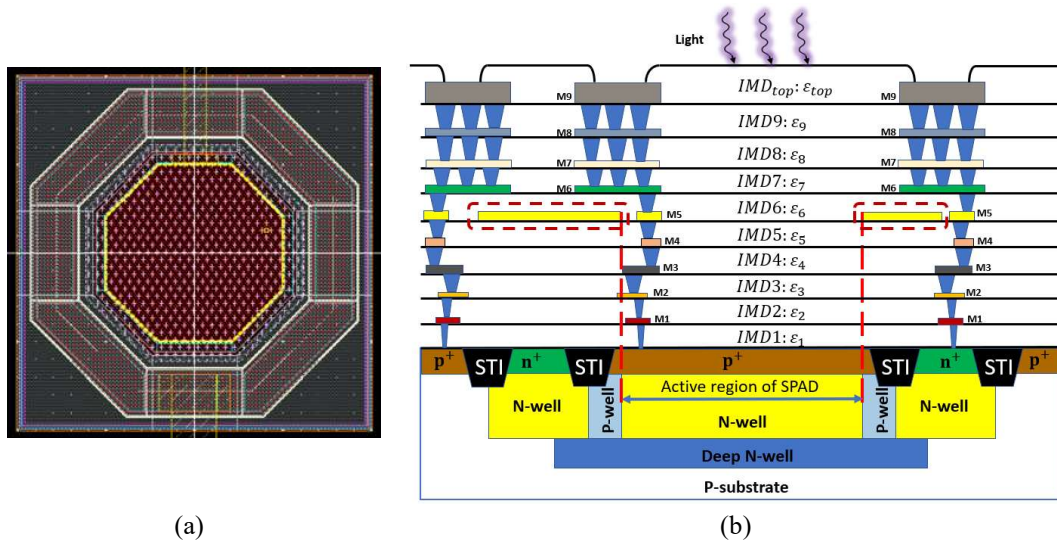


Figure 2-6. Realistic structure of SPAD based on TSMC 65 nm Standard CMOS technology (a) Layout view (top view) (b) Cross-sectional view of the design.

The development of simulation tools will also benefit the SPAD modeling process. Currently, TCAD is commonly used for simulating electric parameters of SPADs including the electric field distributions, ionization coefficients, and breakdown voltage, but not their noise performance [153]. However, these parameters need to be exported to be further processed by other software like MATLAB. When there are many parameters to be investigated, the modeling process will be complicated and time-consuming. The development of software automation can significantly improve modeling efficiency.

The dimensions of SPAD models can be extended from 1 dimension to 2 dimensions, and even 3 dimensions. Due to the shrinking of technologies, SPADs can be fabricated in a much smaller size, which should take the edge effect into

consideration. However, most of the current SPAD models are in 1 dimension. Some of the models have been developed in 2 dimensions for a better estimation of PDP and DCR [76]–[78]. In 3-dimension models, the performance can be more accurate since they can model these parameters with different SPAD shapes, such as circular SPADs, rectangular SPADs, and octagonal SPADs.

The accuracy of SPAD models also depends on the density of mesh points in a simulation process. Without correct mesh settings, convergence problems may occur. That is to say, it is challenging to adjust the mesh settings in semiconductor device simulation. When it comes to SPAD simulations, the convergence issue can be more important due to the rapid change of physical parameters during the avalanche process. To achieve good accuracy, many calculation iterations are needed, which can lead to additional computational and time costs of modeling. To overcome this problem, machine learning techniques can be adopted in SPAD modeling processes. With machine learning, the design parameters like doping concentration, dimension or size, shape, as well as other parameters, can be investigated to see their influence on the specific performance of SPADs. With more data available from simulations, machine learning models can be more accurate. Therefore, predictions of SPAD performances based on different technologies can be made without the need for iterative modeling process again.

2.3. Conclusion

In this Chapter, a review of recent progress of SPAD's applications was reviewed, which indicated the importance of SPAD design and modeling. Consequently, an in-depth review of SPAD models was explored for better understanding of modeling fundamentals, considerations, and modeling methods. Based on the comparison among different models, research challenges regarding the SPAD modeling were summarized, which can provide good guidance for the optimization of SPAD models in Chapter 3.

Chapter 3

CHARACTERIZATION AND SIMULATION OF SPADs

From the previous discussion in Chapter 3, SPAD models play a vital role in predicting SPAD performance and optimizing SPAD's design. Although there are some works that have been explored in the 1-D modeling process of SPADs. However, few efforts have been put on the 2-D modeling of SPAD's DCR and PDP so far, which becomes more significant due to the shrinking sizes of more advanced technology nodes. Especially, when guard ring structures are commonly adopted in SPADs to avoid premature breakdown near the edge of the junction, they tend to have more dominant effects on the central active region for small SPADs. The reduced electric field brought by the guard ring structures can potentially impact the DCR and PDP of SPADs. To investigate the "edge effect" on both DCR and PDP of small SPAD in advanced CMOS technologies, a complete 2-D simulation process is important. Therefore, a complete simulation method of SPAD's 2-D DCR and PDP model is proposed by combining the TCAD Sentaurus and MATLAB.

In this chapter, the fundamental modeling principles of SPAD's DCR and PDP are discussed, followed by detailed explanations of each stage in the modeling process, this includes device structure building, mesh generation, device simulation, and a fully automated simulation process.

3.1. Modeling Fundamentals

3.1.1. Avalanche Triggering Probability

Avalanche triggering probability is defined to be the probability of a carrier successfully initiating avalanches in diodes. Two conditions must be satisfied for an avalanche breakdown: impact ionization and self-sustaining. A carrier must gain sufficient energy to induce impact ionization events. This is characterized by ionization coefficients and α_e and α_h , both of which have exhibited a strong electric field dependency. The definition of them is given by equation 3-1 and 3-2.

$$\alpha_n = \frac{1}{nv_n} \frac{dn}{dt} \quad 3-1$$

$$\alpha_p = \frac{1}{pv_p} \frac{dp}{dt}, \quad 3-2$$

where v_n and v_p represent the velocity of electrons and holes, respectively. n and p are the carrier density of electrons and holes, respectively. However, formation of a self-sustaining avalanche requires a chain of impact ionization events. The ionization integrals I_n and I_p are developed to determine if a self-sustaining avalanche occurs, which are given by

$$I_n = \int_0^d \alpha_n(x) e^{-\int_x^d (\alpha_n(x') - \alpha_p(x')) dx'} dx \quad 3-3$$

$$I_p = \int_0^d \alpha_p(x) e^{-\int_0^x (\alpha_p(x') - \alpha_n(x')) dx'} dx \quad 3-4$$

Note that the direction of the integration aligns with the actual electric field across the depletion region, with a width of d . When either of the ionization integrals equals one, an avalanche breakdown may occur. However, for some heavily doped diodes, there exists another breakdown known as Zener breakdown, which may have a lower breakdown voltage than the avalanche breakdown.

However, there is no exact physical equation that rigorously describes the precise avalanche triggering probability of generated carriers at specific positions. Such avalanche triggering probability, however, is important to determine the SPAD's performances. To address the problem, two differential equations were proposed to represent the triggering probability at specific locations, which have been briefly introduced in Chapter 2. From a simple PN junction shown in Figure 3-1.

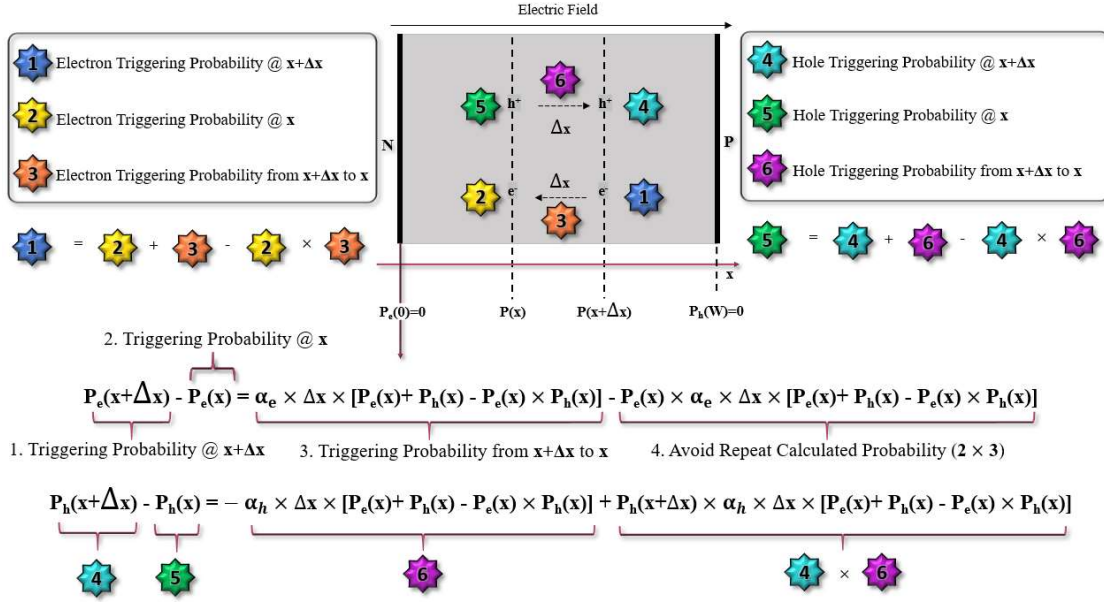


Figure 3-1. Triggering probability diagram. Creative commons License.

The terms $P_n(x)$ and $P_p(x)$ are used to describe the triggering probability of electrons and holes at position x , respectively. Considering the triggering probability of electrons $P_n(x)$ at position x and $P_n(x+\Delta x)$ at position $x+\Delta x$, and the electric field's direction is from position 0 to position d . Therefore, the triggering probability caused by the electron at position $x+\Delta x$ consists of two parts: electron triggering probability at position x , and the probability that it triggers avalanche during the travel from position $x+\Delta x$ to position x . In this case, the triggering probability $P_n(x+\Delta x)$ can be expressed as:

$$P_n(x + \Delta x) = P_n(x) + \alpha_n(x) \times \Delta x \times [P_n(x) + P_h(x) - P_n(x)P_h(x)] - P_n(x) \times \alpha_n(x) \times \Delta x \times [P_n(x) + P_h(x) - P_n(x)P_h(x)] \quad 3-5$$

To avoid the repeat calculation of probability, the avalanche caused by both the electron and hole is subtracted. When the Δx is small enough, the equation can be formulated to a differential equation. For the holes' triggering probability, a similar equation is developed. Therefore, a complete differential equation set is given by:

$$\frac{dP_n(x)}{d(x)} = [1 - P_n(x)] \times \alpha_n(x) \times [P_n(x) + P_p(x) - P_n(x)P_p(x)] \quad 3-6$$

$$\frac{dP_p(x)}{d(x)} = -[1 - P_p(x)] \times \alpha_p(x) \times [P_n(x) + P_p(x) - P_n(x)P_p(x)] \quad 3-7$$

Note that this set of differential equation must be solved simultaneously, with two fixed boundary conditions given by:

$$P_n(0) = 0, P_p(d) = 0 \quad 3-8$$

With the implementation of the differential equations and the boundary conditions, the modeling of avalanche triggering probability becomes notably convenient. And this approach allows adjustment of the only parameter: ionization coefficients. The unit of the ionization coefficients is cm^{-1} . In this case, when they are combined with $d(x)$ in the differential equations, the obtained triggering probability becomes dimensionless. The range of the triggering probability lies in 0 to 1, which is confined by the boundary conditions. Following the modeling of avalanche triggering probability caused by the electrons and holes, the total triggering probability can be written as followed:

$$P_{total}(x) = P_n(x) + P_p(x) - P_n(x) \times P_p(x) \quad 3-9$$

Hence, the position-dependent avalanche triggering probability was modeled, which can be combined with the generation rate to model DCR and PDP of SPADs.

3.1.2. Dark Count Rate (DCR)

Dark count rate (DCR) is used to describe the dark noise of SPADs in the units of count per second (cps) or Hertz (Hz). When the light is absent (both incident and environmental light), carriers can still be generated within SPADs, which are known as “dark carriers”. Considering the high electric field across the junction of SPADs, these dark carriers can still initiate the avalanche, thus causing additional counts. Depending on the driving force, it is more convenient to summarize two major groups that are responsible for the dark carrier generation: thermal generation and tunneling effect. Considering the simplest form of a PN junction, comprising conduction band and valence band. The electrons at the valence band are bonded to the nucleus, being unable to conduct current. When thermal energy is transferred to the bonded electrons, these electrons may become energetic after gaining sufficient energy and “jump” to the conduction band, therefore, the electrons can move freely to conduct current. The thermal generation process of dark carriers has a strong temperature dependency as it is more likely to excite electrons from valence band to the conduction with a narrowing bandgap at higher temperatures. In addition to the thermal generation process, tunneling effect is also a major source of dark carriers. Different from the thermal generation process, the tunneling effect is due to the quantum effect that can “transfer”

electrons from the valence band to the conduction band directly, without the need for overcoming the bandgap. The existence of tunneling effect in SPADs can lead to significantly increased current and enhanced field dependence.

Thermal Generation

For thermal generation in SPADs, there are direct thermal generation and trap-assisted thermal generation. The trap-assisted thermal generation is also known as the Shockley-Read-Hall (SRH) recombination. Due to a very large intrinsic bandgap (typical value: 1.12 eV) of the silicon material, the DCR caused by direct thermal generation is usually negligible in the modeling of SPADs. However, there are some energy levels located in between conduction band and valence band, which are caused by the lattice defects and the damage during the fabrication. These trap traps can serve as very efficient generation-recombination centers, which can capture and release the carriers. Compared to the direct thermal generation, the SRH recombination is considered the dominant mechanism in the thermal generation process in SPADs. The general SRH model used to describe the trap-assisted thermal generation follows the Eq. 3-10,

$$G_{SRH} = \frac{np - n_i^2}{\tau_p \left(n + n_i \times e^{\frac{E_t - E_i}{kT}} \right) + \tau_n \left(p + n_i \times e^{\frac{E_i - E_t}{kT}} \right)}, \quad 3-10$$

where the terms n , p , n_i represent electron densities, hole densities, and intrinsic carrier densities, respectively. τ_p and τ_n are the lifetimes of holes and electrons, respectively. E_t and E_i denote the trap energy level and the intrinsic Fermi level, respectively. k stands for the Boltzmann constant and the T is the Kelvin temperature. Since SPADs are reverse biased above the breakdown voltage, the values of both electron and hole densities (n and p) are negligible compared to the intrinsic carrier density n_i . As a result, Eq. 3-11 can be simplified to:

$$G_{SRH} = \frac{n_i}{\tau_p \times e^{\frac{E_t - E_i}{kT}} + \tau_n \times e^{\frac{E_i - E_t}{kT}}} \quad 3-11$$

From the equations, a strong temperature dependence of SRH is related to the absolute temperature T and the lifetimes of electrons and holes. In addition to the temperature dependence, the lifetimes τ_p and τ_n are also modeled to have doping dependence and field dependence, expressed by:

$$\tau_{p,n} = \tau_{doping} \frac{f(T)}{1 + g_{p,n}(F)}, \quad 3-12$$

where τ_{doping} gives the doping dependence, $f(T)$ gives the temperature dependence, and $g_{p,n}(F)$ gives the field dependence. For SPADs that are operated above the breakdown voltage, the field dependency of carriers' lifetimes is not negligible in the modeling process as the electric field is commonly above 10^5 V/cm. By default, the trap energy level is located in the middle of the bandgap. Since the τ_{doping} introduces the doping dependence, the doping dependence is obtained based on experimental data, following the Eq. 3-13

$$\tau_{doping} = \tau_{min} \frac{\tau_{max} - \tau_{min}}{1 + \left(\frac{N_a + N_d}{N_{ref}}\right)^\gamma}, \quad 3-13$$

where N_a and N_d are acceptor concentration and donor concentration, respectively. The values of the reference doping concentration N_{ref} , and other parameters used for modeling SRH generation rate are given in Table 3-1.

TABLE 3-1. PARAMETERS USED FOR MODELING MINORITY CARRIER LIFETIME

PARAMETER	Electron	Hole	Unit	Note
τ_{min}	0	0	Seconds	Minimum lifetime
τ_{max}	10^{-5}	3×10^{-6}	Seconds	Maximum lifetime
N_{ref}	10^{16}	3×10^{16}	cm^{-3}	Reference concentration
$F(T)$	$(T/300K)^{-1.5}$	$(T/300K)^{-1.5}$	1	Temperature dependence
γ	1	1	1	Weighting factor

Tunneling Generation

The tunneling effect, assisted by the traps, can be modeled by introducing a field enhancement factor to the carrier lifetimes. The modified carrier lifetimes with the field enhancement factor are already given by $g_{p,n}(F)$ in Eq. 3-12. However, the differences

between the measured results and simulation became more significant at higher excess voltages [154]. One reason is that there is another mechanism called the “direct tunneling effect” that becomes dominant at high voltages. This direct tunneling effect is also known as the band-to-band tunneling (BTBT). It becomes the primary source of dark carriers when the electric field is close to or greater than 9×10^5 V/cm at room temperature, as stated in [155]. With such a high electric field across the junction, the direct tunneling phenomenon is more likely to occur. A BTBT model proposed by Hurkx can be expressed as:

$$G_{BTBT} = -B|F|^{\frac{5}{2}}D(F, E, E_{fn}, E_{fp}) \exp\left(-\frac{F_0}{|F|}\right), \quad 3-14$$

where the term $D(F, E, E_{fn}, E_{fp})$ is determined by the bandgap, electric field, electron, and hole Fermi levels. B is a fitting parameter used to match the experimental data, which is also temperature dependent [156]. The default value of B equals to $4 \times 10^{14} \text{ cm}^{-2} \text{ V}^{-2.5} \text{ s}^{-1}$ [157]. The very strong field dependence of the BTBT generation rate can help to indicate if the total DCR is dominated by BTBT mechanism based on DCR versus biasing voltage plot. In Chapter 2, various DCR models have already been discussed with the consideration of technology-specific values, including the trap energy level, trap population, and the damage from implantation.

The total DCR of a SPAD is modeled by integrating the generation rates G of different mechanisms and the simulated avalanche triggering probability $P_t(x)$ along the depletion region, which is calculated by using the MATLAB.

3.1.3. Photon Detection Probability (PDP)

The PDP is modeled by combining the absorbed photon rate and the avalanche triggering probability. Different from the modeling of DCR, external illumination is needed for the modeling of PDP. For a given incident photon, its energy determines whether it can be absorbed and successfully excites the electron from the valence band to the conduction band. Without sufficient energy, the photon will pass through the material as if it is “transparent”. Depending on the optical property of the material, a certain portion of the incident photons has already been reflected at the interfaces of different layers. However, accurate information on the diverse layers above the SPAD in modern standard CMOS technologies is not provided to the users or designers, which

has made it difficult to develop a generalized model that encompasses all technologies and structures. In this case, the modeling of the PDP usually neglects the complicated light transmission among the layers above the SPAD's active area.

With the availability of the 1-D position-dependent avalanche triggering probability, the only thing left for modeling SPAD's PDP is the photon absorption rate, which can be characterized by:

$$I_x = I_{surface} \times e^{-\alpha x}, \quad 3-15$$

where I_x and $I_{surface}$ are the optical intensity at position x and at the surface, respectively. α is the absorption coefficient, which is wavelength dependent. Note that this equation assumes a 1-D direction, and the start point is at position $x = 0$. The absorbed intensity I_x follows an exponentially decaying trend as the light goes deep inside the material. Since we are concerned about the photon number in the modeling of SPAD's PDP, Eq. 3-15 can be converted to the absorption probability for the convenience of calculation, as expressed by:

$$P_{op} = \frac{N_{op}}{N_{surface}}, \quad 3-16$$

where P_{op} is a dimensionless probability, N_{op} and $N_{surface}$ are the absorbed photon density and incident photon density, respectively.

Due to the different bandgaps of various semiconductor materials, the absorption coefficient α of different materials may vary significantly and have an upper wavelength limit. For the typical application of SPAD in PET-CT, the target wavelength window is usually below 500 nm, primarily depending on the scintillators used [158], [159]. For SPAD's application in automotive LiDAR, the wavelengths usually lie in the near-infrared (NIR) range.

3.2. Device Building

To model DCR and PDP of SPADs, structures must be specified with actual dimensional parameters. Since the edge degradation of electric field caused by the guard ring structures is a key consideration in our research, instead of an ideal 1-D PN junction, a 2-D SPAD structure is constructed using the Sentaurus Technology-Computer-Aided-Design (TCAD). In Sentaurus, many tools are available for modeling,

such as the **SPROCESS** for simulating actual processes, **SINTERCO** for simulating interconnects, and **SDEVICE** for simulating electrical characteristics. In the modeling of SPAD's DCR and PDP, we mainly utilize **SDE**, **SDEVICE**, and **SVISUAL** for building device structures, simulating electrical properties, and extracting data, respectively.

Since the actual process information regarding the standard 65nm CMOS technology is not provided to users, SDE was used to build the structure of SPAD with some ideal assumptions, such as the doping concentrations of different regions. Even with these ideal assumptions made during the modeling process, it can still provide reasonable estimations of the general performances of DCR and PDP. A simple PN junction can be modeled with typical P+/N-well doping. A more realistic SPAD structure is then built in comparison to the simple 1-D PN junction and 1-D DCR and PDP models. The structure of 1-D PN junction and the realistic SPAD structure are shown in Figure 3-2.

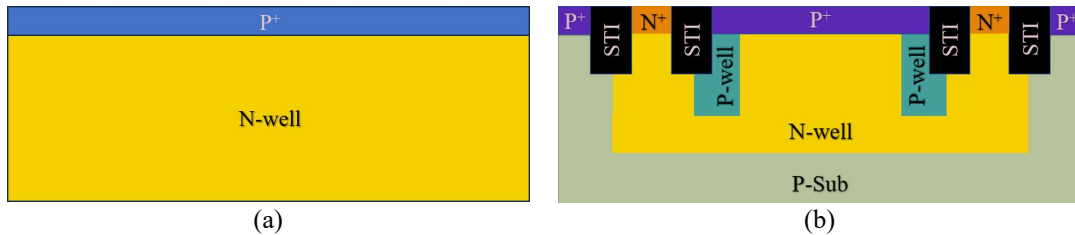


Figure 3-2. Structure of (a) Simple PN junction (b) Realistic SPAD structure

In the simple 1-D PN junction, the junction is uniform, allowing the direct adoption of the conventional 1-D avalanche triggering probability model in the modeling of DCR and PDP. However, for the more realistic SPAD structure shown in Figure. 3-2 (b), the P-well guard ring structures are designed to prevent the premature breakdown (PEB) near the edge region of the P+/N-well junction. This design leads to a non-uniform electric field distribution across the entire active region. In addition, short-trench isolations (STIs) are implemented to isolate P+ and N+ regions, which are consistent with the actual standard CMOS process. The depth of the junction and the doping concentration are adjusted to fit the measured data of PDP wavelength dependence and the breakdown voltage, respectively.

3.3. Mesh Setting

Once the dimensions of the SPAD's structure are specified, the mesh settings should be adjusted properly. A denser mesh leads to more accurate results, as TCAD solves the equations numerically. However, for SPADs operating above the avalanche breakdown voltage, achieving convergence can easily become problematic, leading to significantly increased computing time for a single simulation. To address the issue, two methods were employed in our simulations. From the structure point of view, the mesh is selectively refined in the junction area. By estimating the width of the depletion region, the mesh is refined in an area larger than the total depletion region, as shown in Figure 3-3. Note that the figure is scaled to illustrate the mesh details near the junction. Without suitable mesh refinement, results can be inaccurate, as the avalanche process involves positive feedback, making convergence a challenging work.

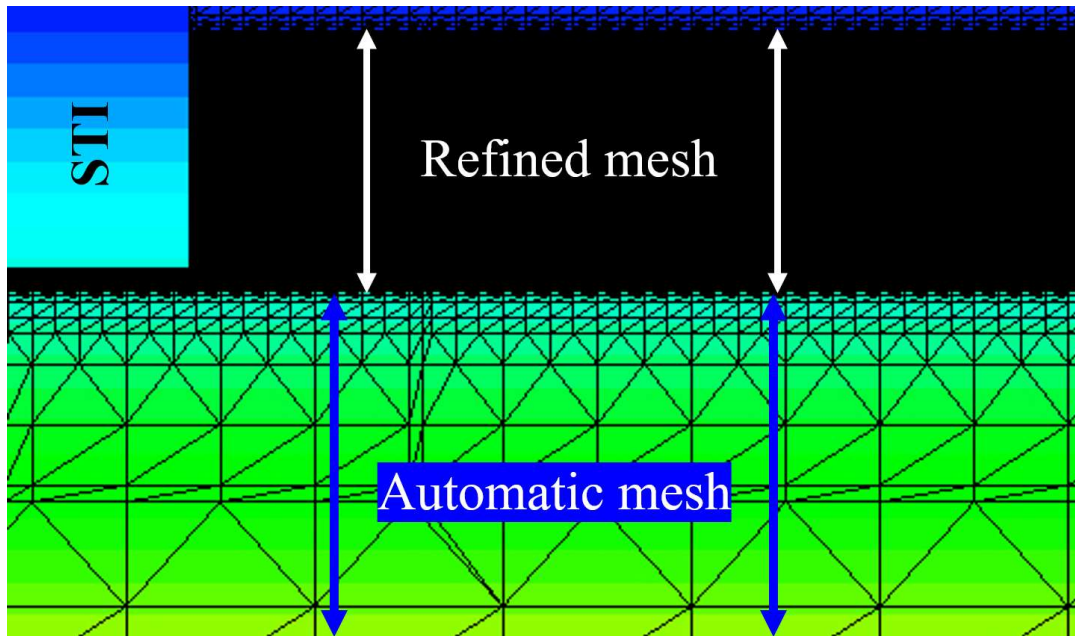


Figure 3-3. Mesh refinement for accurate avalanche simulation

The automatic mesh used in the modeling is defined to be denser near the interface. However, such density near the interface is still not dense enough for modeling avalanche process. In this case, a manually refined mesh is defined to improve the convergence. To avoid the convergence problem, a second method can be adopted in addition to mesh refinement. This method, however, is more suitable for simulating the

breakdown voltage (BV) of a SPAD. When simulating the BV, a specific breaking criterion can be introduced to suspend the avalanche shortly after the breakdown occurs.

The materials should be configured accordingly after determining the structure and mesh settings. Here the silicon material is used for the SPAD, as the 65 nm standard CMOS technology used is also silicon-based. For the STI material, we simply implemented the SiO₂ for oxidation, with all the material parameters set to their default values.

3.4. Device Simulation

Using the SDEVICE tool, electrical and optical properties can be simulated based on the structures. There are many available models that can be employed in the SDEVICE tool, according to user preferences. Before implementing models for simulations, the first step is to define the contacts for the SPADs, allowing external biasing voltages to be applied to the SPADs. In this section, ideal ohmic contacts are used for SPAD's anode, cathode, and body contacts. To prevent the convergence problem during simulating the BV of SPADs, a large serial resistor can be connected to one of the contacts. In the 2-D structure, the contacts are represented by 1-D lines with editable colors, as shown in Figure 3-4.

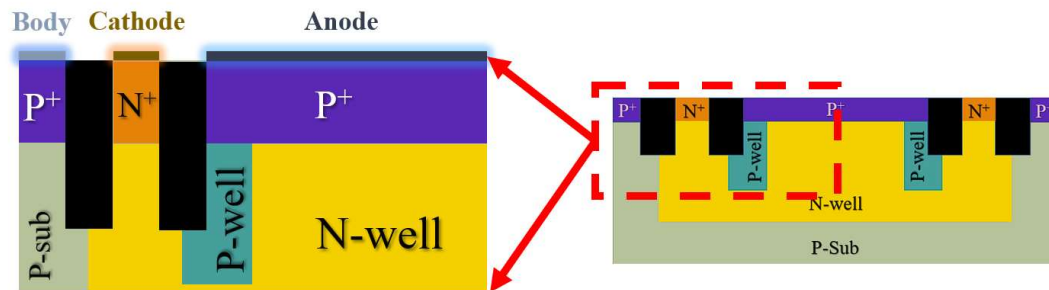


Figure 3-4. Contact definition in SDEVICE.

Note that a 50k Ω serial resistor is connected at the anode which is not visible in the figure or the device structure. Following this, the initial voltage applied to these contacts can be specified. When simulating the BV of the SPAD, the initial value of the three contacts can be simply set to 0 V, given that a sweep function is needed to simulate the reverse I-V characteristics. The next step is the implementation of the models, which is also one of the most important steps.

3.4.1. Physical Models

Firstly, the simulation conducted in Sentaurus solver is based on nonlinear iterations, which rely on coupled equations. The basic equations used in modeling of SPAD encompass the Poisson equation and equations related to electrons and holes. To simulate the DCR of SPADs, default SRH and BTBT models are necessary in the physics section.

However, prior to implementing such models, several modifications must be made to be more accurate. The first modification is related to the intrinsic density n_i , which is the basic property of the material. The default value of n_i is calculated according to the default bandgap of silicon, expressed as:

$$n_i(T) = \sqrt{N_c(T)N_v(T)} \exp\left(-\frac{E_g(T)}{2kT}\right), \quad 3-17$$

where N_c and N_v are the effective density of states within the conduction band and the valence band, respectively. E_g is the intrinsic bandgap of silicon, and k is the Boltzmann constant. However, the intrinsic density may change due to a high doping concentration, which is common in modern CMOS technologies as the size is shrinking. In this case, the doping-dependent intrinsic density must be introduced in the simulation of SPADs, which is also known as the effective intrinsic density $n_{i,eff}$, given by:

$$n_{i,eff} = n_i \exp\left(\frac{E_{bgn}}{2kT}\right) \quad 3-18$$

The term E_{bgn} refers to the bandgap narrowing effect. Here, we introduced the Bennett-Wilson bandgap narrowing model into the calculation, which can be expressed as:

$$\Delta E_g = \begin{cases} E_{ref} \left[\ln\left(\frac{N_{total}}{N_{ref}}\right)\right]^2, & N_{total} > N_{ref} \\ 0, & N_{total} \leq N_{ref} \end{cases} \quad 3-19$$

The N_{total} represents the value of the total density. E_{ref} and N_{ref} are reference values obtained from the experimental data [160]. The default value used for E_{ref} and N_{ref} are 6.84×10^{-3} eV and 3.162×10^{18} cm⁻³, respectively. Note that ΔE_g is only one part of the total band gap narrowing effect E_{bgn} . The other part is a correction to mitigate errors that are caused by the ideal Boltzmann-Maxwell statistics in the simulation, which can be expressed by $\Delta E_{g, Fermi}$. So, the total bandgap narrowing E_{bgn} is the summation of ΔE_g and $\Delta E_{g, Fermi}$ if using Fermi statistics in the simulation.

The second change is the specification of the carriers' mobility in the physics part, which also requires editing. As SPADs are biased above the BV, the electric field across SPADs' junctions are very high, which may saturate the velocity of the carriers. This saturation velocity v_{sat} , can limit the mobility of the carriers in semiconductor materials. For silicon-based device, the velocity saturation model can be expressed as:

$$v_{sat} = v_0 \left(\frac{300K}{T} \right)^{v_p} \quad 3-20$$

where the v_0 is the value of the saturated velocity at 300 K, and v_p is a fitting parameter. The value of v_0 for electrons and holes are 1.07×10^7 cm/s and 8.37×10^6 cm/s, respectively. v_p for electrons and holes are 0.87 and 0.52, respectively, according to [161]. The parameters used for the basic properties of the device are concluded in Table 3-2.

TABLE 3-2. BASIC PARAMETERS FOR SILICON MATERIAL

PARAMETERS	Value	Unit	Note
E_{ref}	6.84×10^{-3}	eV	Bennet-Wilson Bandgap narrowing model reference energy level
N_{ref}	3.162×10^{18}	cm ⁻³	Bennet-Wilson Bandgap narrowing model reference concentration
$v_{0,e}$	1.07×10^7	cm/s	Saturated velocity of electrons at 300 K
$v_{0,h}$	8.37×10^6	cm/s	Saturated velocity of holes at 300 K
$v_{p,e}$	0.87	1	Fitting parameter for electrons in velocity saturation model
$v_{p,h}$	0.52	1	Fitting parameter for holes in velocity saturation model

In addition to the basic information that needs modification in the physics section, specific avalanche models, SRH models, and BTBT models are required to be implemented for SPAD simulation. Concerning the avalanche model, the default one is the Van Overstraeten impact ionization model, which is valid in the electric field ranging from 1.75×10^5 V/cm to 6×10^5 V/cm. For the default model, there are two sets of coefficients used for low electric field and high electric field, respectively. However, we replaced the default Van Overstraeten model with the Okuto-Crowell model.

Compared to the default one in the Sentaurus, Okuto-Crowell model presents two major advantages: empirical model and wide electric field range. Different from the Van Overstraeten model, Okuto-Crowell model takes the input and output data from experiments to find the best fit for all the fitting parameters. In this model, detailed physical process is regarded as a “black box”, which is simple to implement without the need for the complicated definition process of various parameters. Second, the wide electric field range of Okuto-Crowell model (from 1×10^5 V/cm to 1×10^6 V/cm) is valid for simulating SPADs reverse I-V characteristics from zero bias to the operating voltage. The general form of Okuto-Crowell model can be expressed as:

$$\alpha = a(1 + c(T - T_0))E^\gamma \exp\left(-\left(\frac{b(1 + d(T - T_0))}{E}\right)^\gamma\right) \quad 3-21$$

where T_0 is 300 K, T is the temperature, E is the electrical field. a , b , c , d , and γ are fitting constants. The default coefficients listed in Table 3-3 are used in the model due to the wide electric field range of the Okuto-Crowell model.

TABLE 3-3. DEFAULT VALUES FOR OKUTO-CROWELL MODEL

PARAMETERS	Electrons	Holes	Unit
a	0.426	0.243	V^{-1}
b	4.81×10^5	6.53×10^5	V/cm
c	3.05×10^{-4}	5.35×10^{-4}	K^{-1}
d	6.86×10^{-4}	5.67×10^{-4}	K^{-1}
γ	1	1	1
δ	2	2	1
λ	62×10^{-8}	45×10^{-8}	cm
β	0.265283	0.261395	1

Regarding the SRH models, it is necessary to introduce the temperature doping dependencies into the physics section, as discussed earlier in the context of the generation rate of DCR. For the BTBT models, the Schenk model is adopted, as it considers the phonon-assisted band-to-band tunneling [162].

3.4.2. Breakdown Voltage (BV)

After specifying various physical models, the first step of simulations is to find the BV of SPADs. A reverse voltage is applied across the junction, and the range must be

specified properly to prevent convergence problems. To be consistent with the actual layout design, a positive voltage is applied at the cathode, and a constant 0 V is applied to the anode of the SPAD, with a 50k-Ohms serial resistor. The body contact is also tied to 0 V. For the first attempt of the simulation, the voltage at the cathode is set to vary from 0 V to 20 V. Through an iterative process, the doping concentration is adjusted for finding the BV. When the doping concentration of N-well is set to $2.21 \times 10^{17} \text{ cm}^{-3}$. The simulated BV is based on the SPAD structure with detailed dimension parameters shown in Figure 3-5. Reverse I-V curve is shown in Figure 3-6, which indicates the BV of 9.45 V. Note that the heavily doped p-side has little impact on the BV as the doping concentration of the N-well is smaller than the p-side in the order magnitude. Further adjustments of doping concentrations based on the measured results are necessary for an accurate BV.

Initial parameters that are used for simulating the BV, DCR, and PDP of SPAD are shown in Table 3-4.

Table 3-4 Some Initial Parameters for the 1-D SPAD Simulation

N-well_doping	$2.21 \times 10^{17} \text{ cm}^{-3}$
P+_doping	$1 \times 10^{19} \text{ cm}^{-3}$
Diameter	10 μm
Surface light intensity	0.001 W/cm^2
Temperature	300 K
Impact ionization model	Okuto-Crowell
Electron saturation velocity	$1.07 \times 10^7 \text{ cm/s}$ [161]
Electron saturation velocity	$8.37 \times 10^6 \text{ cm/s}$ [161]

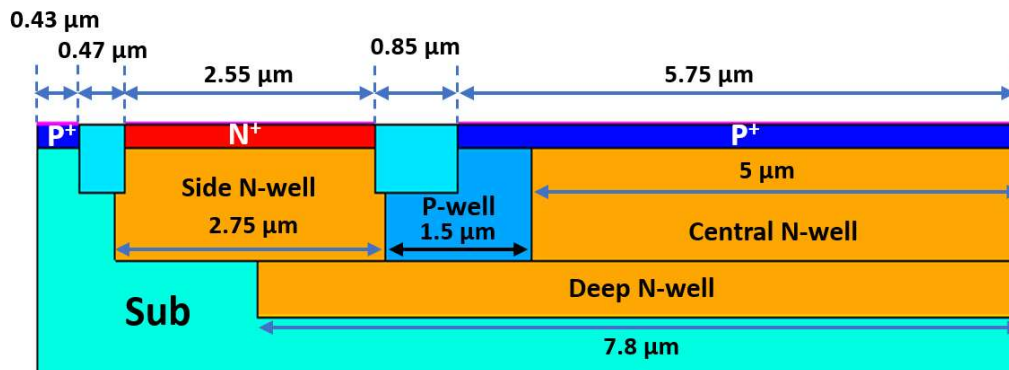


Figure 3-5. SPAD device details used for simulating breakdown voltage.

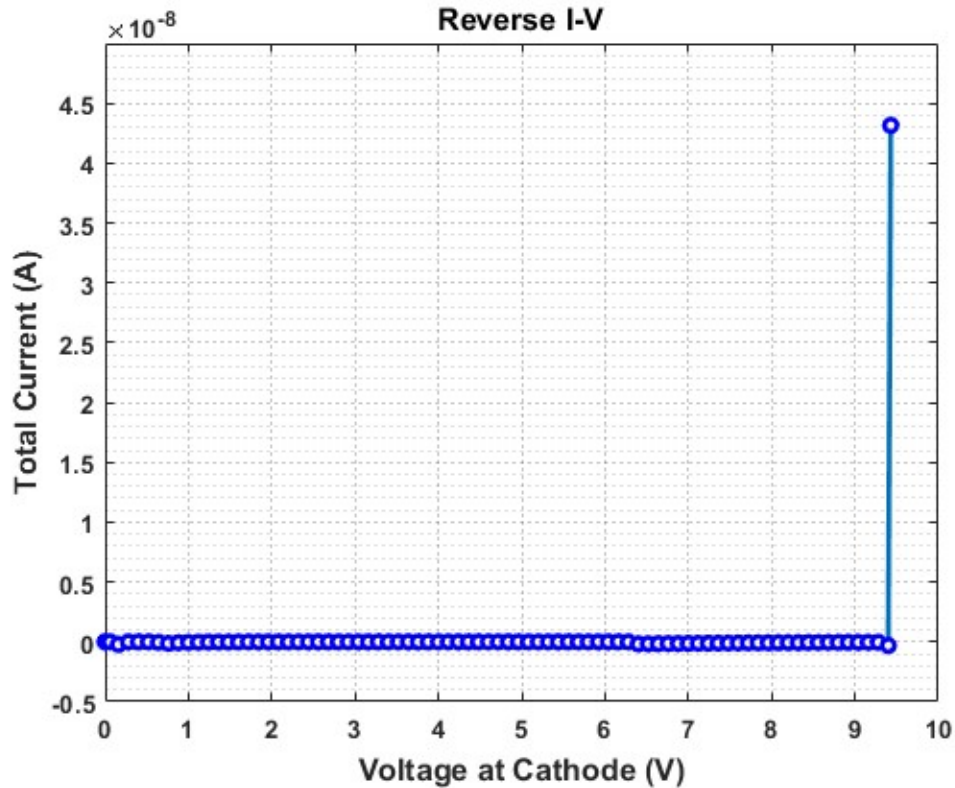


Figure 3-6. Simulated reverse I-V of SPAD

Note that a 50 k Ω serial resistor is connected at the anode which is not visible in the figure.

In addition to plotting the I-V characteristics to find the BV of SPAD, breakdown analysis criteria can be added in the device simulation mainly for validation purpose. In Sentaurus, the breakdown analysis of impact ionizations can calculate the ionization integrals along every path. Among all the ionization paths, the one with the highest ionization integral will be shown, along with the position of the highest electric field. This breakdown analysis can provide designers with a better sense of the simulation results. If the structure, mesh or the physics are not set appropriately, the estimated BV obtained from the breakdown analysis can hardly be consistent with the value obtained from I-V curve.

Based on the simulated BV of the SPAD, excess voltage can be set to bias the device accordingly. To simulate the DCR, voltage dependence is very important as it

can indicate if the BTBT will dominate the total DCR of SPADs. Before that, the avalanche triggering probability needs to be simulated and processed.

3.4.3. Avalanche Triggering Probability

Avalanche triggering probabilities of electrons and holes are obtained by solving the differential equations expressed in Eq. 3-6 and 3-7. To solve the differential equation, the ionization coefficients of electrons and holes need to be extracted from the TCAD. It is already known that both ionization coefficients are dependent on the local electric field. In this case, the electric field of the device can be simulated. Figure 3-7.

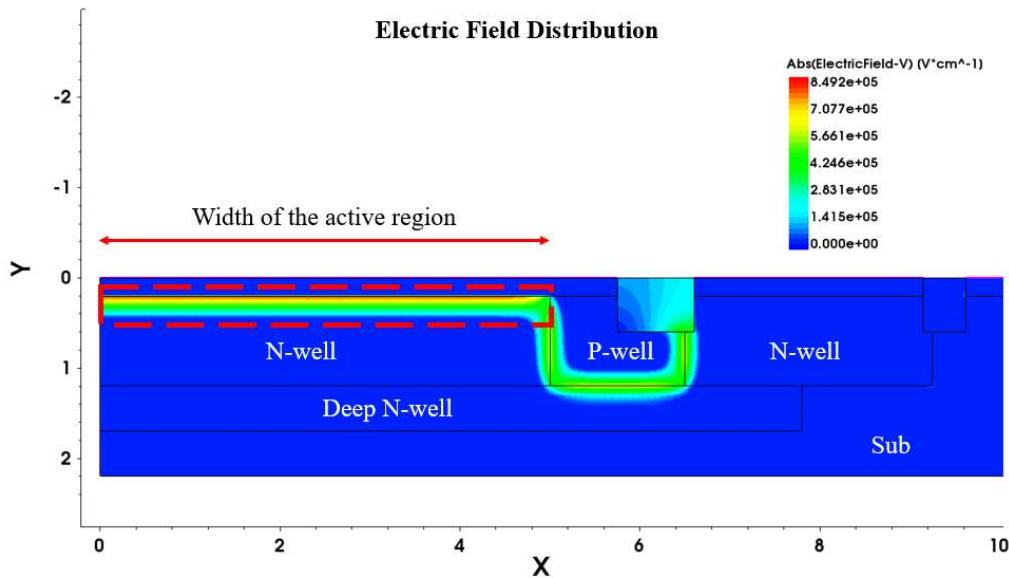


Figure 3-7. Simulated Electric Field of SPAD with a 10-V biasing voltage.

From the figure, the central region has a uniformly distributed electric field across the P+/N-well junction. In this case, the width of the depletion region can be determined by finding the point where the electric field is 0, as shown in Figure 3-8 (a). For the conventional modeling of SPAD's DCR and PDP, the impact ionization coefficients across the junction are extracted from the TCAD, where the electron ionization coefficient α_e is shown in Figure 3-8 (b). Based on the simulated electric field, the width of the actual depletion region, and the ionization coefficients, the data along the line can be extracted the calculation of avalanche triggering probability. The extracted electron and hole ionization coefficients are fitted using MATLAB. Since they are also

position dependent, they are combined with the differential Eq. 3-6 and Eq. 3-7 to solve the position-dependent triggering probability $P_p(x)$, $P_n(x)$, and $P_t(x)$.

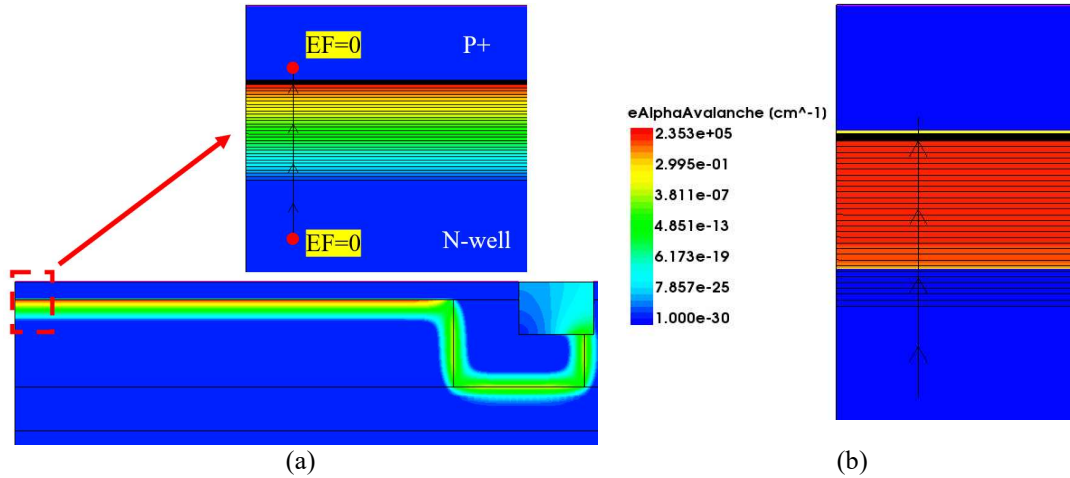


Figure 3-8. Specification of (a) depletion region's width and (b) electron ionization coefficient.

In the MATLAB, to solve the differential equations simultaneously, the **BVP4C** solver can be employed with the two known boundary conditions. The simulated avalanche triggering probability is shown in Figure 3-9. From the figure, the electron's avalanche triggering probability has the highest value compared to the hole's avalanche triggering probability, which is as expected since the impact ionization coefficients of electrons are higher than the hole impact ionization coefficients. Consequently, the total avalanche triggering probability P_t is higher near the P side of the depletion region since electrons at the P side of the depletion region can explore a longer accelerating path, thus having higher probability to initiate avalanching events than the electrons at the N side. Note that the distribution of the avalanche triggering probability is for this P+/N-well junction only. For other types of junctions and the line directions, this distribution may vary. Also, with a higher biasing voltage, the avalanche triggering probability will also increase, due to the higher impact ionization coefficients. However, the electric field must not exceed the valid range of the avalanche models used in the Sentaurus. For the SPAD designed in 65 nm standard CMOS technology, the excess voltages applied are usually smaller than 1 V, especially for the active quench and reset SPAD because the MOSFETs may be destroyed if a high voltage output is directly connected to them.

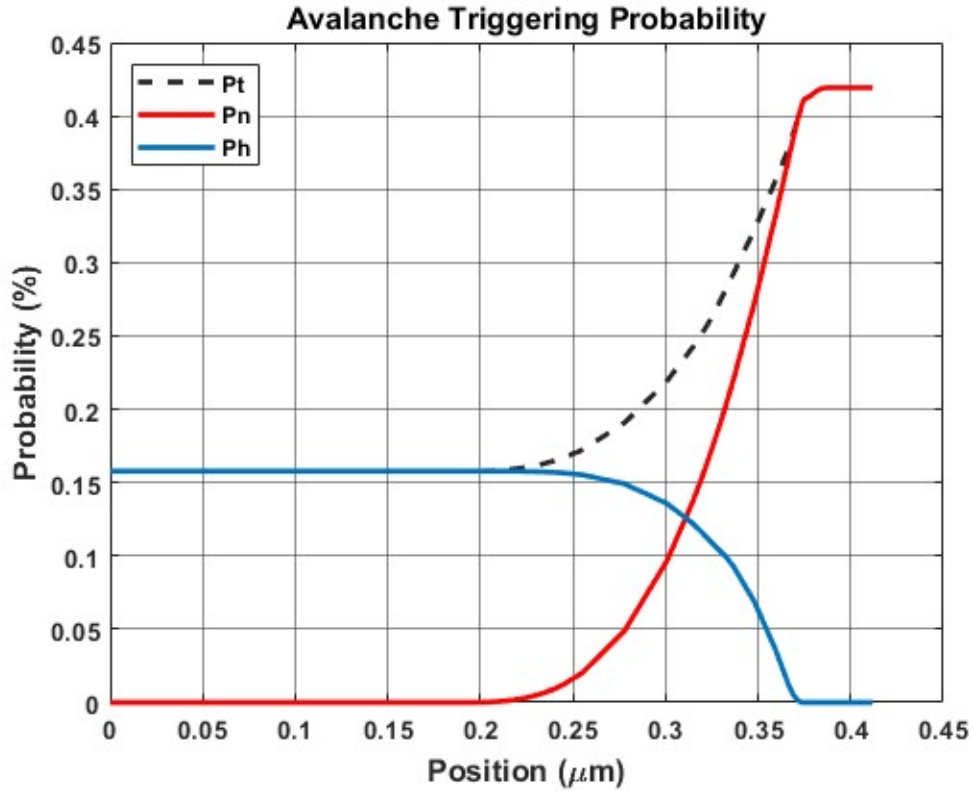


Figure 3-9. Simulated avalanche triggering probability in the depletion region.

3.4.4. Dark Count Rate (DCR)

Upon the finish of modeling avalanche triggering probability, the generation rate of SRH and BTBT can be simulated to obtain the DCR. The simulation of the generation rate due to different mechanisms can be directly extracted from the TCAD. From the previous discussion, the SRH is an enhanced model that considers the field enhancement factor. In the simulation, the trap energy band is set to locate at the center of the band gap, serving as efficient generation and recombination center. Similar to the simulation of avalanche triggering probability, we only focus on the generation rate in the depletion region as diffusion has little influence on the total DCR and PDP, especially for the advanced standard CMOS technology. However, when modeling some devices that are specially designed for long-wavelength detection, the diffusion may not be negligible as the doping concentration could be much lower and the diffusion may have a significant contribution on the total DCR and PDP. The simulated

SRH generation rate G_{srh} is shown in Figure 3-10. Note that the SRH generation rate here doesn't include field dependence.

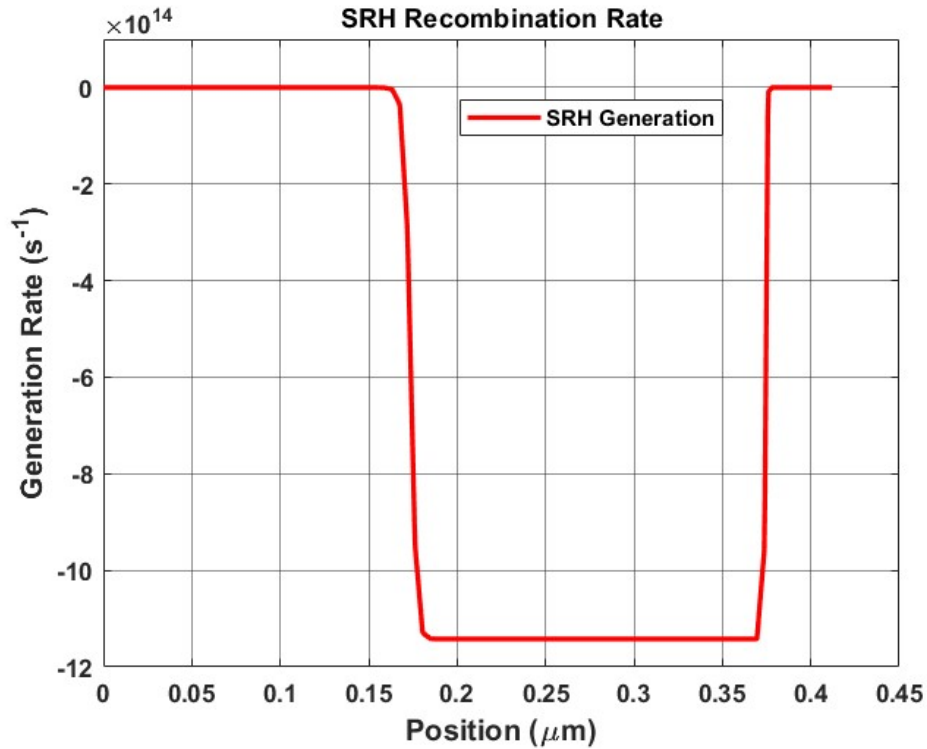


Figure 3-10. Simulated SRH generation rate across the depletion region
Similarly, the generation rate due to the band-to-band tunneling effect is simulated as shown in Figure 3-11.

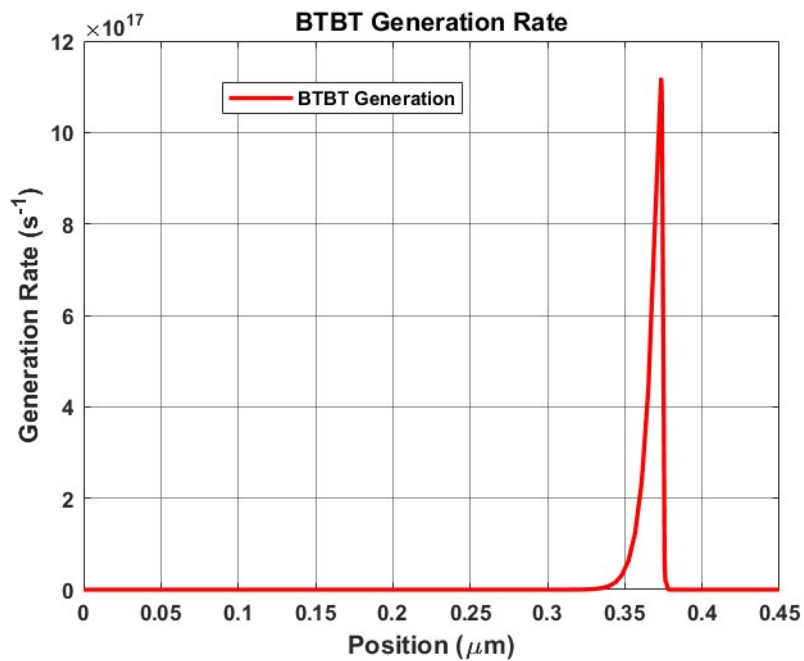


Figure 3-11. Simulated BTBT generation rate across the depletion region

Note that both figures are simulated based on the 10 V biasing voltage condition. From the comparison between the SRH generation rate and BTBT generation rate at a 10 V bias, the BTBT generation rate is much higher than the SRH generation rate near the junction interface, where the electric field is high. However, for the entire depletion region, the SRH generation rate has higher value than the BTBT generation rate for most of the time. So, it is not straightforward to see their contribution to the total DCR of SPADs. Therefore, it is necessary to integrate the generation rate and the avalanche triggering probability along the depletion region, given by:

$$DCR_{SRH} = \int_0^d |G_{SRH}(x) \times P_t(x)| dx \quad 3-22$$

$$DCR_{BTBT} = \int_0^d |G_{BTBT}(x) \times P_t(x)| dx \quad 3-23$$

Term d is the width of the depletion region, which is extracted directly from TCAD. The simulated DCR caused by intrinsic SRH and BTBT mechanisms at a 10 V bias are 5.03×10^1 cps/ μm^2 and 4.26×10^3 cps/ μm^2 , respectively. Under such biasing voltage, the DCR caused by BTBT mechanism is much larger than the SRH-induced DCR, in this case, the BTBT mechanism dominates the total DCR generation. The initial results also indicated the doping concentration may be assumed much higher than that in the real cases. Trap-assisted tunneling can be introduced to the traditional SRH model, thus having electric field dependency. This is called the field-enhancement in SRH model. After introducing this field-enhancement factor into SRH model. The comparison between the traditional SRH model and the SRH model with field-enhancement factor is shown in Figure 3-12. Since the figure is plotted in log scale, the generation rate of the SRH mechanism with field enhancement is much larger than the traditional SRH generation rate when the electric field is high. So, in the modeling of SPAD's DCR, the traditional SRH generation rate is almost negligible compared to the SRH TAT generation rate.

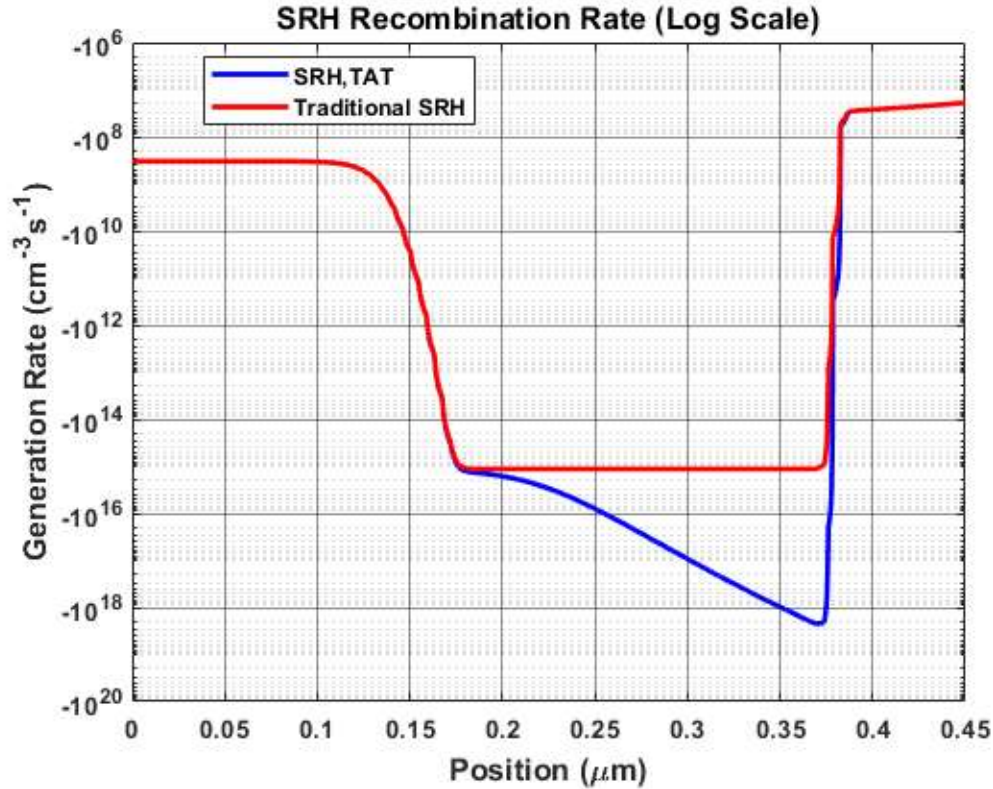


Figure 3-12. Comparison between SRH generation rate and the field enhanced SRH generation rate

For the abovementioned simulation, the basic parameters follow the values listed in Table 3-1 to Table 3-4. Now both the SRH generation and the BTBT generation mechanisms exhibit a strong electric field dependence. Therefore, a voltage dependence of DCR is crucial for determining the contributions from different mechanisms. With the simulated BV of SPAD being 9.45 V now. Voltages from 9 V to 10.8 V are applied to the SPADs for simulating the voltage dependence of DCR with a step of 0.1 V. Following a similar step, the DCR are simulated at a varying bias. The simulated results are shown in Figure 3-13, with curves of the DCR caused by different mechanisms clearly annotated. In the applied voltage range, the contributions from SRH-TAT mechanism are larger than the BTBT mechanism, which is inconsistent with the results from Ref. [157]. From the plot of the DCR voltage dependence, the BTBT-induced DCR should become dominant at a much higher voltage due to the exponential increasing trend. However, currently we only focus on the SPADs that are biased at lower voltages to avoid destroying the following MOSFETs. And the initial assumption

of E_{trap} at the middle of the bandgap may not be suitable for the current SPAD model, as an unreasonably high TAT generation rate was simulated.

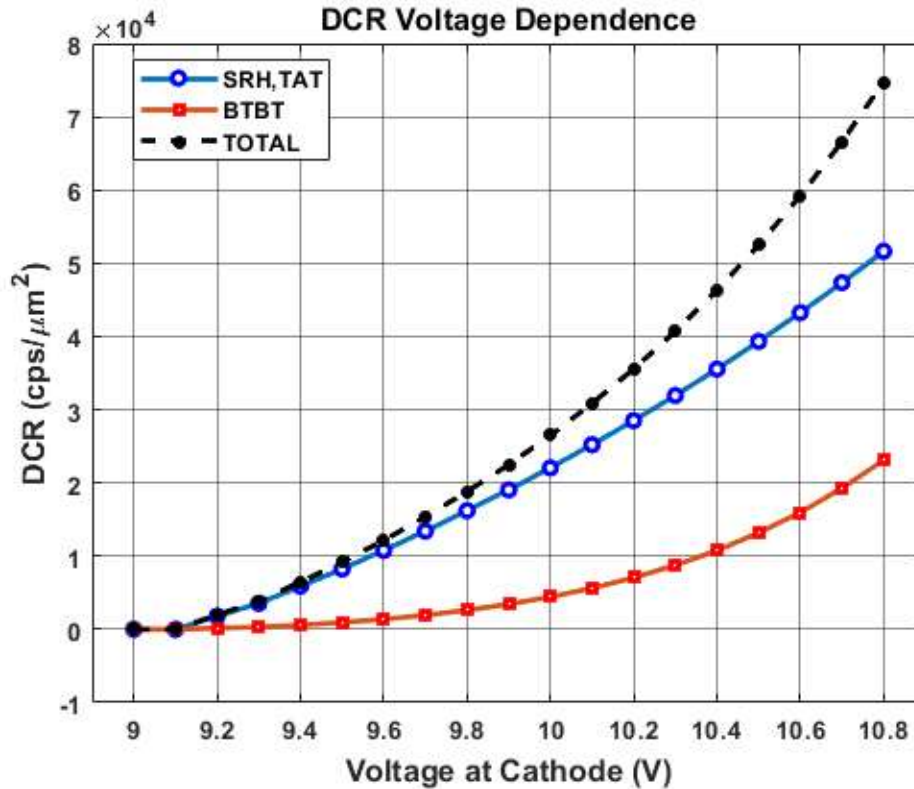


Figure 3-13. Simulated DCR voltage dependence of SPAD based on initial BV of 9.45 V

Now, the dark counts of SPADs are modeled, with the consideration of different mechanisms and detailed simulation settings. However, with the initial results obtained from simulations, the unrealistically high DCR caused by TAT mechanism may indicate a significant deviation to the real cases. One of the major issues is the access to real trap information. Therefore, in the future modeling process, the TAT process may be excluded from the model to prevent errors arising from inadequate assumptions.

3.4.5. Photon Detection Probability (PDP)

Different from the solely electric field simulations required for DCR modeling, an optical simulation process is needed in the PDP modeling. Consequently, additional wavelength dependence may need to be modeled accordingly. In the SDEVICE tool, the raytracing method is adopted to simulate photon absorption. From the simulation, the absorbed photon density can be extracted along specific cutlines or streamlines. For

the conventional 1-D PDP model, the integration between the absorption probability and avalanche probability is executed along the depletion region. During the modeling phase of PDP, the impact of DCR can just be ignored since only photon-generated carriers are taken into consideration for the calculation. However, it can be totally different in the PDP measurements.

The photon absorption probability P_{op} is modeled by defining the intensity of the incident light and simulating the absorbed photon density at specific positions. The light source is illuminated vertically to the surface of the SPAD, with a light intensity of 0.001 W/cm^2 . The illumination window is limited to the entire active area. 20000 rays are traced by considering both the computational time and consistency. The maximum depth of the raytracing is limited to $1000 \mu\text{m}$, and the raytracing will also stop where the light intensity has dropped below 10^{-5} W/cm^2 . The simulated photon absorption at different wavelengths is shown in Figure 3-14. Note that the right side is close to the surface of the SPAD, while the left side is located deep within the device. For different wavelengths, the absorbed photon density all exhibits exponential decay. A larger proportion of photon absorption occurs close to the surface of the device. However, for light with longer wavelengths, the absorbed photon density is higher than the light with short wavelengths at a deeper location, which is consistent with the theoretical absorption law. Therefore, some SPADs are intentionally designed with a long depletion region with epi-layers or using backside-illuminated (BSI) technologies, to have high detection efficiencies at near infrared (NIR) spectrums.

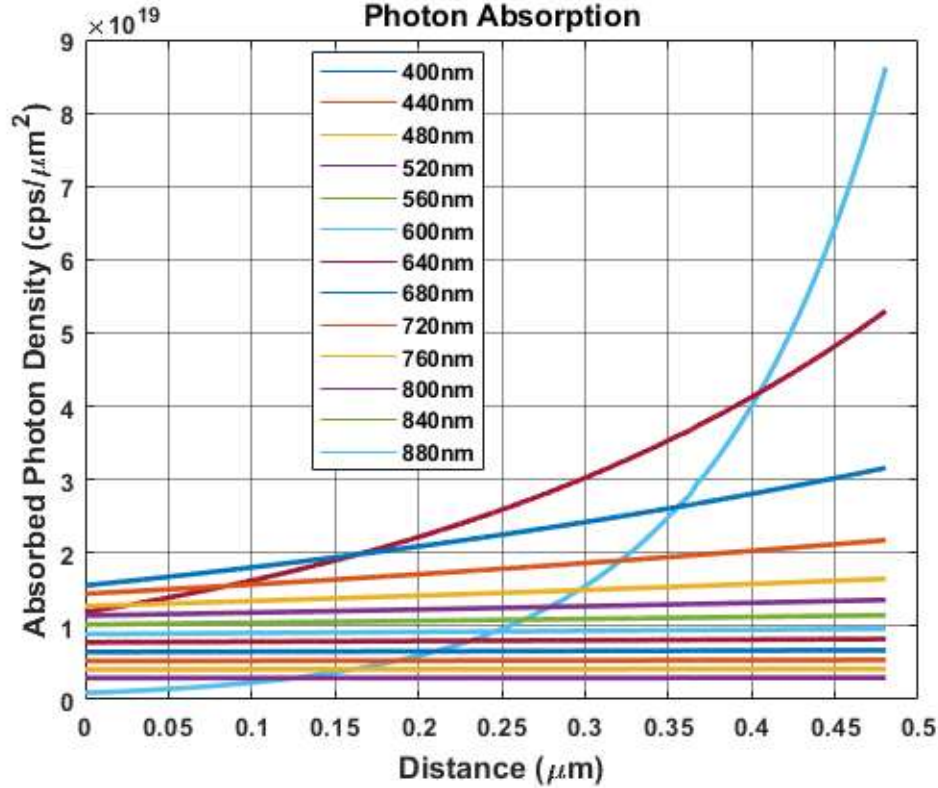


Figure 3-14. Simulated Photon absorption rate of different wavelengths

With the obtained absorption photon rate, the probability can be calculated according to the Eq. 3-23,

$$P_{op} = \frac{N_{op}}{N_{surface}} = \frac{N_{op} \times 1 \mu m}{I_{surface} \times \lambda / hc}, \quad 3-24$$

where N_{op} is the simulated absorption rate, $1 \mu m$ is the virtual depth in the z-direction specified by TCAD, $I_{surface}$ is the incident photon intensity at the surface of the SPAD. λ , h and c , are wavelengths, Planck's Constant, and vacuum light speed, respectively. Now both P_{op} and the avalanche triggering probability P_t are dimensionless factor, an integration can thus be calculated along the depletion region, therefore, PDP is therefore simulated.

3.5. Extend from 1-D model to 2-D model

In the previous modeling process of SPAD's dark carrier generation rate, DCR, photon absorption probability, and the PDP of SPAD, 1-D models were used due to the simplicity and the availability of various models. When the size of SPAD is large, the

1-D simplification is acceptable as the active region has a large uniform area. However, with the shrinking size in the advanced technology nodes, SPAD sizes become progressively smaller. Therefore, the edge effect due to the reduced electric field may have more significant influence on the overall PDP and DCR of SPADs. For example, a SPAD pixel with only 1 μm -diameter has been reported to have significantly lower PDP ($\sim 15\%$ at 3.2 V excess voltage bias), compared to other larger SPADs based on 130 nm technologies [163].

To achieve more accurate prediction regarding the SPAD's performance, a 2-D simulation process is being extended from the current 1-D DCR and PDP model. For comparison purposes, the 2-D simulated results will be compared with both the 1-D simulated results and measured data. For a single SPAD, instead of a simple cutline used for extracting data, multiple streamlines are created following the actual directions of the electric field at any position in the depletion region. Considering the computational time and cost, a total of $N=25$ streamlines are generated following the direction of local electric field, for each half-structure of the SPAD. The boundary condition for each of these streamlines remains $E=0$. Therefore, each streamline can represent an impact ionization path within the depletion region. The cross-sectional view of SPADs with streamlines are shown Figure 3-15. Since these streamlines follow the direction of local electric field, an estimation of the uniform region can be made upon the creation of these lines. Near the edge of the active region, the directions of electric field gradually deviates from straight lines, as shown in Figure 3-15.

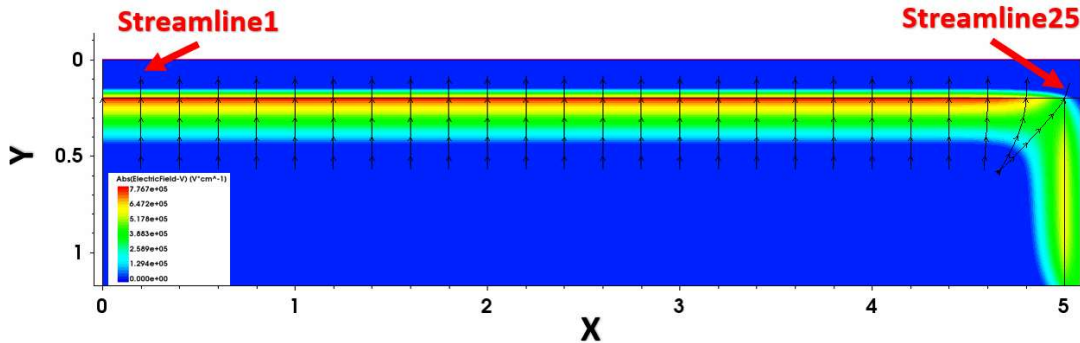


Figure 3-15. 25 Streamlines created in the 2-D SPAD model.

For each streamline, ionization coefficients α_e and α_h , SRH generation rate $G_{srh,i}$, band to band tunneling generation rate $G_{b2b,i}$, and photon absorption rate are extracted and processed in MATLAB to obtain DCR_i and PDP_i .

For the avalanche triggering probability P_t obtained by solving the differential equations, the comparison among several streamlines is shown in Figure 3-16.

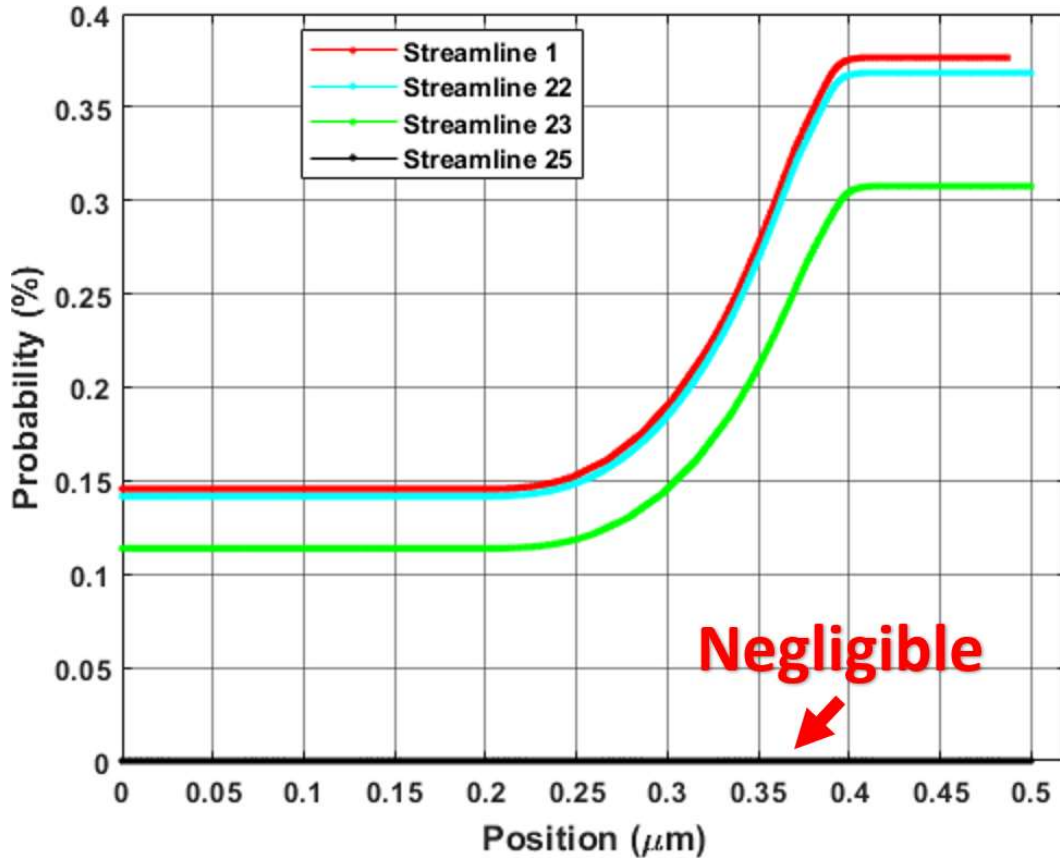


Figure 3-16. Avalanche triggering probability P_t of different streamlines of a 10- μm -diameter SPAD at 10.5 V bias

It has shown an obvious decrease in the avalanche triggering probability P_t as the streamline approaches the edge region. For the outermost streamline (Streamline 25), the total avalanche triggering probability becomes almost negligible. Therefore, both the DCR and PDP are decreasing from the central region to the edge region since they are both highly related to the avalanche triggering probability. To have an estimation of the overall DCR and PDP of the SPAD, an average of the 25 values of each parameter is computed. With the implementation of the 2-D model, the simulated value of each streamline's DCR and PDP are shown in Figure 3-17 (a) and Figure 3-17 (b).

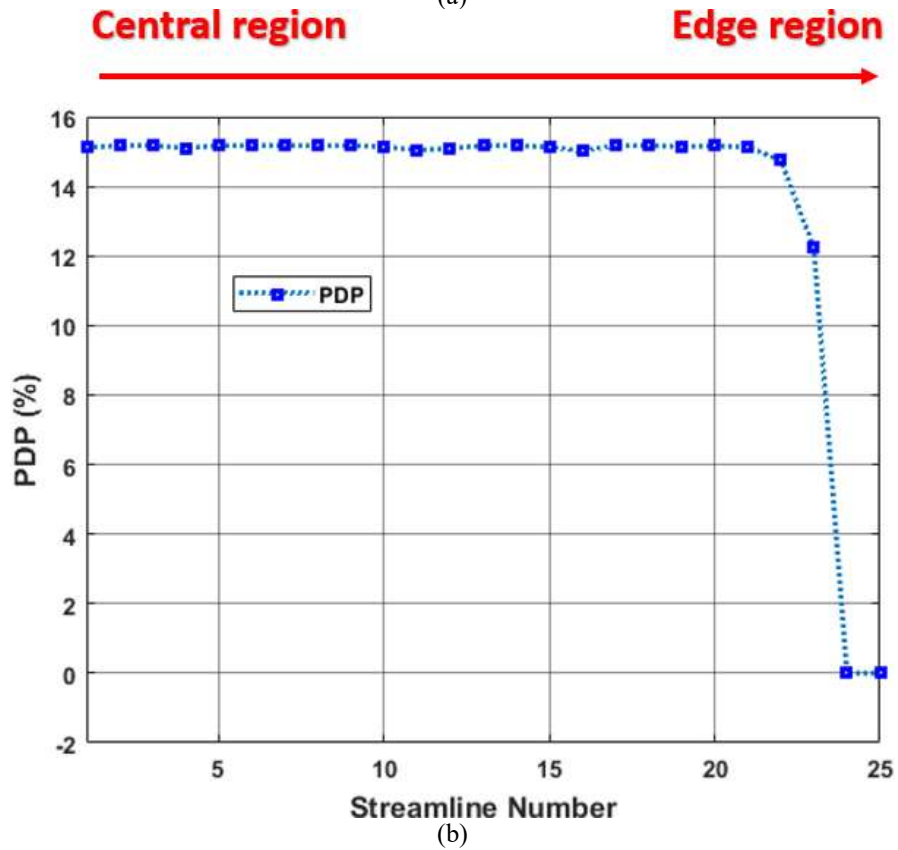
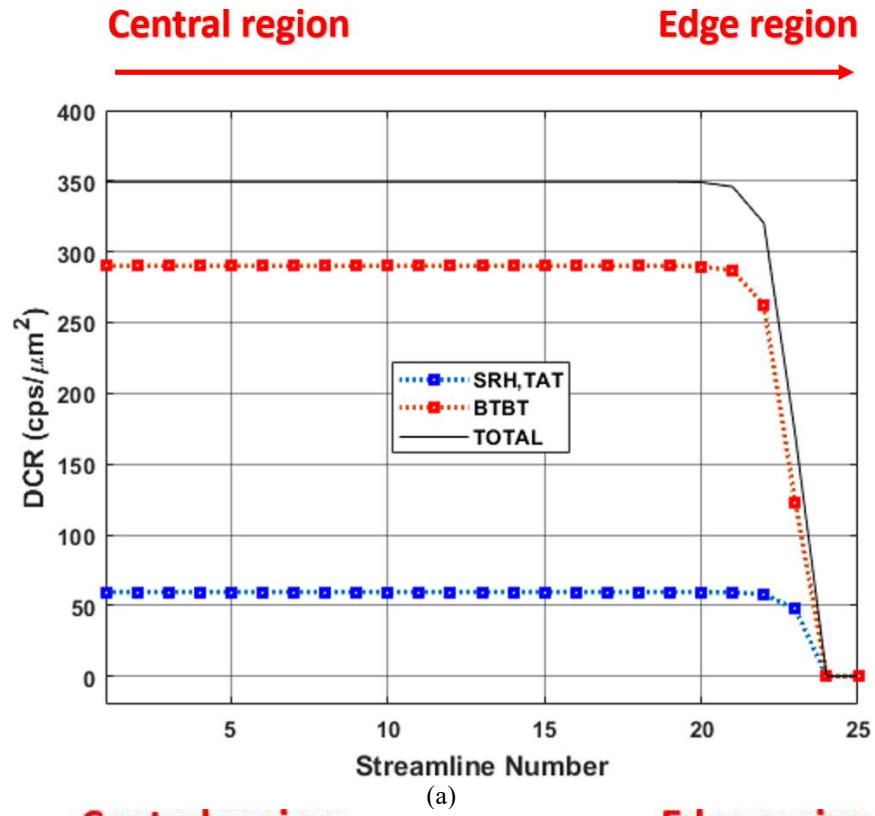


Figure 3-17. (a) Dark count rate of each streamline and (b) Photon detection probability of each streamline of a 10- μm -diameter SPAD at 10.5 V bias.

Both figures illustrated a clear degradation of values from the central region to the edge region. This has indicated the influence of the edge effect. However, for the SPAD with different sizes, the influence of the edge field degradation may be of different significance. For example, if a SPAD has a large uniform active region, the edge region is much smaller than the central region, thus being negligible. However, if the SPAD is small, the edge region can have more dominant effects on the overall DCR and PDP of a SPAD. In this case, trade-offs among the size, detection efficiency, and the noise performance must be considered for an optimized design. Especially, high integration and more pixel numbers are desired in SPAD arrays since they can be cost-effective and can provide high image resolution, as discussed in Chapter 2. Therefore, 5 SPADs with different sizes of active region are modeled in the TCAD by utilizing the proposed 2-D simulation models.

Five SPADs were modeled with the active region diameters of 6 μm , 10 μm , 12 μm , 16 μm , and 20 μm , respectively, as shown in Figure 3-18. For every individual SPAD, all the parameters required for calculations of DCR and PDP are extracted along the 25 streamlines. For each streamline, the PDP and DCR can be represented by PDP_i and DCR_i . For each modeled SPAD (S1-S5), the position x can be normalized to individual's radius, as shown in Figure 3-19. The simulated DCR_i of the 5 SPADs were presented based on the normalized x -axis in Figure 3-20.

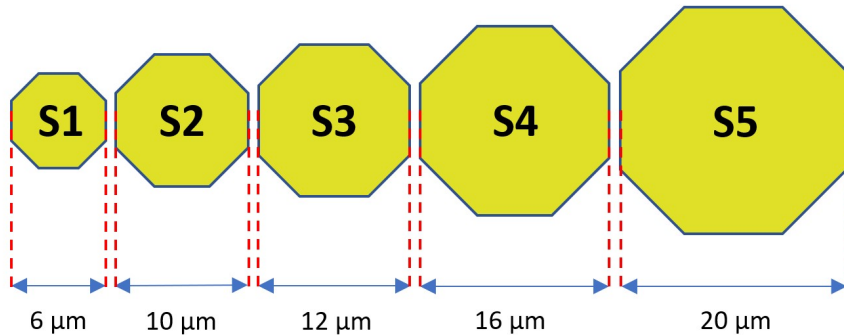


Figure 3-18. 5 SPAD with diameter of 6 μm , 10 μm , 12 μm , 16 μm , 20 μm .

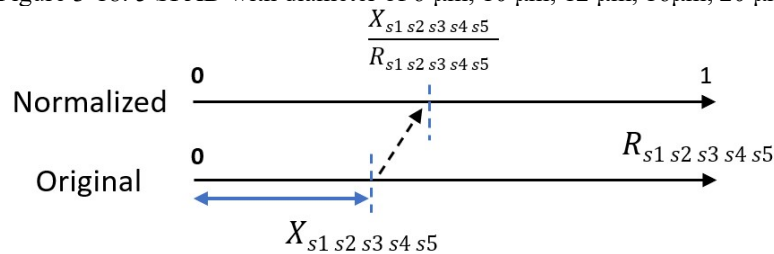


Figure 3-19. Original axis and normalized axis for plotting DCR versus position.

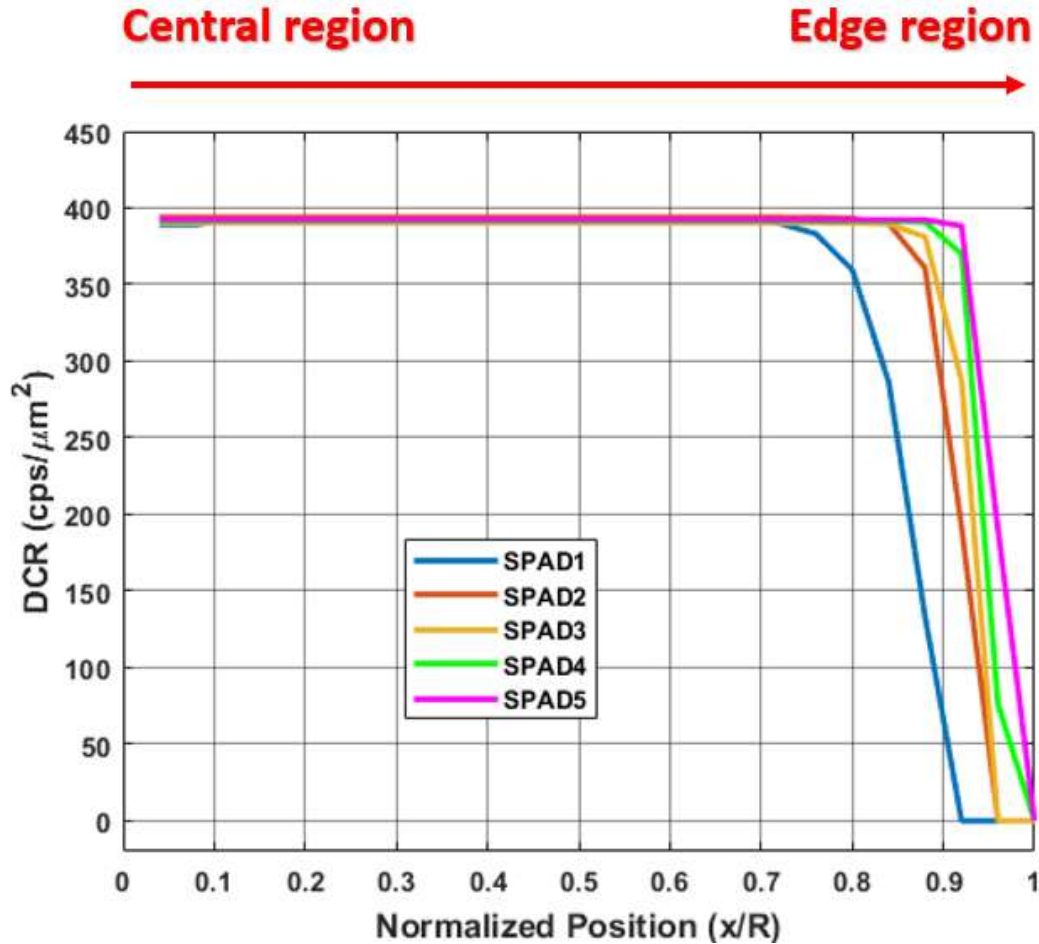


Figure 3-20. The simulated normalized DCR of 5 SPADs at 10.55 V bias

Similarly, the decrease of PDP is also different for the SPADs with different sizes. In Figure 3-21, the simulated PDP_i of the 5 SPADs were compared at a fixed biasing voltage and a wavelength of 400 nm. With the additional photon absorption process, the edge effect on the detection efficiency still exists. The incident angle of the light was fixed to be 90 degrees. However, the light emitted from different angles may have certain influences on the total detection efficiency in real cases.

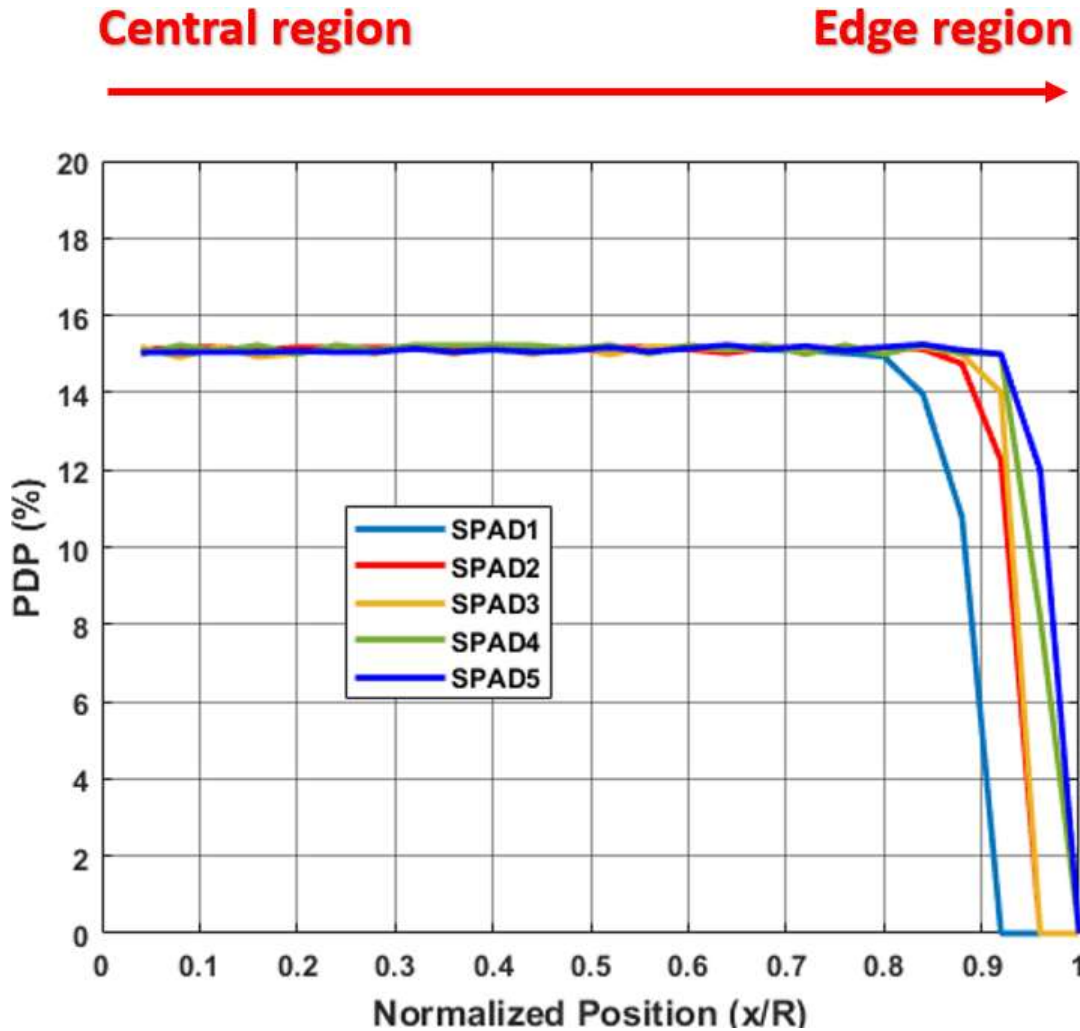


Figure 3-21. Photon detection probability of different streamlines of a 5 SPADs at 10.55 V bias and wavelength of 400 nm.

Note that the decrease of the DCR and PDP appears earlier in the smaller SPADs than the larger SPADs. To have an overall estimation of the DCR and PDP of each SPAD. With a similar method, the DCR of each SPAD can be normalized to the DCR of the largest SPAD, which has a diameter of 20 μm , as shown in Figure 3-22. For SPAD 2 to SPAD 4, there isn't too much difference (less than 5 % decrease); however, for the smallest SPAD, there is an obvious decrease (more than 10 %), which indicating the existence of edge effect. Considering the measurement variations, a distinct difference in DCR may be witnessed on the smallest SPAD: S1.

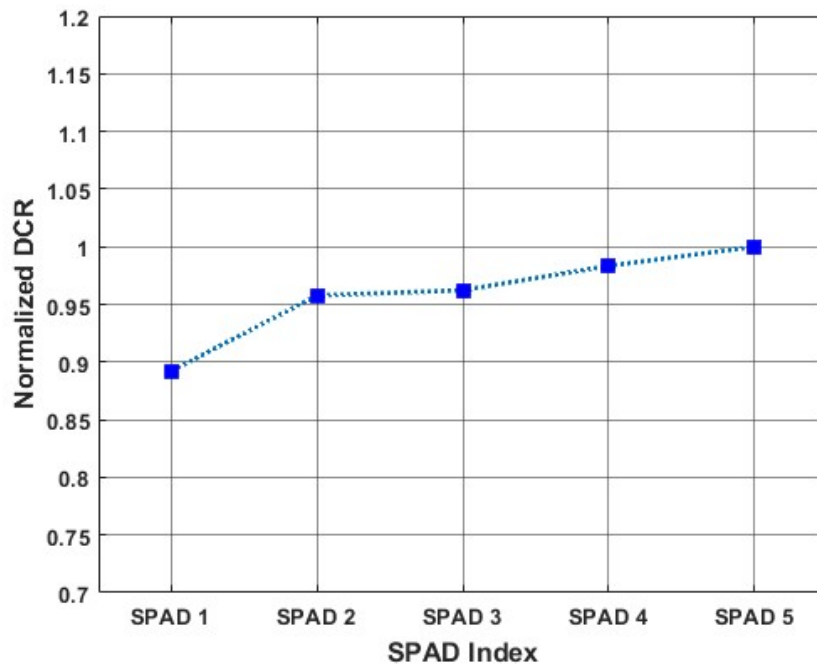


Figure 3-22. Normalized DCR of different SPADs

The simulated averaging PDP of SPAD1 to SPAD5 can also be presented using $PDP_{avg,n}$ where n is the index number of the 5 SPADs. At a specific wavelength of 400 nm, the comparison between different SPADs is shown in Figure 3-23.

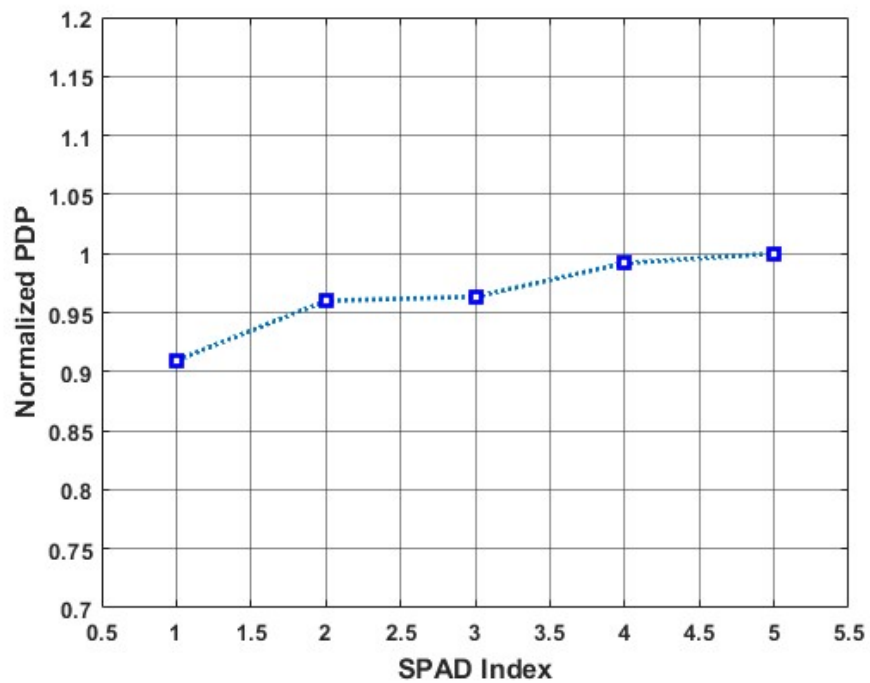


Figure 3-23. Normalized PDP of different SPADs

From Figure 3-21 and Figure 3-23, the DCR and PDP degradation of small SPADs is more obvious than large SPADs. By normalizing $DCR_{avg,n}$ and $PDP_{avg,n}$ against $DCR_{avg,5}$ and $PDP_{avg,5}$, a clear edge effect of each SPAD has been demonstrated. From this figure, a very small SPAD can have a significantly decreased PDP. Based on the simulation of DCR and PDP utilizing the 2-D SPAD model, designers can develop general idea of choosing the right size and design specifications. Following the proposed 2-D modeling process, the predicted DCR may be closer to the real value obtained from measurements. However, additional efforts are needed to improve the efficiency of the proposed 2-D modeling process.

3.6. Automated Simulation Process

When the simulations of SPAD's DCR and PDP are extended from 1-D to 2-D, both the simulation time and the data extraction time have increased a lot. Especially, 25 streamlines of each device need to be created manually every time. For the 5 SPADs with varying sizes, the intervals between neighboring streamlines are also of different values, which further increases the total time needed for a complete simulation. In this case, the simulations of SPADs can be very time-consuming, which is not efficient for the design and optimization of SPADs. Recently, emerging machine learning (ML) techniques are combined with traditional modeling work due to their high efficiency, accuracy, and low cost. Some typical ML-TCAD combined cases include the prediction of the defect location in Fin-FET technologies, process variations, breakdown, and even circuit design [164]–[167]. However, there have been few studies on SPADs that combine ML with TCAD simulations, due to the lack of available data and rigorous simulation process. In this section, a fully automated TCAD simulation is introduced, which can save a lot of time that is needed for editing, data extraction, and data processing.

A simple diagram is shown in Figure 3-24. For certain parameters, a specific range can be set as input, and the simulated results can be extracted exactly after the simulation. And the data will be stored in Excel files for processing in MATLAB.

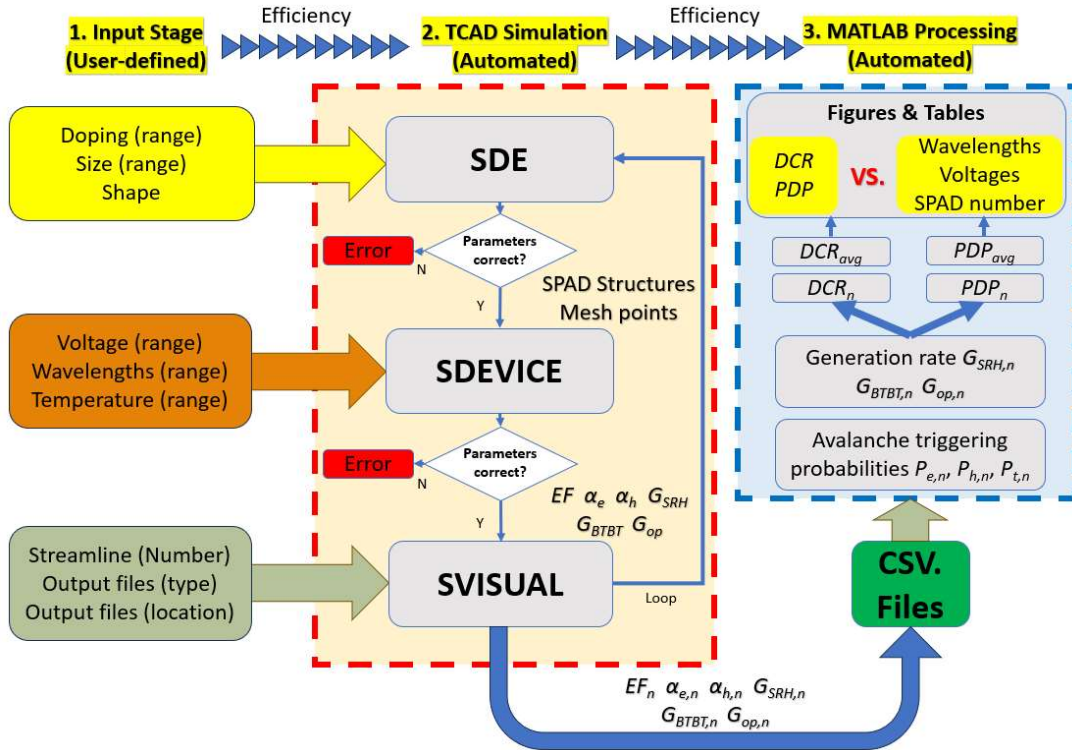


Figure 3-24. Proposed automated simulation process of 2-D SPAD model

With the simulation automation, there is no need for continuous monitoring and modifying parameters during the process. For example, to investigate the edge effect on DCR and PDP, a diameter range can be simply specified in the TCAD before running simulations. Subsequently, a pre-defined number of streamlines can be automatically generated at a specific step size. Finally, all the pre-defined parameters can be automatically extracted to Excel file for each streamline. The simulation automation is based on `tcl` commands within **SDE**, **SDEVICE**, and **SVISUAL**. For the range of structure-related parameters, it can be edited in the **SDE**, and the electrical aspects can be specified in the **SDEVICE**, such as voltages, temperatures, and light intensity. For the **SVISUAL** part, commands are edited to extract certain parameters automatically. Furthermore, the figures and tables can also be generated which satisfy the required sizes and styles. Detailed codes of automated data visualization, extraction and MATLAB programs are attached in Appendix B, together with the explanation of important commands.

With the help of the automated simulation process in TCAD, a bunch of data can be generated by varying different parameters of SPADs. These datasets can potentially

be used to train certain ML models in the future, thus further optimizing SPAD designs in a more efficient way.

Chapter 4

DESIGN AND OPTIMIZATION OF CMOS

SPADS AND CIRCUITS

From the previous simulation results, the 2-D simulation results that consider the edge effect have shown lower DCR and PDP for SPADs. In this chapter, SPADs and the related front-end circuits are designed to validate the effectiveness of the model. Different from the simulations, many technology-related issues must be considered in the design of SPADs based on 65 nm standard CMOS technology. Compared to CMOS image sensor (CIS) technologies and custom CMOS technologies, standard CMOS technologies are cheaper and can be easily integrated with digital circuits such as time-to-digital converters (TDCs). In this chapter, introductions to the designing procedure and key considerations of SPADs based on 65 nm technologies are discussed first. Then, the SPAD pixels designed based on passive quench and reset (PQR) configurations are presented. In addition, the design and simulations of output buffers are introduced, along with a discussion on the measurement-related considerations. The measurements of the designed SPADs are presented and compared with the simulation results, including BV, DCR, and PDP of different SPADs. Finally, discussions and analyses of the measurement setup, variations, and potential improvements are provided at the end of the chapter.

4.1. SPAD Structure Design in 65nm CMOS Technology

SPADs designed based on 65nm CMOS technology can achieve low fabrication costs, high integration, and reasonable detection efficiencies. However, when it comes to layout design, there are many features to consider for improving the SPAD's performance. Unlike custom technologies, the technology-related parameters are not

editable in the design of SPADs based on standard CMOS technologies, such as the doping concentration, junction depth, and the availability of anti-reflection-coating (ARC) layers. However, the size and the structures still have a significant impact on the overall performance, such as the DCR, PDP, and the area efficiency. One of the most important differences between simulation and realistic SPAD design, regarding the SPAD structure, is the existence of inter-metal-dielectric (IMD) layers. These layers above the SPAD can affect the transmission of light signals. In the 65 nm technology used, there are 9 metal layers in total. A cross-sectional view of the SPADs with multiple layers is already shown in Figure. 2-6. While multiple metal layers are very convenient for designers to route interconnections, they can have very complex influences on the optical properties of SPADs. Standing waves can form during the transmission of the light, thus introducing ripples to the PDP wavelength dependence plot [168], [169]. Therefore, to reduce the impact on photon absorption in the active region, metal layers should be carefully designed.

4.2. SPAD Design

Since there is no standard cell of SPADs in the TSMC 65 nm standard CMOS library, each layer and region of SPADs must be designed by users. The first consideration is the geometric shape of the SPAD. Based on the 5 SPAD structures modeled in Chapter 3, there are three different shapes that can be designed for the SPAD layout: rectangular shape, circular shape, and octagonal shape. All three shapes have good symmetry, making them suitable for comparison with the simulation results based on 2-D structures. However, rectangular SPADs may suffer from the high possibility of premature edge breakdown (PEB) at four corners. A circular SPAD may be a good option, however, it is not allowed to have curved regions in the TSMC 65nm standard CMOS technology. In this case, regular octagonal SPADs become an ideal alternative due to the good geometric symmetry and reduced PEB possibility. Following the 2-D structures in simulation, an octagonal shape for the central N-well is designed as the active region of the SPAD. It is connected to the surrounding N-wells through the implementation of deep N-well, as shown in Figure 4-1 (a). To apply voltage across the junction, P⁺ and N⁺ regions must be defined before adding the

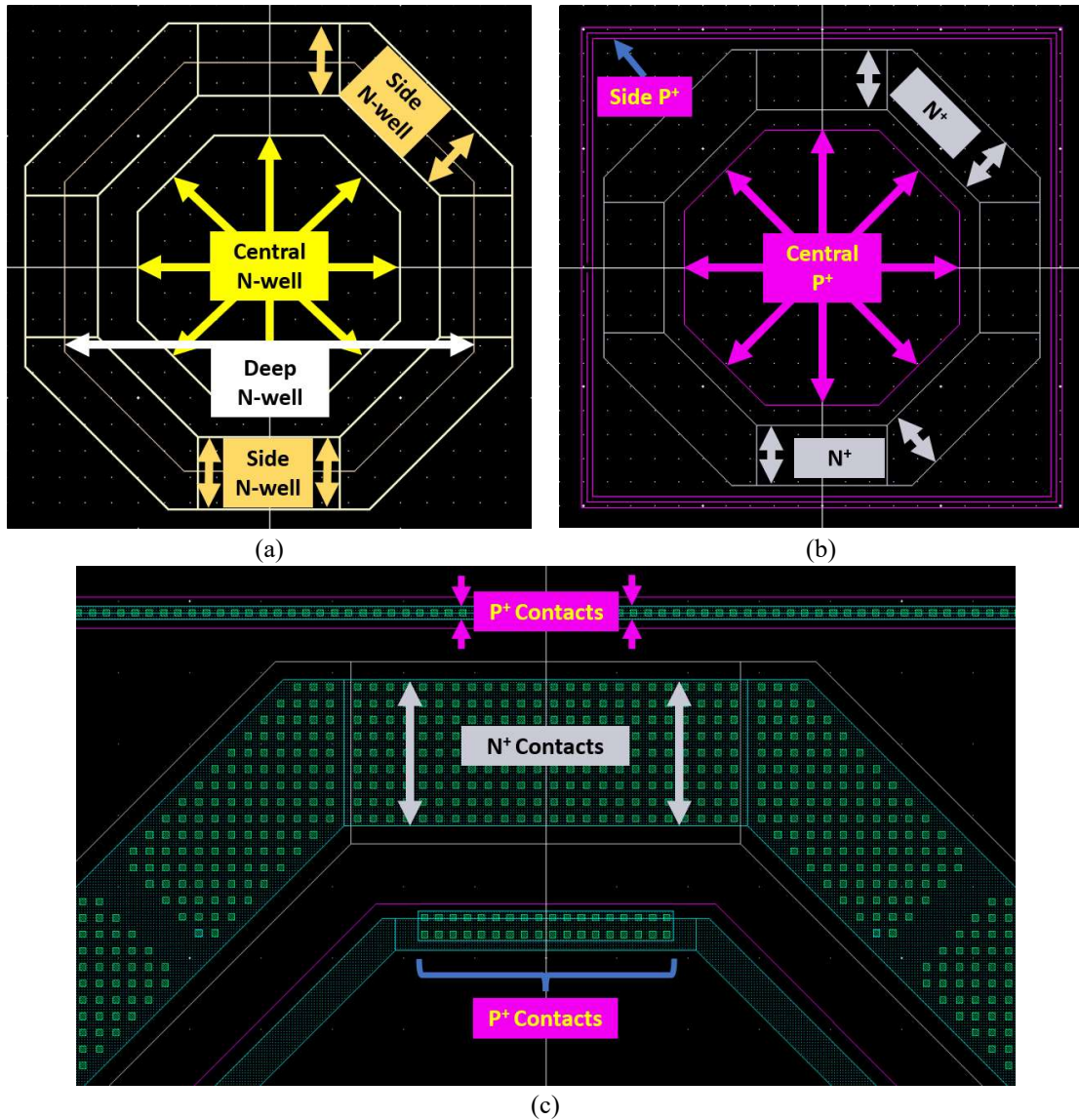


Figure 4-1. Layout design of a single SPAD (a) N-well regions; (b) N^+ and P^+ regions; (c) Metal 1 and contacts.

contacts and metal layers. The P^+ region of the central active region is also designed to have an octagonal shape, and the P^+ region for the substrate contact is designed with a rectangular shape, which can also be referred to as the ‘guard ring’. The designed N^+ and P^+ regions are shown in Figure 4-1 (b). Note that the P-well regions are automatically set where there is no defined N-well. After defining these basic doped regions, contacts are needed to connect the highly doped regions with the metals. In Figure 4-1 (c), Metal 1 and contacts for P^+ regions and N^+ regions are shown. Note that the contacts for N^+ regions cover a larger area than the contacts for the P^+ region since

most of the P^+ region is inside the active region. Ideally, more contacts are desired when a large current is expected to flow through.

To ensure that incident photons are mostly absorbed mostly in the active region, a blocking layer is designed above the SPAD, leaving only an opening window that is slightly larger than the active region, as shown in Figure 4-2 (a). In addition to the specially designed opening window for the active region, two special layers RH and RPO are needed to prevent the silicidation above the active region, as shown in Figure 4-2 (b). The RPO region is the same size as the total active region and the RH region is slightly larger to satisfy the design rules.

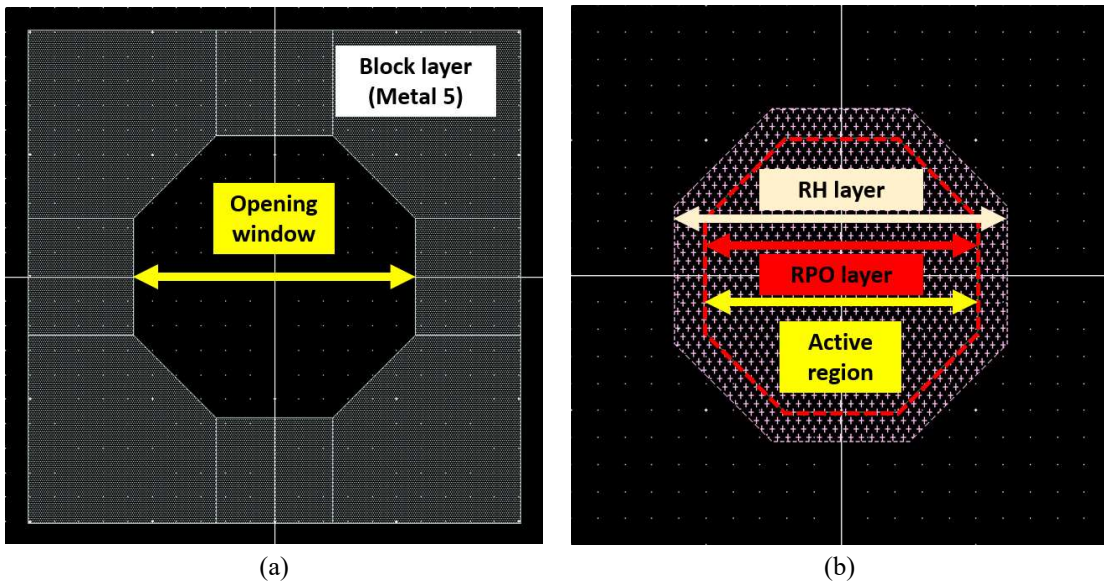


Figure 4-2. Special layers designed for SPADs: (a) Block layer M5; (b) Special layers RH and RPO.

At the layout design level, many other layers need to be added in addition to the basic regions mentioned above. These include the OD layers, dummy layers, and PO layers. After adding all the required layers for the SPADs, a complete layout and the corresponding 2-D structure of a 10- μm diameter SPAD are shown in Figure 4-3. Please note that all the size-related information is the same as the value used in the SPAD modeling, such as Figure 3-5.

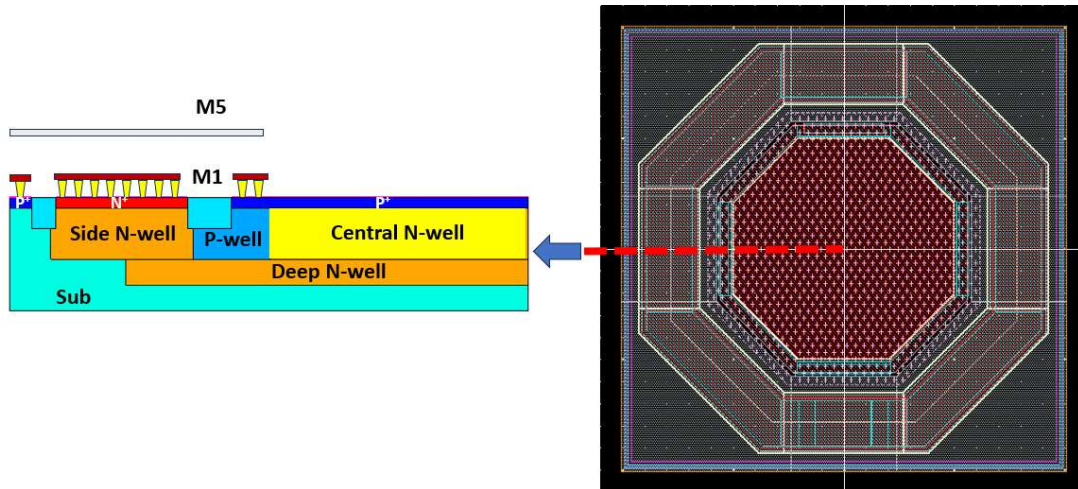


Figure 4-3. Simplified cross-sectional illustration and the complete layout of a 10- μm diameter SPAD.

4.3. Front-end Circuit Design

From the simulated I-V characteristics in Chapter 3, it is known that a large current will flow through the SPADs once they are triggered. Such a large current may destroy the device without appropriate mitigation. Therefore, SPADs must be connected to suitable quenching and reset circuits to achieve consecutive photon detections. In general, there are two major categories of quenching and reset circuits: passive quenching and reset (PQR) circuits and active quenching and reset (AQR) circuits. In recent development of SPAD's front-end circuits, AQR circuits have gained popularity for quenching and resetting SPADs. This is due to their fast quenching, configurable hold-off time, time gating capability, and high integration [170]. However, there are still some disadvantages associated with AQR circuits. For example, the MOSFETs connected to the SPADs must be carefully tuned to minimize process, voltage, and temperature (PVT) variations. Second, monostable circuits may be required for measurements if the dead time of an AQR SPAD is too short to be detected by oscilloscopes. Such monostable circuits typically include a capacitor for storing and release of carriers. However, there could be significant differences between the simulation and measurements because of the variations caused by the PVT variations. Considering both the stability and the parasitic effects, a PQR circuit was designed to quench the SPADs.

A PQR-configured SPAD circuit is simply connecting a series resistor to the designed SPAD. Two common configurations of PQR SPADs which both have positive output signals are shown in Figure 4-4 (a) and (b).

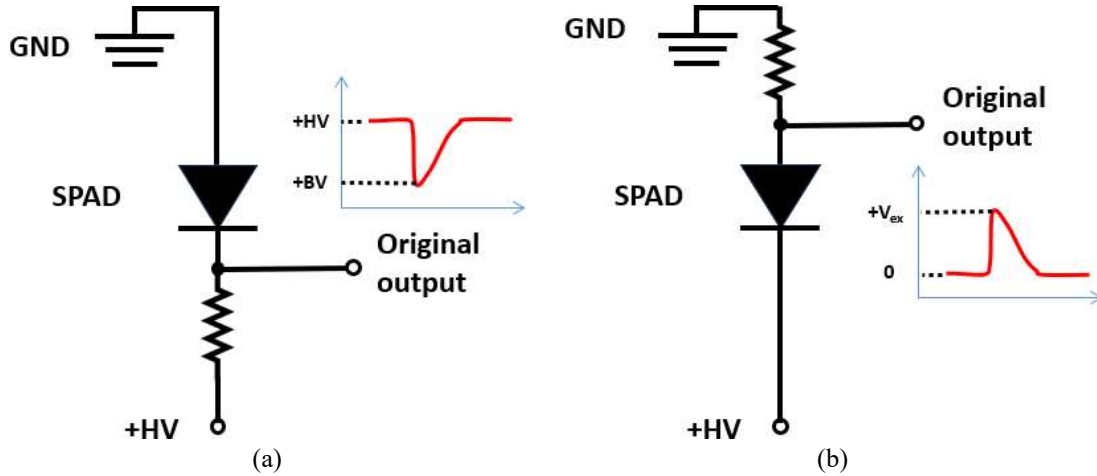


Figure 4-4. Two PQR circuits that have positive original output pulses: (a) Output at cathode; (b) Output at anode.

With the outputs taken from the opposite nodes, the pulse shapes and the absolute voltages are different. Considering the voltage specifications of TSMC 65 nm standard CMOS technology, the second configuration was selected because the voltages of the output pulses can be confined between 0 V and 1 V, which is a safe range for the input of MOSFETs. Therefore, polysilicon resistors were designed to quench and reset the SPADs. In general, the resistor designed in the PQR circuit should exceed 50 k Ω to effectively sustain an avalanche [171]. However, a very large resistance can increase the RC time constant, leading to longer reset times. In this scenario, certain simulations are necessary before assigning specific values for the quenching resistor.

4.3.1. Front-end Circuit Simulation

Circuit simulations are necessary before finalizing specific circuits. However, there is no available SPAD model in a circuit simulation. Therefore, a SPICE model is needed to describe the behaviors of a SPAD in a circuit. Such a model can be achieved by combining some ideal components in a schematic view or by developing Verilog-A blocks. In this section, a SPICE model of the SPAD was designed using simple resistors, capacitors, voltage-controlled switches (VCS), and ideal signal references. The implementation of VCS can simulate the triggering process of SPAD once “photon” signals are added as stimuli [172]. A concise schematic of the SPICE model is shown

in Figure 4-5, which includes three switches, four resistors, one capacitor, and an ideal voltage source.

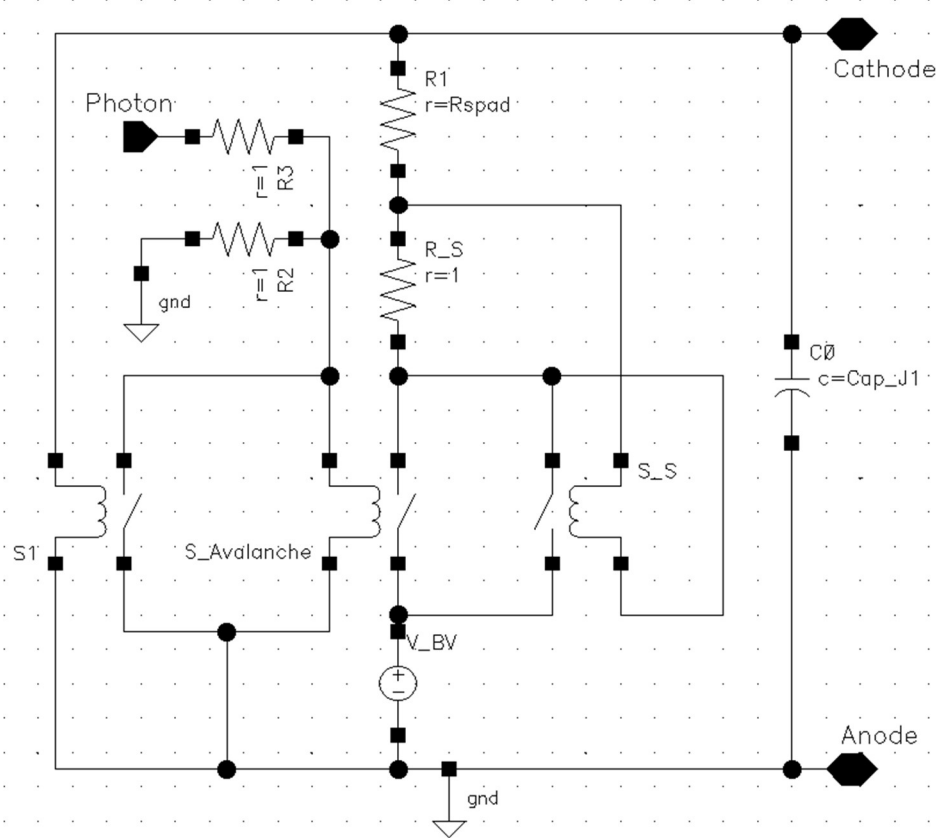


Figure 4-5. Schematic of SPAD SPICE model

From the left to the right in Figure 4-5, the switch S1 is designed to determine if a SPAD is operating above the BV. Pin ‘Photon’ is used as the input stimulus port. R2 and R3 are two small sensing resistors to prevent infinite current. S_Avalanche is a switch that controls the triggering of avalanche. The BV of the SPICE model is set by using an ideal voltage source V_BV. The switch S_S controls the self-sustaining process with a certain threshold of current flowing through resistor R_S. R1 and C0 are the SPAD resistance and the junction capacitance between the anode and cathode, respectively. A flowchart that explains how the SPICE model works to mimic SPAD’s operating mechanism is shown in Figure 4-6.

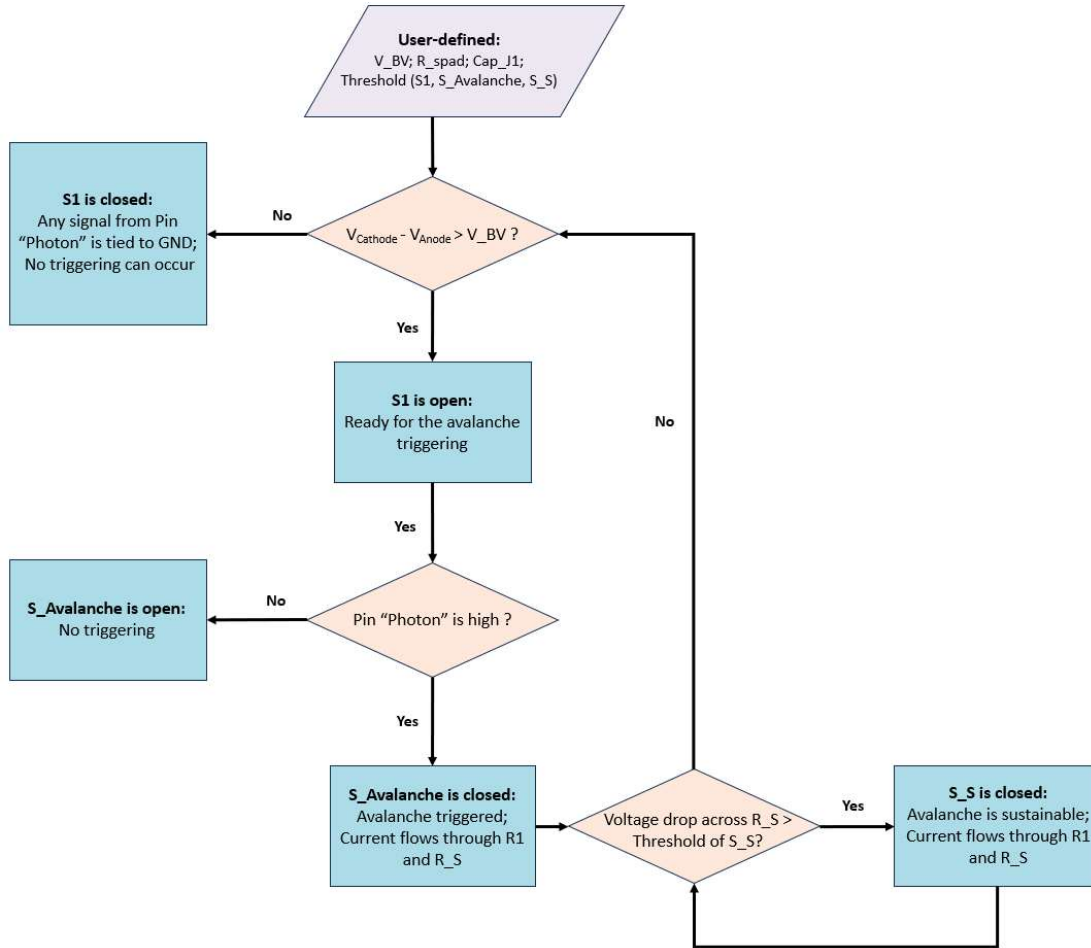


Figure 4-6. Operating principles of the designed SPICE schematic

In this SPICE model, if the applied reverse voltage across the junction is greater than the BV, the response to the incident photons can be simulated. The accuracy of the SPICE model mainly depends on the value of R_{spad} and the capacitance set, which can be estimated by fitting the avalanche pulses and the I-V characteristics. In this case, initial values for the SPAD junction resistance R_{spad} , capacitance Cap_{J1} , and quenching resistor R_L can be set according to various references and previous designs. More accurate values of these parameters can be obtained by fitting them to measured results, which can be beneficial for future SPAD designs. The SPAD's internal resistance during avalanche can drop to the hundreds of Ohms, thus having a large avalanche current [173]. Furthermore, the threshold current set for the determination of self-sustained avalanche is around $100 \mu\text{A}$. Once the current is greater than $100 \mu\text{A}$, the avalanche is considered as self-sustaining [174]. In this case, initial values of

$R_{\text{spad}} = 600 \Omega$, $R_L = 50 \text{ k}\Omega$, and $\text{Cap}_{J1} = 100 \text{ fF}$ were set for the simulation of PQR-SPAD. The simulated single response to the incident photons and the I-V characteristic above the breakdown are shown in Figure 4-7.

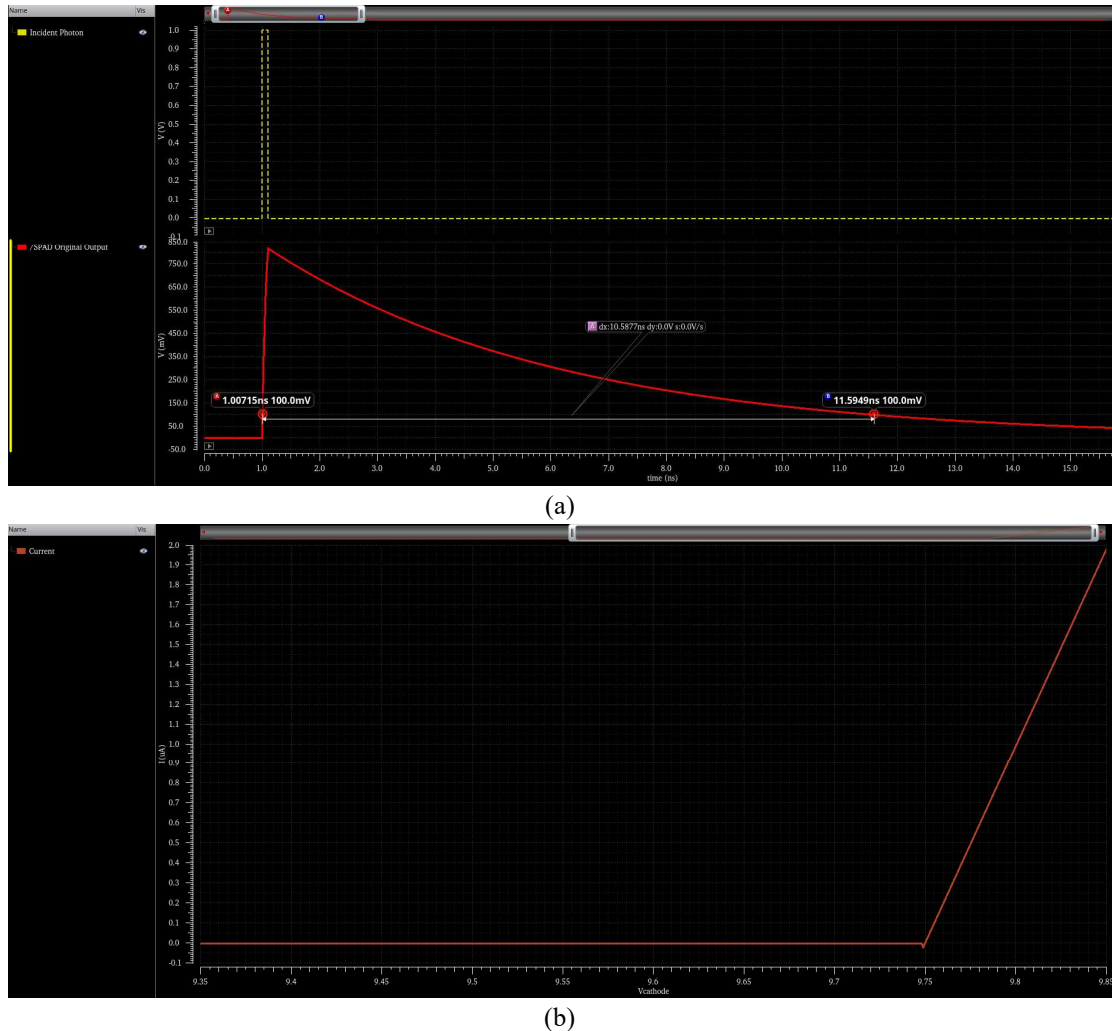
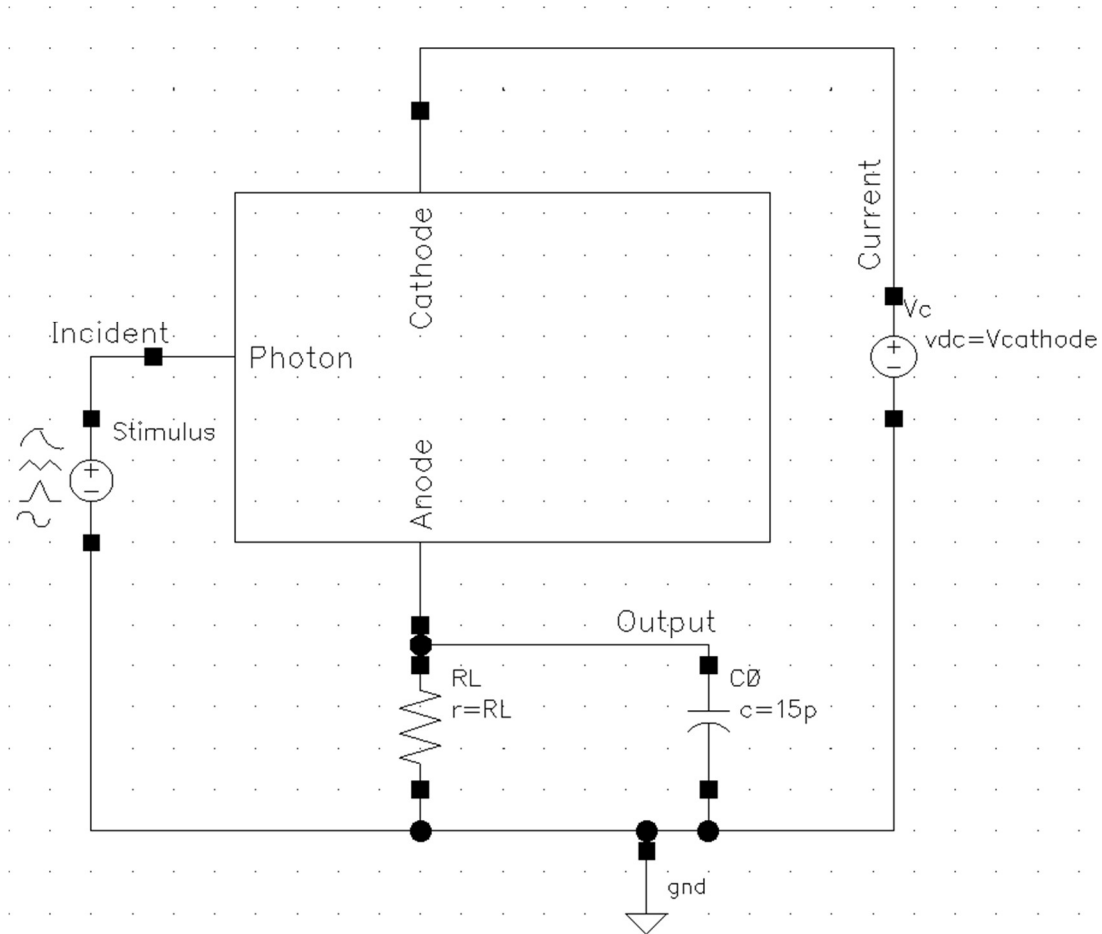


Figure 4-7. Simulated results of the SPICE model: (a) Single pulse waveform; (b) I-V curve.

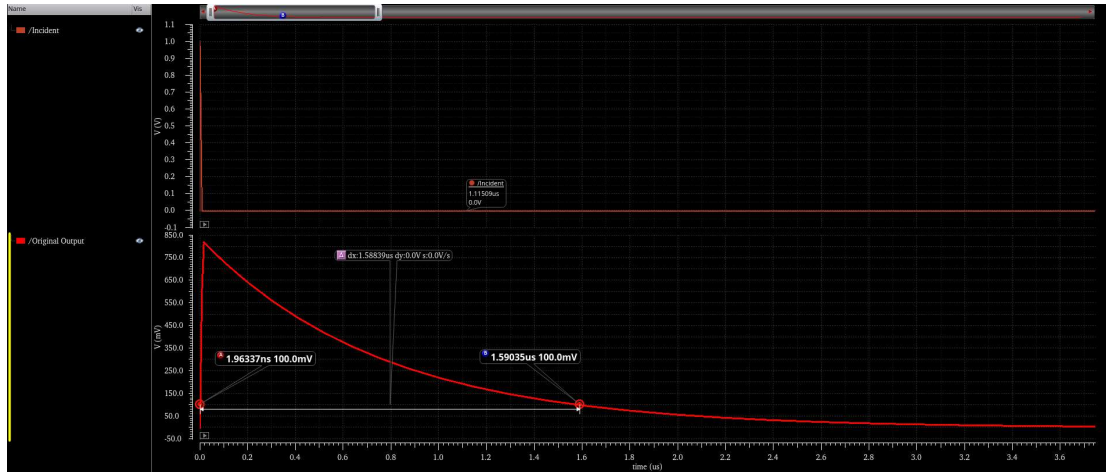
Note that the simulated results are based on the initial values, the width of the original output pulse was obtained when the load capacitance was set to zero. In the actual measurements of the SPADs, the load capacitance's effect on the RC constants should be taken into consideration. The $50 \text{ k}\Omega$ load resistor can achieve a pretty good reset time in the simulation level. Therefore, a $\sim 50 \text{ k}\Omega$ polysilicon resistor is designed in the layout.

4.3.2. Output Buffers

As discussed in Section 4.3.1, the narrow width of the SPAD's original output is due to the ideal output pin. If the load capacitance is not taken into account, the designed SPADs may not have enough driving ability to drive probes of the oscilloscope. To address this, a 15-pF capacitor was attached to the output pin in the schematic. Figure 4-8 presents both the schematic and the simulated output pulse.



(a)



(b)

Figure 4-8. Simulated results of the SPICE model: (a) SPICE schematic; (b) Single pulse with 15-pF load capacitor.

Compared to the simulated single pulse in Figure 4-7, the width has increased by almost a thousand times. Therefore, output buffers are needed to enhance the driving capability while ensuring that there are no distortion.

In the standard library provided by TSMC, several standard inverters can be utilized for designing an output buffer. However, the standard cell with the strongest driving ability can only handle capacitances smaller than 1.58 pF. Therefore, a parallel design is necessary to achieve a much stronger driving ability. By designing a 4-stage paralleled output buffer, the driving ability progressively increases, until it can drive the 15-pF load capacitor at the output node. The simulated output waveforms are shown in Figure 4-9, which indicates almost no additional delay caused by the load resistance. The pulse width of the output from the output buffer falls within nanoseconds range, which is even smaller than the original output pulse's width. This is because that the threshold voltage of the designed output buffer is 0.5 V.

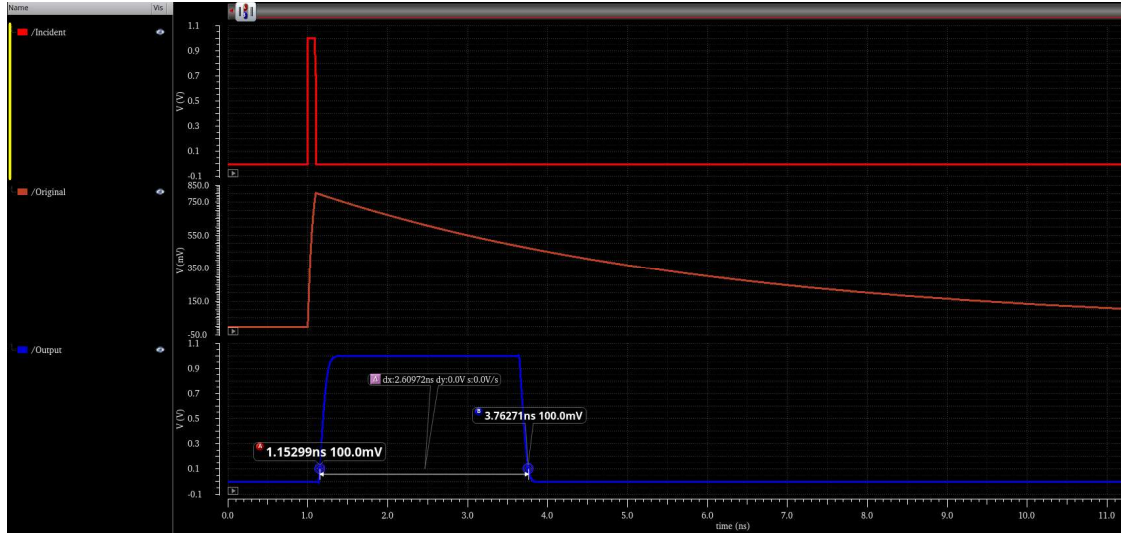


Figure 4-9. Simulated waveforms of incident photon, original output, and output of the output buffer (From top to the bottom)

4.3.3. Whole-chip Layout Design

Based on the simulations conducted on the SPICE model, PQR circuits, and output buffers, the complete layout of the circuit is presented in Figure 4-10. 5 SPADs were designed with passive polysilicon resistors of 51.39 k Ω and corresponding output buffers. To avoid crosstalk that could happen when two SPADs are very close to each other, each SPAD was placed at a distance of $> 20 \mu\text{m}$ from the others. In addition, due to the limited number of pins in the fabrication, the SPADs shared a single ground pin, which may introduce additional parasitic effect. Dummy layers of metals are necessary to satisfy certain density requirements. Inside the core circuit region, additional metals were added to meet the least density requirement of each layer. For the designed SPAD circuit, only 11 pins are needed for biasing and signal readout.

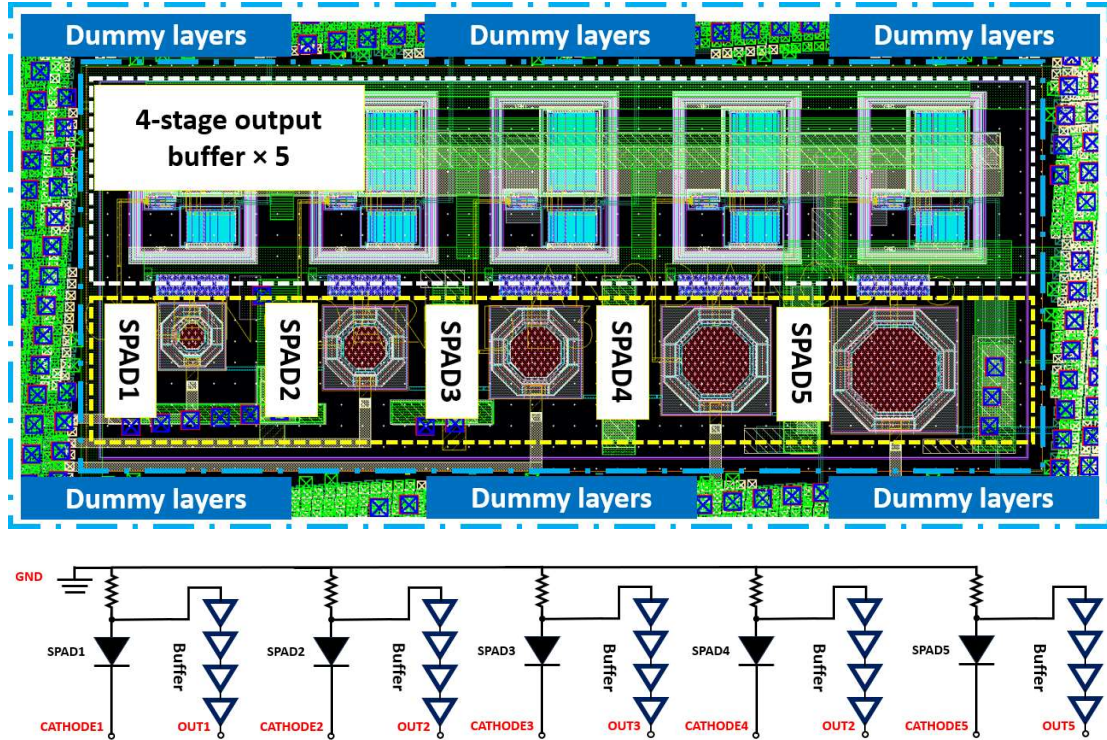


Figure 4-10. Complete layouts of 5 SPADs, 5 output buffers, and dummy layers (Top); Connections and pins (Bottom).

4.4. Measured Results and Discussions

Based on the discussions on the SPAD's design and simulations, the SPADs and front-end circuits were fabricated based on 65 nm standard CMOS technology. In this section, measurements on the fabricated SPADs were conducted to obtain the results: I-V characteristics after BV. The measured results were compared to the previous simulations. Based on the comparison, a fitting process was explored to optimize the SPICE model of SPADs, which are beneficial for future SPAD design. Additional discussions were presented at the end.

4.4.1. Measurement Setup

The fabricated chip was based on a 68-pin PGA technology. Indeed, a PCB was needed to apply the bias and measure the output for each SPAD. The PCB was designed concisely. There is no attenuator needed for converting voltages. A complete measurement setup for measuring the I-V characteristics and the single output pulse of a SPAD is shown in Figure 4-11.

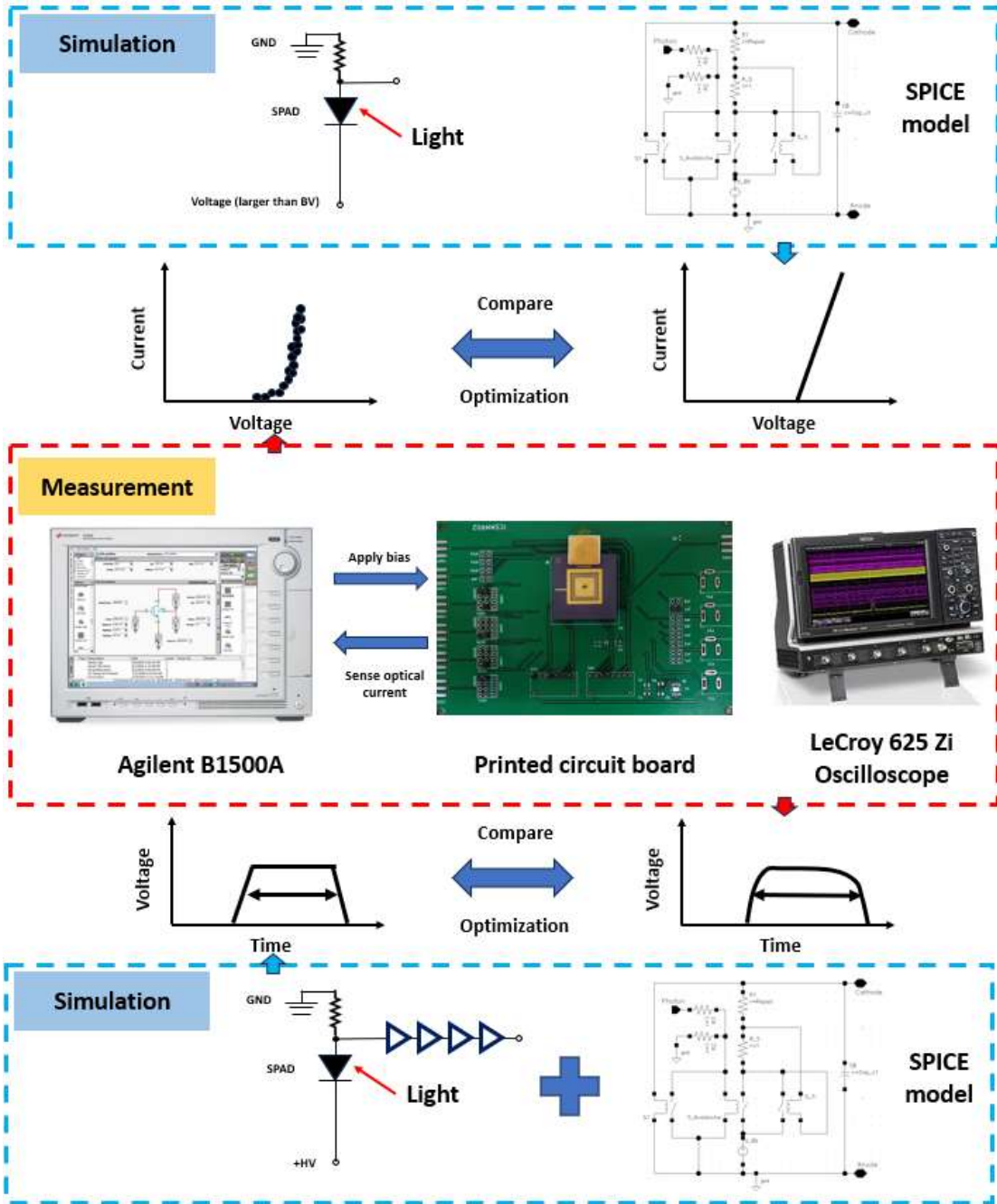


Figure 4-11. Measurement setup and expected results for SPAD’ single output pulse and I-V characteristics under illumination.

4.4.2. Results and Discussions

During the illumination, the I-V characteristics of the fabricated was measured to determine the optical current after the breakdown. The slope of the I-V curve can be extracted and compared to the simulated value obtained from SPICE model simulation.

This slope is highly related to the resistance during the avalanching process. The comparison between the simulations and the measurement of I-V characteristics is also helpful to determine if a piecewise-resistance in SPICE model is necessary for PQR-based SPAD circuits. The measured datapoint were shown in Figure. 4-12, along with linear fitting and comparison with the simulated value from the SPICE model. From Figure 4-12, the simulated avalanching current is on the order of hundreds of nanoamperes, which is consistent with the simulated value.

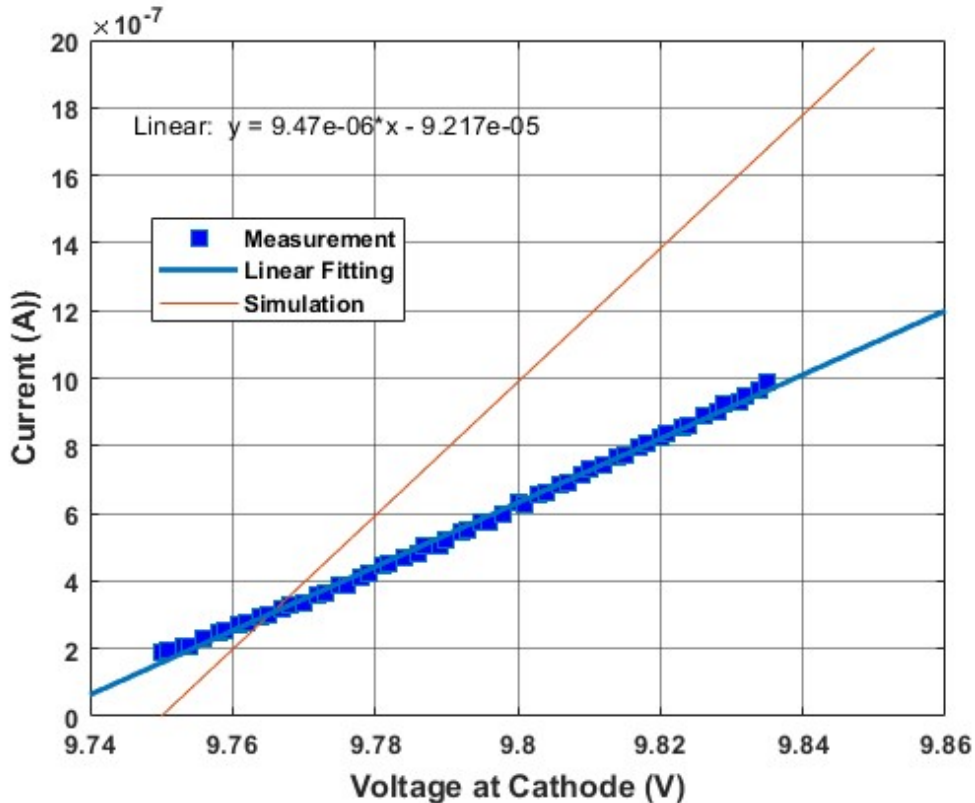


Figure 4-12. Comparison between simulation and measurements of avalanching current

Based on the measured data, a simple linear fitting was included in the plot, indicating a good linear property of the avalanching current in the current range. From the simulated results, the SPAD didn't show a very significant nonlinearity. The resistance can be extracted from the measured data, following Eq. 4-1.

$$\frac{1}{Slope} = \frac{V - V_0}{50k\Omega + R_{I-V}} \quad 4-1$$

The big slope difference can be calibrated by fitting the R_{spad} in the SPICE model. Since a 51.39 k Ω load resistor is connected to the SPAD, the value of R_{spad} should be increased by several kilo ohms to achieve a noticeable difference. The reason for such a big difference in the resistance is because the current specified voltage range is slightly above the BV. If more data are collected at much higher voltages, the slope of the I-V curve will be steeper, thus having smaller resistance in the order of hundreds of Ohms. To validate that the fitted resistance in the current voltage range is correct, measured data from 3 SPADs with different sizes were shown in Figure 4-13.

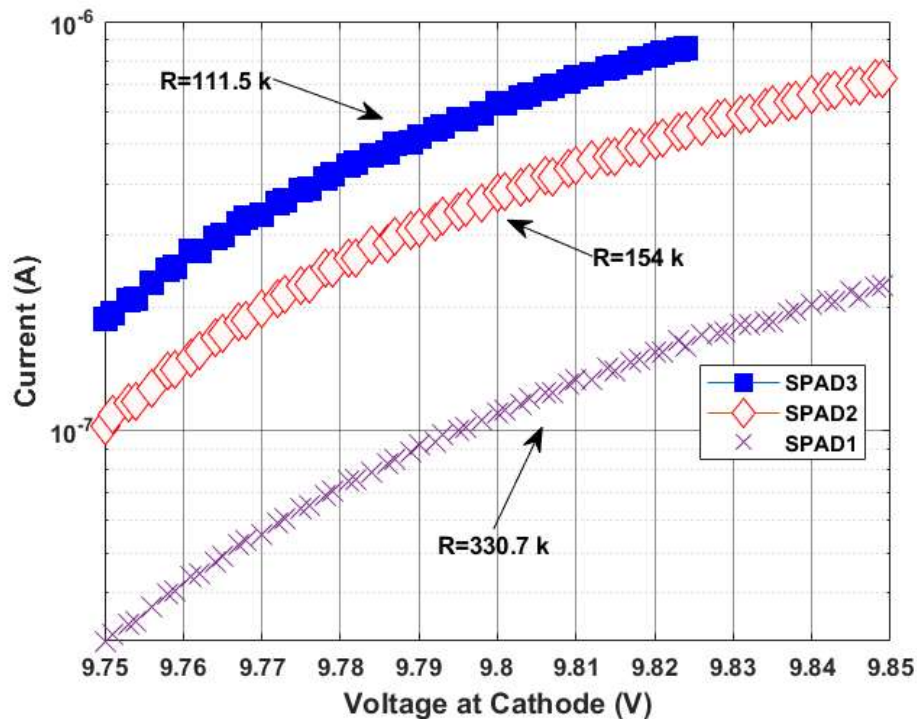


Figure 4-13. Comparison of measured I-V between 3 SPAD with different sizes of active region

From Figure 4-13, SPAD 1 to SPAD 3 have a active region of 29.823 μm^2 , 82.843 μm^2 , and 119.294 μm^2 , respectively. The linear fitting indicates the differences of the serial I-V resistance of these SPADs (at 9.75-9.85 V). Based on the Eq. 4-1, the resistance due to the current path in diodes can be represented using a simplistic equation, which is expressed by Eq. 4-2 [172].

$$R = \rho \frac{D}{A} \quad 4-2$$

where D is the thickness of the depletion region and neutral region, A is the size of the active region. For the three different SPADs, the doping concentration and the biasing voltages are exactly the same, therefore, the term D can be regarded as the same for them. And ρ is a constant value for the silicon material. In this case, the resistance is inversely proportional to the size of the active region. Based on the extracted resistance from Figure 4-14, the ratio between resistance can then be compared with the ratio of the active region's size, as expressed in Eq. 4-3.

$$\frac{R_1}{R_2} = \frac{278.9}{102.2} = 2.72896, \quad \frac{S_2}{S_1} = \frac{82.843}{29.823} = 2.7778 \quad 4-3$$

$$\frac{R_2}{R_3} = \frac{102.2}{59.7} = 1.71119, \quad \frac{S_3}{S_2} = \frac{119.294}{82.843} = 1.44$$

From Eq. 4-3, it is clear that the extracted resistance from the measurements has met the expectation from the theories. Therefore, at each voltages, such a relation should be consistent. Considering a very large resistance in the voltage range between 9.75 V to 9.85 V, piecewise-resistance components are of great necessity in the complete SPICE models for SPADs. With varying resistance, SPICE model can describe SPAD's performance in a circuit more accurate, and in a wide voltage range.

With different RC constants, the shape of the simulated SPAD's outputs also varies significantly due to the varying charging and discharging abilities. The shape, width, and the amplitude of the output pulse are also different with different RC constant.. Therefore, to improve the SPICE model, measurements of the shape, width, and amplitude of the output pulses are of importance. However, there are some challenges regarding these characterizations. First, the output pulses are also affected by the connected output buffers. These output buffers also exhibit unexpected variations regarding the charging and discharging abilities. Second, the complicated parasitic effects of the device, PCB board, cables, and the measurement devices can have significant influence on the abovementioned parameters. Lastly, SPICE models are based on describing the behavior of SPADs in circuits, which is not derived from rigorous physical process. Therefore, further investigations are necessary to mitigate such effects for improved SPICE models.

4.5. Conclusion

In this chapter, key design considerations and design process of the PQR SPAD were discussed. The SPICE model was developed to mimic the SPAD's performance in a PQR front-end circuit. To address the problem of driving large capacitive loads, a 4-stage output buffer was simulated and implemented. The designed layout was fabricated in the 65 nm standard CMOS technology by TSMC.

Measured results of the current-voltage (I-V) characteristics of SPADs using PCB and semiconductor analyzer are referenced to calibrate and optimize the original SPICE model. The calibration of the SPICE model is based on both the I-V characteristics and the shape of the output pulses. The simulated results of the optimized SPICE model achieved higher accuracy compared to the previous simulations. In the future design of PQR SPAD, this SPICE model can serve as a good reference in estimating a SPAD's performance in a real circuit. However, there are still some challenges to be overcome. First, the measurement is conducted by simply ignoring the output buffer connected at the anode. Although the output buffer is not biased, unknown parasitic capacitance and resistance may exist, which can affect the measured results. Second, the process, voltage, and temperature variations (PVT) have been considered in the current SPICE model. Third, the simulated SPICE model can only simulate the SPAD's behavior, which is only above the breakdown voltage. Additional sections like the APD's I-V characteristics below the breakdown voltage can be added for calibration. Last, the influence caused by parasitic effects from circuits, components, experimental devices should be mitigated.

Chapter 5

DESIGN AND MEASUREMENTS OF CMOS

SPADS AND CIRCUITS

This chapter presents the measured results of the fabricated SPAD and PCB, along with detailed discussions on the layout, measurement setup, breakdown voltage (BV), dark count rate (DCR), photon detection probability (PDP), SPAD's edge effect, and influence of measurement settings.

5.1. PCB and Measurement Setup

The measurements of BV and DCR are based on the previous measurement setup in Chapter 4. The difference is that a completely dark environment is required during the testing. So, the SPAD should be measured in a dark room. To measure the DCR of the SPADs, two voltage sources are needed to power the PCB, output buffers, and the SPADs. A complete setup of measuring DCR is shown in Figure 5-1.

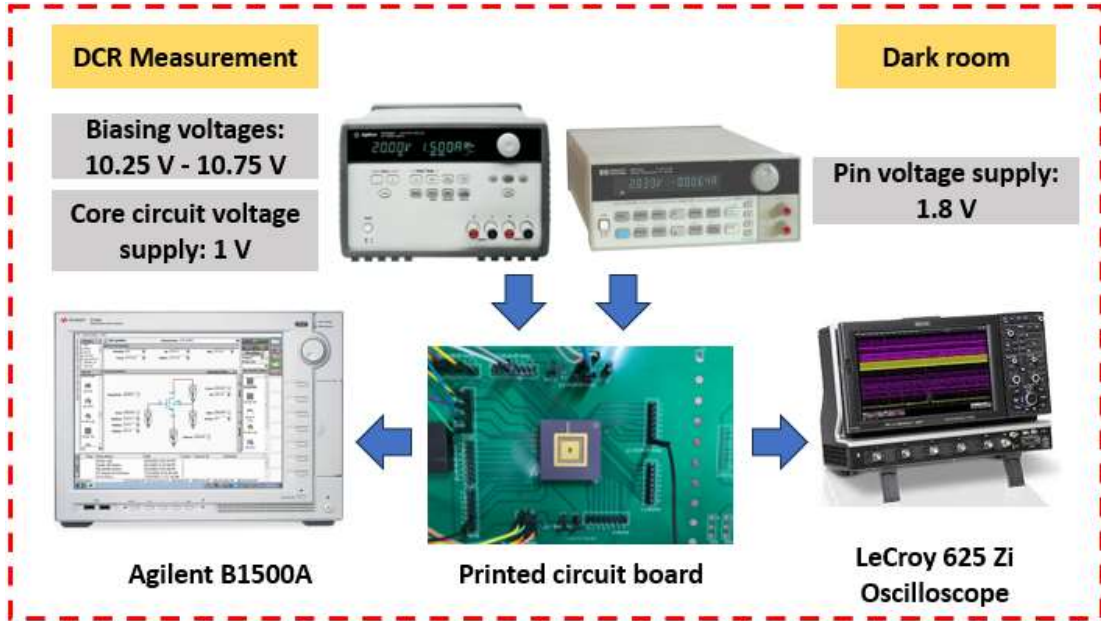


Figure 5-1. Breakdown voltage (BV) and dark count rate (DCR) measurement setup.

Note that the two voltage sources are of different accuracy. Agilent E3346A, which has two channels, was used to supply the core circuits and the bias the SPADs. And the voltage source Agilent 66312A was used to power the pins of the chip, which requires a constant 1.8 V voltage supply. For the core circuits that consist of MOSFETs, a 1 V voltage supply was applied. Note that all the measurements were conducted based on multiple chip replicas and multiple measurements to ensure consistency.

5.2. Measurements of SPADs and Discussion

The measurements of the PQR SPADs in this chapter are used to compare and calibrate the proposed SPAD model. In this Chapter, the measurement was conducted based on a newly designed PCB board. The measurement was conducted in the dark room to have the least influence from environmental interferences. The measured results were compared to the calibrated SPAD model, followed by the analysis of the model's effectiveness and deviations.

5.2.1. Breakdown Voltage (BV)

In Chapter 3, the breakdown voltage of the SPAD structure was simulated based on the initial value of doping concentrations. To have more accurate SPAD models, the calibration of the doping concentrations must be done prior to the prediction of SPAD's

DCR and PDP. In this case, the fabricated SPADs were measured using the semiconductor analyzer shown in Figure 5-2. The simulation of the I-V characteristics was done by sweeping the voltage applied to the cathode of each SPAD, once a sudden increase of the current is witnessed, the voltage can be regarded as the BV of the SPAD. The simulated I-V curve is shown in Figure. 5-2, which indicates a BV of ~ 9.75 V. Note that multiple measurements were repeated to reduce the variations.

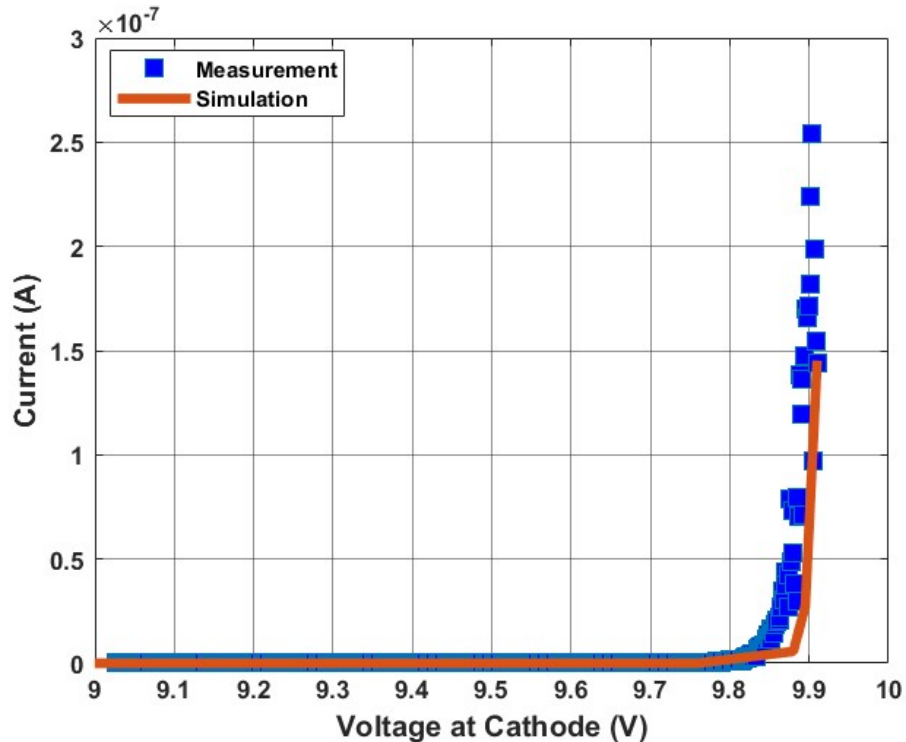


Figure 5-2. Comparison between the simulation and measurement of breakdown voltage

Referring to Figure 5-2, the voltage range applied to the SPADs was from 9 V to 10 V, and the simulation started from zero bias. However, one thing to be noted in the simulation of BV using TCAD is the convergence problem. In addition to the proper mesh settings needed, the avalanche process should be suspended timely after the avalanche to get convergent results [175]. After the iterative calibrations taken on the doping concentration of the N-well and P+ region, the simulated BV was very consistent with the measured value. Due to the slight change of the doping concentration, the DCR caused by band-to-band tunneling mechanism may have a lower value. Parameters of simulation were listed in Table 5-1. The characterization of the SPAD's DCR will be presented in Section 5.2.2.

Table 5-1. Basic Parameters used in the Simulation of BV

P+_doping	$1 \times 10^{18} \text{ cm}^{-3}$
N-well_doping	$2.21 \times 10^{17} \text{ cm}^{-3}$
Voltage range (at cathode)	1-15 V
Temperature	300 K
Impact ionization model	Okuto-Crowell
SRH generation	Default
BTBT generation	Schenk model
Bandgap model	Oldslotboom with band gap narrowing
Electron saturation velocity	$1.07 \times 10^7 \text{ cm/s}$ [161]
Electron saturation velocity	$8.37 \times 10^6 \text{ cm/s}$ [161]
Breakdown Analysis	Current limit = 0.15 μA
Avalanche derivatives	Enabled
Max iterations	20

5.2.2. Dark Count Rate (DCR)

From the discussion of the SPAD fundamentals, the DCR has a strong dependence on the biasing voltage at the room temperature. To measure the DCR of fabricated chip, a similar measurement setup as measuring BV was used. However, a high-speed oscilloscope, instead of the semiconductor analyzer, was used to count the effective output pulses, as shown in Figure 5-1. Since the dark counts happen randomly in the time domain, a Poisson distribution of the output pulses caused by dark noise should be witnessed. However, a certain number of counts should be recorded to make sure of a smooth Poisson distribution. In the measurement, the total counts needed for obtaining DCR range from between 1×10^5 to 5×10^5 cps.

However, in addition to the counts caused by the dark noise, another mechanism known as afterpulsing can cause additional counts. When an avalanche is triggered due to the carriers generated from dark noise or photon absorption, the traps may capture a certain number of carriers during the avalanche process. However, the captured carriers may be released after a certain time due to the finite lifetimes of the traps. During the release of these trapped carriers, if the SPAD is still biased above the BV, there is a

certain probability of triggering another avalanche. However, the afterpulsing is a time-correlated phenomenon, which is totally different from the random generation of dark carriers. Therefore, it is possible to distinguish between the counts that are caused by dark carriers and the counts that are caused by afterpulsing. The afterpulsing in SPAD is commonly characterized by afterpulsing probability (AP). In the measurement of DCR, AP can be calculated by analyzing the inter-arrival-time (IAT) plot.

IAT is the time duration between two consecutive output pulses that are measured. Due to the random generation process of dark carriers, the IAT should also have a Poisson distribution, as shown in Figure 5-3.

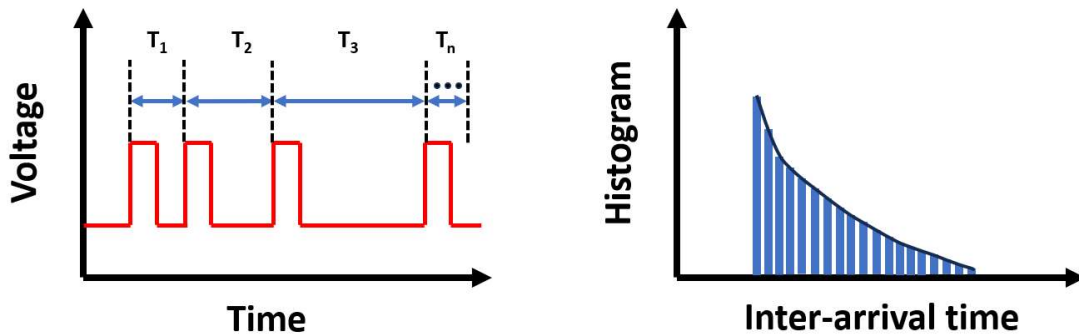


Figure 5-3. Definition of inter-arrival-time and ideal distribution

When the AP is high, additional counts may present, thus causing a deviation in the IAT plot, with a certain exponentially decaying trend. Therefore, if the AP is small that is negligible, a single exponential fit can fit the IAT plot well. However, if the AP is high, multi-exponential fitting is required. The primary DCR of SPAD follows the Poisson distribution as expressed by [176]:

$$f(\tau) = \lambda_p \exp(-\lambda_p \tau) \quad 5-1$$

where λ_p is the factor of the primary dark counts.

The histogram of IAT can be further processed to determine the primary DCR and DCR caused by afterpulsing. By taking a logarithm operation on Eq. 5-1, the exponential relation can thus be converted to a linear relation, which is given by

$$\ln(f(\tau)) = \ln \lambda_p - \lambda_p \tau \quad 5-2$$

Based on Eq. 5-1 and Eq. 5-2, the mean value and the variance of the IAT distribution can be expressed as [177]:

$$\tau_{mean} = \int_0^{\infty} \tau f(\tau) d\tau = \frac{1}{\lambda} \quad 5-3$$

$$\tau_{sdv}^2 = \int_0^{\infty} \tau^2 f(\tau) d\tau - \tau_{mean}^2 = \frac{1}{\lambda^2} \quad 5-4$$

From the mean value and the standard deviation of the IAT distribution, a ratio can be derived to help determine if AP is large or negligible. By taking the ratio of τ_{mean} and τ_{sdv} , an ideal IAT distribution free of afterpulsing will give a value of 1.

The measured IAT plot of a 10- μ m-diameter SPAD biased at a 0.7 V excess voltage is shown in Figure 5-4. According to the result from a single exponential fitting, the ratio of τ_{mean} divided by τ_{sdv} is 0.998, which indicates a negligible AP. The primary DCR obtained from the mean value of the IAT was 13.386 kHz.

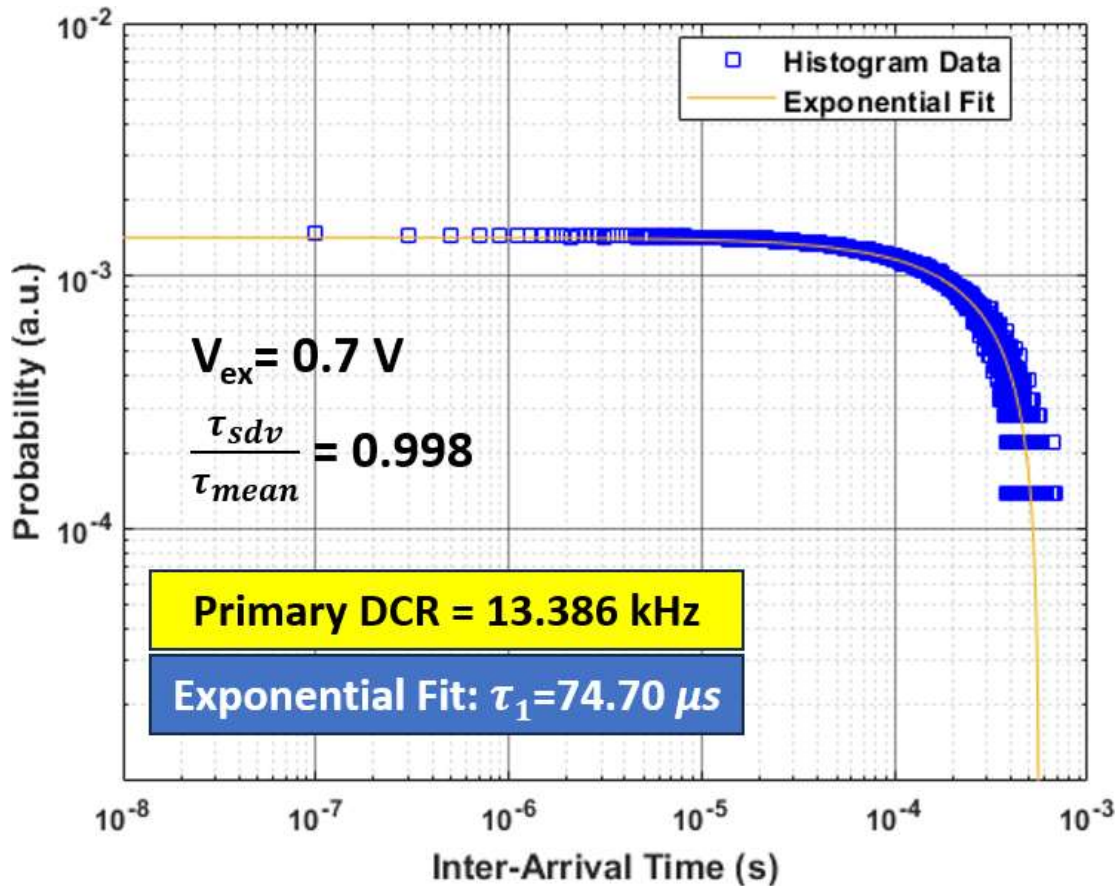
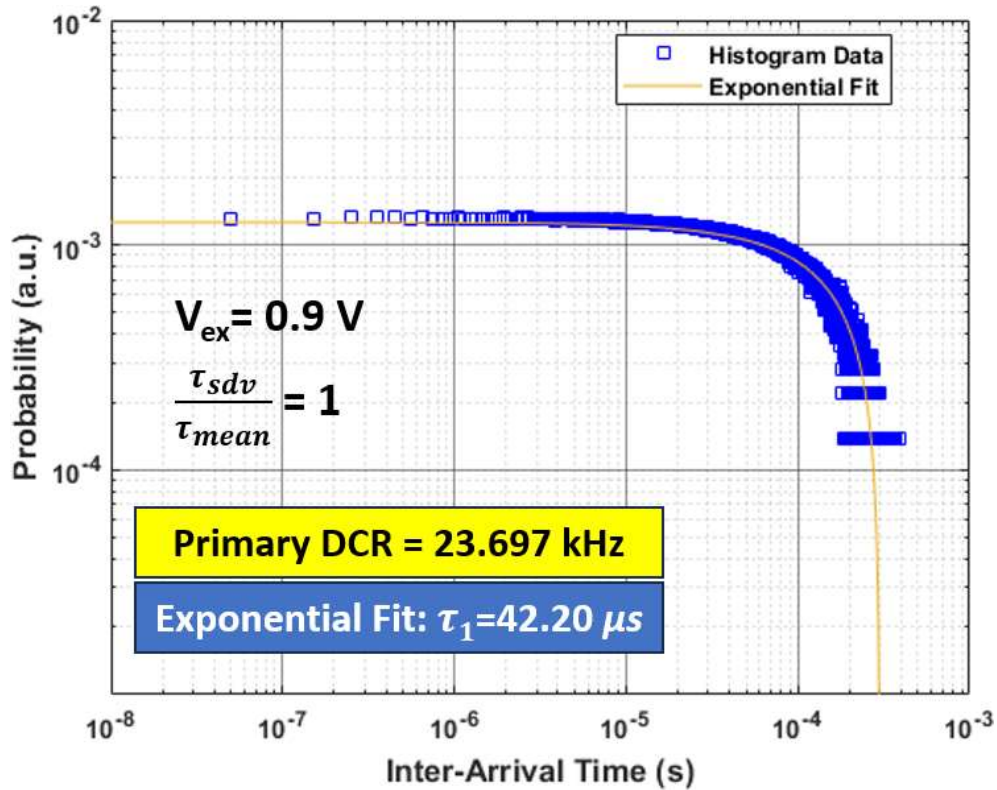


Figure 5-4. Inter-arrival-time plot of a 10- μ m-diameter SPAD at 0.7 V excess voltage

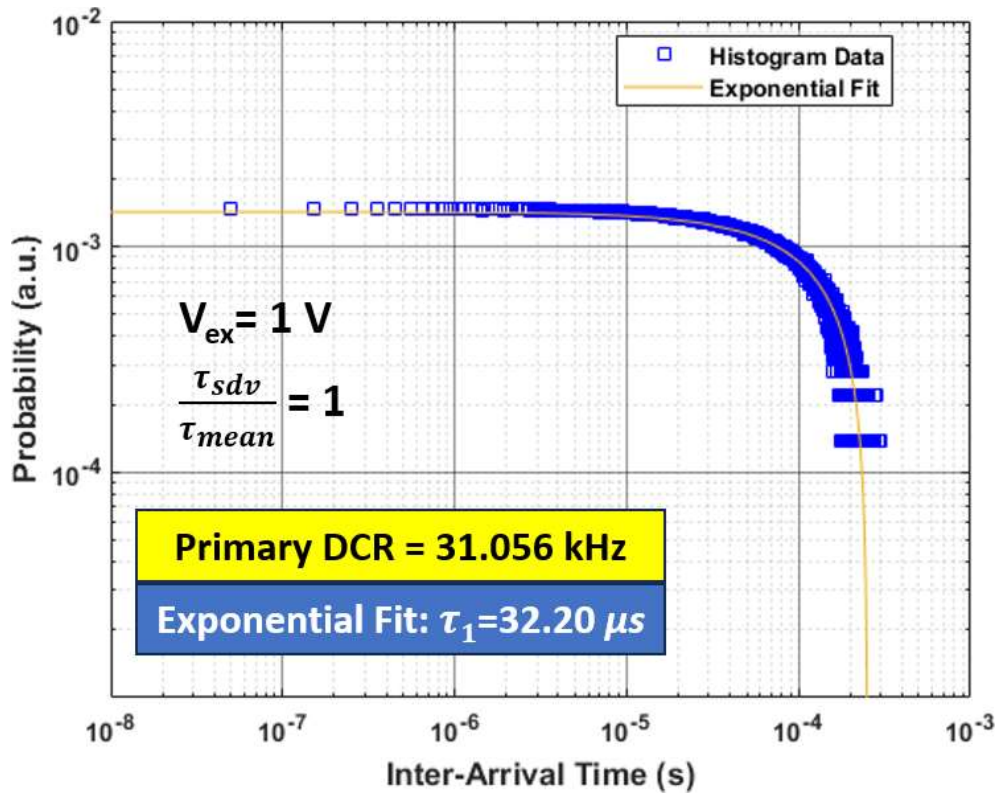
At an excess voltage of 0.7 V, the performance of the tested SPAD shows a decent DCR, compared to previous designed passive quench SPADs [178]. However, the influence of the measurement setup should be considered. In the measurement, the threshold voltage for an effective count was 0.5 V. If the threshold voltage is larger,

less pulses will be counted, causing smaller DCR. In addition, the output buffers were connected to all the passive quench SPADs in the design, which also have a 0.5 V threshold at the SPADs' anodes.

For a single SPAD, the change of the biasing voltage will have significant influence on the measured DCR. In Figure 5-5 (a) and Figure 5-5 (b), two IAT plots of a single SPAD at different excess voltages were compared. From the comparison among the IAT plots, it can be observed that higher excess voltages can cause smaller τ since more dark counts were measured by the oscilloscope and leading to smaller average time duration between two consecutive detections. A single τ can be used in the fitting since the designed SPADs were free of afterpulsing.



(a)



(b)

Figure 5-5. Inter-arrival-time plot of a 10- μm -diameter SPAD at (a) 0.9 V excess voltage; (b) 1 V excess voltage

For the tested SPAD with a 10- μm diameter, the area of the active region is 82.843 μm^2 . Therefore, the measured DCR at different biasing voltages was converted to the DCR per unit area for the purpose of comparison. In Figure 5-6, the simulated DCR of SPADs is compared to the measured DCR. Note that the DCR has been normalized to the area of the active region. The unit is $\text{cps}/\mu\text{m}^2$. To get a good agreement with the measured data, accurate information related to the trap energy level should be specified. However, such information is not accessible to designers. In this case, it is commonly considered as a fitting parameter to fit the experimental data, as it has no influence on the impact ionization coefficients and the breakdown voltage [157]. The value of the single trap energy level was adopted to be 0.19 eV in the DCR modeling as it showed a decent agreement with the measurements.

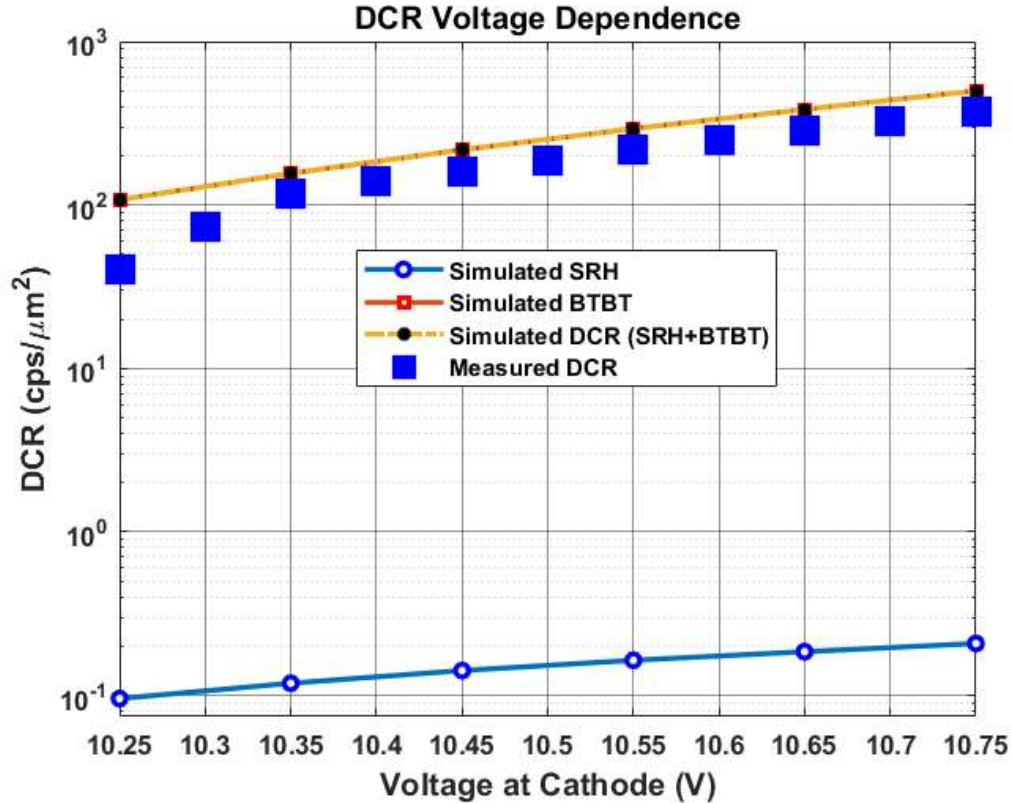


Figure 5-6. Comparison between simulated DCR and measured DCR of a 10- μm -diameter SPAD

From the comparison between the simulated DCR and the measured DCR, a consistent voltage dependence can be concluded. To be more specific, the voltage dependence between BTBT-induced DCR and total DCR has indicated a dominant contribution of BTBT mechanism. However, when the biasing voltage applied at the cathode is smaller than 10.35 V, a significant drop of DCR can be witnessed. The reason for the sudden drop of the DCR is because of the input threshold of the output buffers. When the excess voltage is close to or smaller than the threshold voltage of the output buffer, the amplitude at the anode of SPADs may be unable to trigger the output buffer, thus having significantly reduced number of, even no effective output pulses, as explained in Figure 5-7. In this case, these values cannot be counted as the normal DCR of the SPADs since most of them are filtered, being unable to be counted. Therefore, in the following comparison between simulations and measurements, DCR at those biasing voltages are removed.

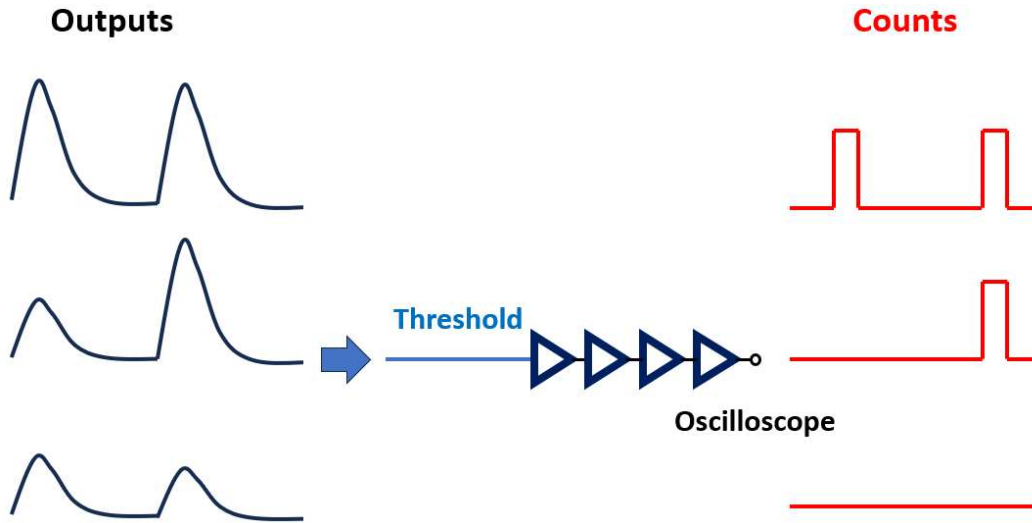


Figure 5-7. Diagram that explains the sudden drop of DCR at small biasing voltages

In Figure 5-7, the original outputs from SPADs are not directly measured using oscilloscopes but are sent to the output buffers with a certain voltage threshold. In this case, some original output pulses may be filtered out, thus causing much less DCR at small biasing voltages. In the SPAD modeling process, the counts are obtained by calculating the probability. Once an avalanche is triggered, it can be counted as a dark count. However, in real cases, the amplitude of the output pulse may vary, which can cause the lower DCR from measurements. Below certain voltages, the measured counts cannot be regarded as DCR anymore. The second reason for the difference between the modeled DCR and the measured DCR can be the edge effect. The difference due to edge effect can be further reduced by introducing a more accurate 2-D DCR model. Detailed discussions on the 2-D SPAD DCR model and measurements are presented in Section 5.3.

5.2.3. Photon Detection Probability (PDP)

Different from the simulation of PDP, only the total counts can be measured in the real cases, and counts caused by the dark noise should be subtracted. To measure the PDP of the fabricated SPADs, light source and optical filters are needed. A complete measurement setup is shown in Figure 5-8.

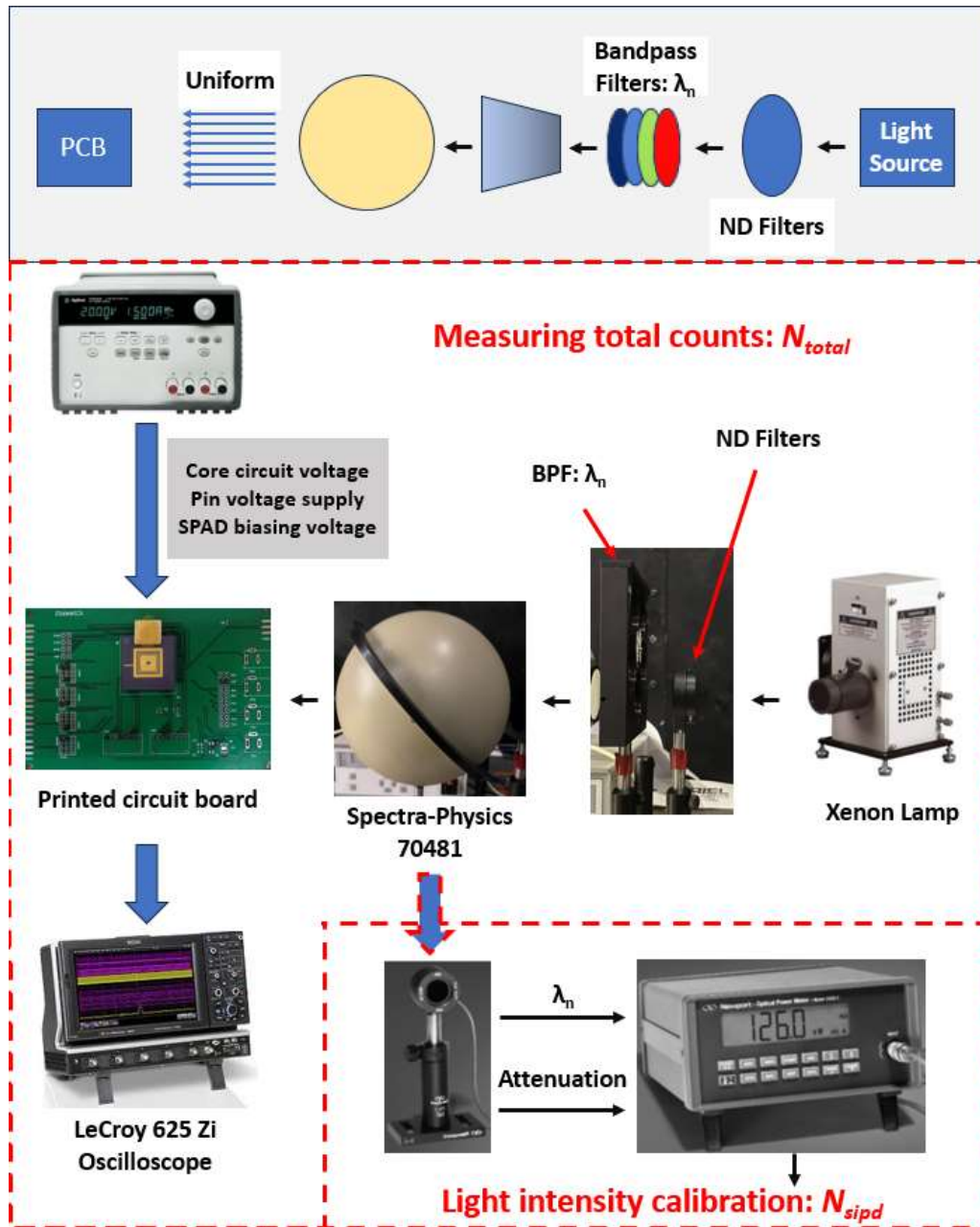


Figure 5-8. Photon-detection-probability (PDP) measurement setup

A xenon lamp was used as the light source, and the optical current can be adjusted during the measurements. If the emitted light intensity is too high, ND filters are needed to reduce the light intensity so that the photons will not saturate the tested SPADs. After the ND filters, bandpass filters are needed to select the wavelengths. The bandpass filters (BPFs) used in the measurement of PDP ranges from 400 nm to 900 nm. Since the light source is not a laser, a sphere device Spectra-Physics 70481 was used to distribute the light uniformly at the PCB board. The output signal from the PCB board

can then be measured by the high-speed oscilloscope. However, the incident photons that can arrive at the surface of the SPAD are largely reduced due to the loss during the transmission. Therefore, a calibration of the number of incident photons at the SPAD's surface is needed to obtain accurate PDP. A commercial silicon photodetection (Newport 818-SL SiPD) was combined with an optical power meter for the calibration of incident photons. The incident photon number at the surface of SPADs can be expressed as

$$\frac{N_{sipd}}{T_{unit}} = \frac{A_{spad}}{A_{sipd}} \times \frac{P_{sipd}}{hc/\lambda}, \quad 5-5$$

where N_{sipd}/T_{unit} is the calibrated incident photon number, and the unit is cps. $\frac{A_{spad}}{A_{sipd}}$ is used to correct the mismatch between the size of SiPD and the fabricated SPADs. P_{sipd} is the measured optical power at specific wavelength λ . h is the Planck's constant, and c is the light speed. After the determination of the total detected photon rate and the calibrated incident photon rate, the PDP can therefore be obtained by subtracting the DCR, following the equation:

$$PDP = \left(\frac{N_{total}}{T_{unit}} - DCR \right) / \frac{N_{sipd}}{T_{unit}} \quad 5-6$$

Based on the current measurement setup and available BPFs, PDP versus wavelength plot can be obtained at different biasing voltages. In Figure 5-9, the wavelength dependence of the PDP plot was given at an excess voltage of 0.5 V, indicating a peak PDP at wavelength of 420 nm.

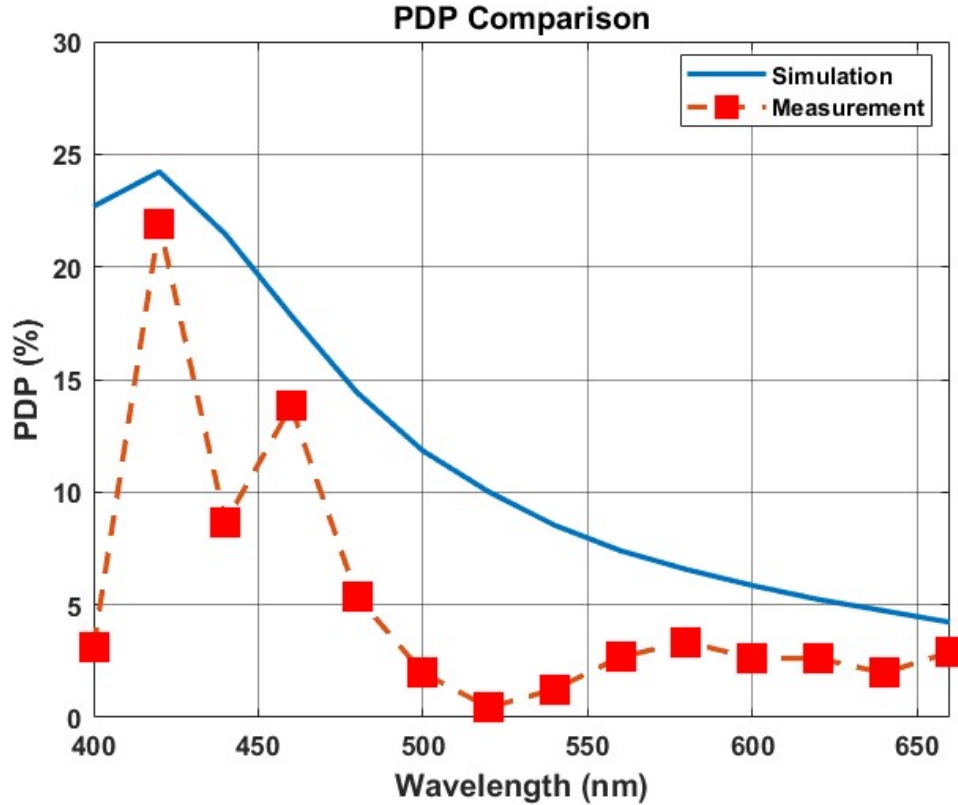


Figure 5-9. Comparison between simulated PDP and measured PDP at 0.5 V biasing voltage

At longer wavelengths, the PDP has a sudden drop due to the shallow junction in the 65 nm standard CMOS technology. More photon absorptions happen near the surface of the device. The trend of the simulated PDP and measured PDP are consistent over all wavelengths. However, in simulation, the PDP's wavelength dependence curve is smooth. There are many ripples in the curve of the measured PDP. The difference between the model and the measurement indicates the influence of light transmissions and reflections between different layers above the active region. At all wavelengths, the simulated PDP is better than the measured PDP, which is expected since there are many stacked layers above the fabricated SPADs, which can block a certain number of photons. The designed SPAD achieved a decent PDP value while maintaining a reasonable DCR level. In Figure 5-10, the SPAD's PDP wavelength dependence at different voltages is presented at different voltages, the PDP wavelength dependence has shown a similar trend, proving the curve ripples are mainly related to the optical transmissions.

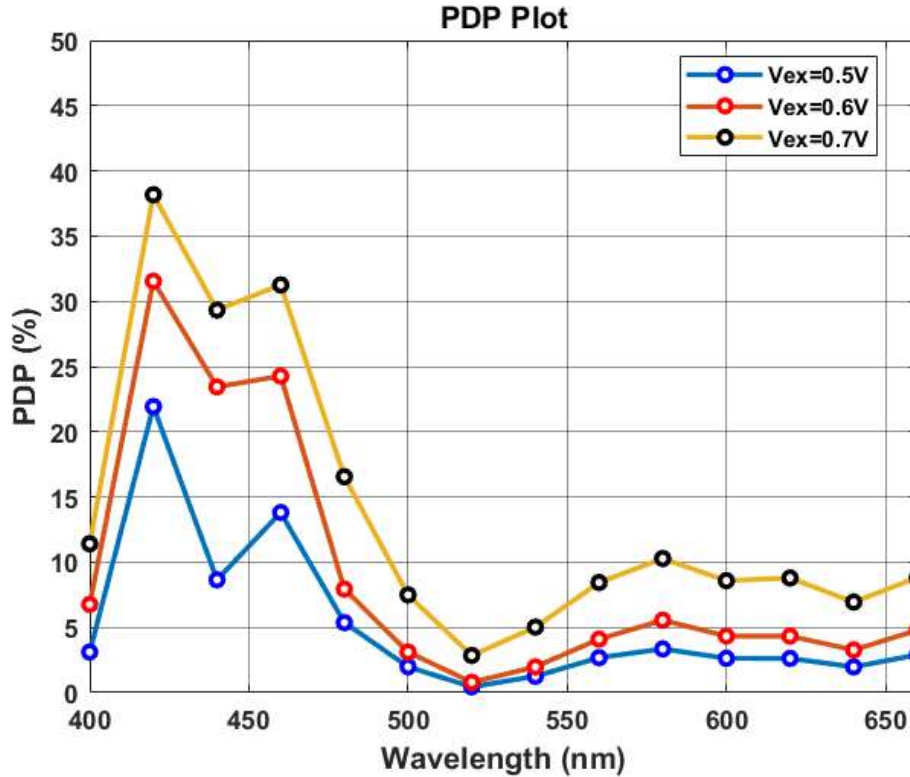


Figure 5-10. Measured PDP at three different biasing voltages: (blue) $V_{ex}=0.5V$, (red) $V_{ex}=0.6V$, orange ($0.7V$).

From Figure 5-10, when the excess voltage has increased 0.1 V, the measured PDP still remains a similar wavelength dependence. The measured peak PDP is located near the wavelength of 420 nm. At longer wavelengths, the measured PDP can also achieve a decent value, indicating the potential applications at these wavelengths, even in near-infrared regions. For example, the low-cost SPADs can then be largely used in the LiDAR systems, as discussed in Chapter 2.

5.3. SPAD's 2-D Modeling Discussion

After the comparison between the measured DCR and PDP with the simulated values, the conventional model can give a good estimation. There are still deviations between the simulation and measurements. For example, the DCR in the 1-D simulation was larger than the measured DCR. In this section, the improved 2-D SPAD model which has considered the edge effect will be compared with the simulation to validate its effectiveness.

Upon introducing the 2-D SPAD model, the total simulated DCR is obtained by averaging the DCR from all the streamlines. Therefore, it is expected that the simulated DCR will be lower than the value obtained from the 1-D model, as discussed in Chapter 3. For the SPAD with a 10- μm diameter, 25 streamlines were created in the half structure of the total active region. By taking the average of the 25 DCR values, the total DCR can thus be calculated. The comparison among the 1-D DCR, 2-D DCR, and measured DCR was presented in Figure 5-11.

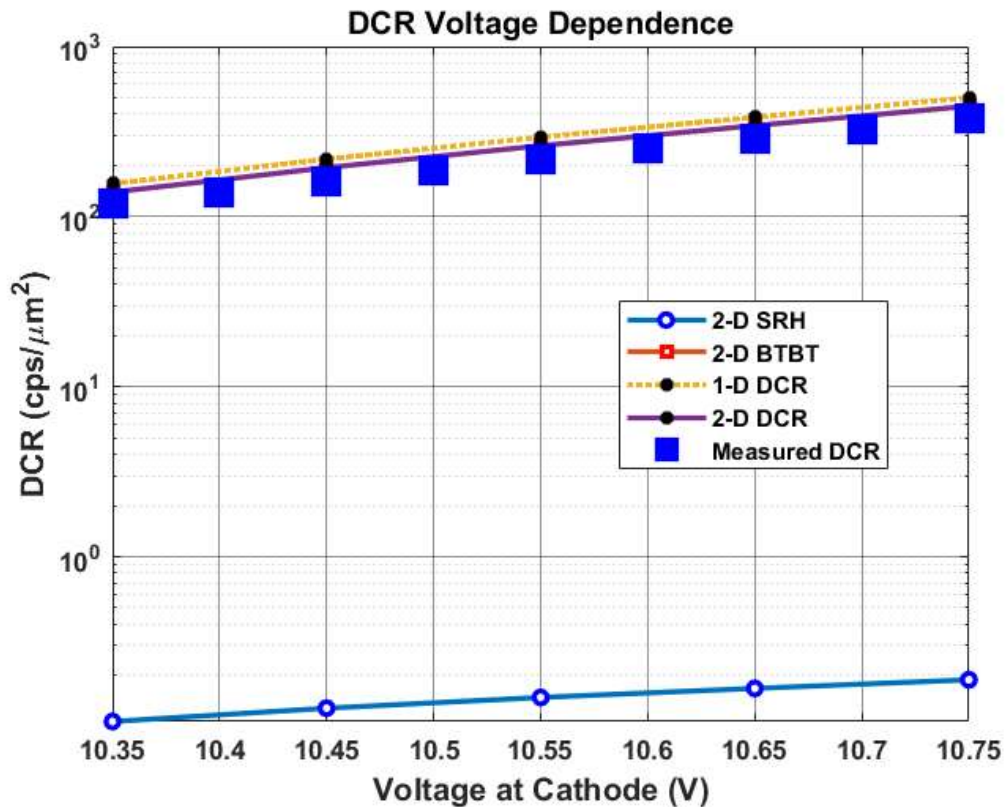


Figure 5-11. Comparison among 1-D DCR, 2-D DCR, and measured data

Note that some small excess voltages were excluded compared to Figure 5-6 since the DCR cannot be counted at these small voltages. Therefore, the comparison made at these biasing voltages might become meaningless. The simulated DCR based on the proposed 2-D model has achieved a higher accuracy, while keeping a very good voltage dependence consistency with the measured data. The major mechanism that contributes to the total DCR in the 2-D model is still the BTBT. Further improvements on the DCR modeling of SPAD may focus on the multiple trap energy level and accurate doping profile from foundries.

However, when it comes to the DCR measurement of SPADs with different sizes, the normalized DCR per unit area didn't show an expected trend at some biasing voltages, as shown in Figure 5-12. Each of the measured DCR was normalized to the DCR of the largest SPAD5.

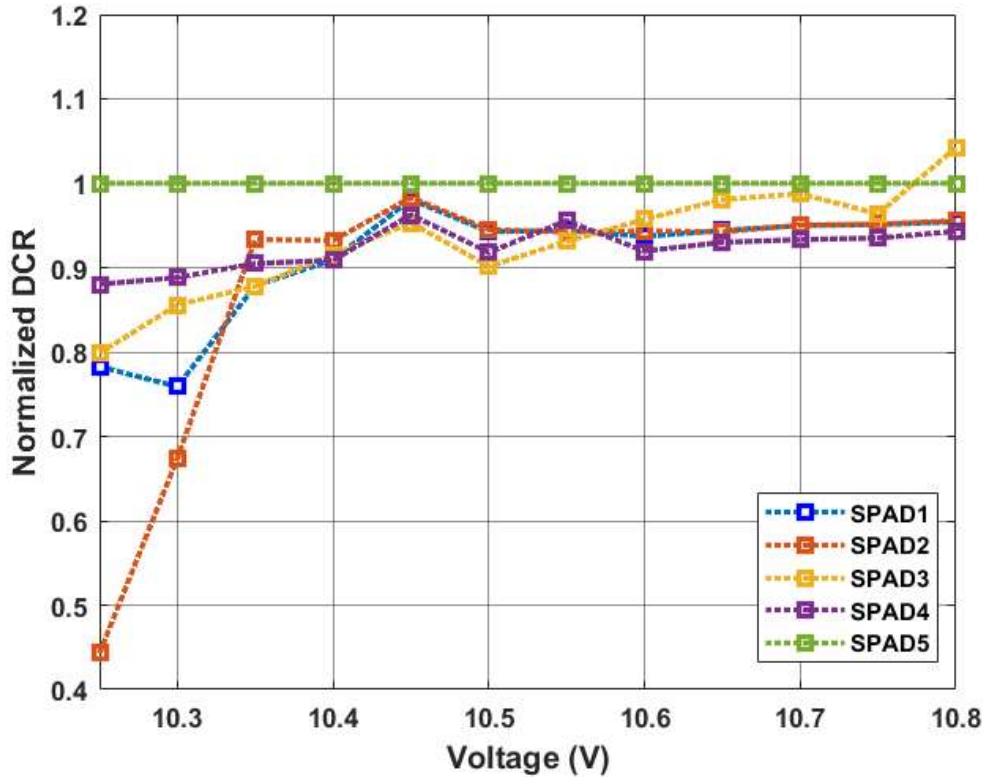


Figure 5-12. Comparison of normalized DCR of 5 SPADs based on measured data

In general, the largest SPAD has the largest DCR due to negligible edge effect, thus having normalized DCR of one. This is exactly the same as the simulated results in Figure 3-22. However, for SPAD 1 to SPAD 4, there aren't too many differences between them. From the measurement, the stability of the voltage source, slight temperature variations may have more influence on the results. However, the comparison in Figure 5-12 did prove that the decrease of the DCR due to the edge effect is limited in the range of 10 %, which is the same as the predictions based on 2-D simulations. Lastly, the sudden decrease at small biasing voltages (10.25 V and 10.3 V) is also consistent with the discussion on the influence of output buffers. For the PDP measurement on different SPADs, this phenomenon is not witnessed as additional

source of variations is introduced. For example, when the incident light intensity has increased a lot, the PDP may also increase. For SPADs with different sizes, the influence of the measurement settings can cause big differences. To figure out such variations, an additional step was taken for the validation.

For a given SPAD 2 with diameter of 10 μm , a 680-nm light was used to illuminate the SPAD. The ND filter keeps the same all the time during the measurement. However, when the incident light intensity is modified, the measured PDP can exhibit an obvious difference, as shown in Figure 5-13.

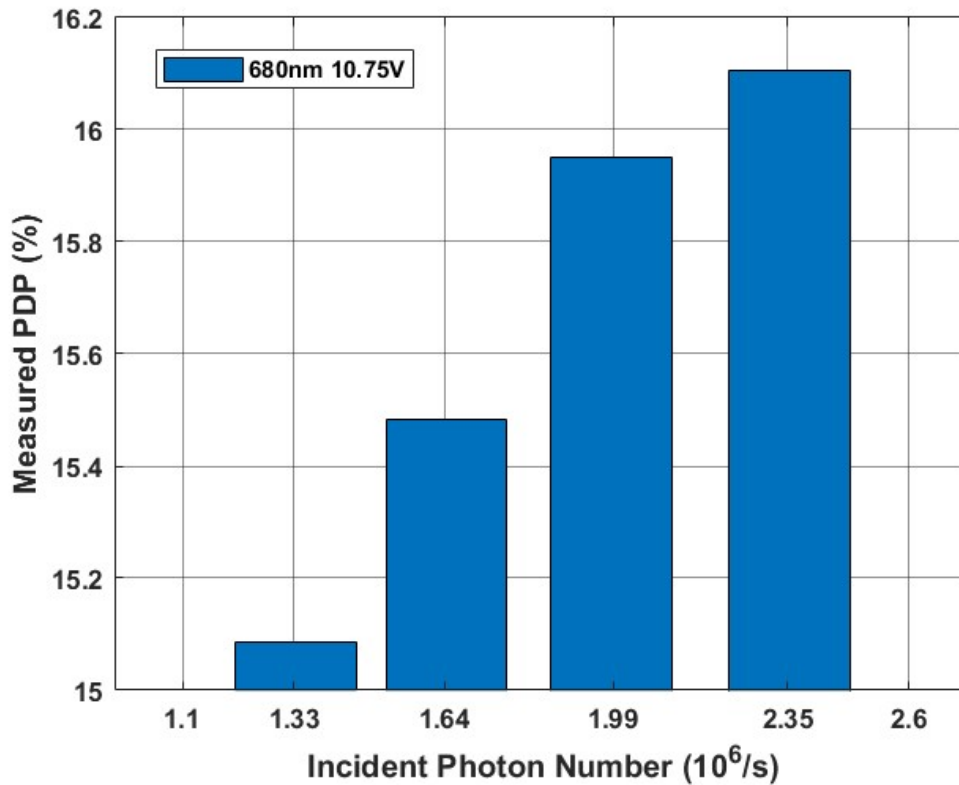


Figure 5-13. Measured PDP at 10.75 V biasing voltage, 680-nm incident light with different incident photon numbers.

While gradually increasing the incident light intensity, the incident photon numbers also increase, thus improving the PDP. This increasing trend tends to be slower as too many incident photons may saturate the SPADs. In this case, for larger SPADs, an unreasonable large incident light intensity can cause the count loss, thus actually decreasing the measured PDP. For comparing different SPAD's PDP, it is

more important to pay attention to the measurement settings, which can bring deviations that are larger than the deviations due to the edge effect.

5.4. Conclusions

From the measurement of the designed SPADs, all the SPADs have shown decent PDP with acceptable DCR levels. Table 5-2 has listed the comparison between the designed SPADs and SPADs from previous designs, the DCR has shown an improvement compared to previous results. Due to the implementation of output buffers, the designed PQR SPADs can achieve a low DCR as the output buffers can filter some pulses with small magnitudes.

Ref	Configuration	Technology	DCR	PDP	AP	FoM _t **
[48]	AQR	65 nm standard CMOS	24.08 kHz (V _{ex} = 0.8 V)*	42.9 % (420 nm V _{ex} = 0.8 V)	unknown	0.087
[51]	AQR	65 nm standard CMOS	21 kHz (V _{ex} = 0.5V)	23.8 % (420 nm V _{ex} = 0.5 V)	~ 0 %	0.052
[59]	PQR	180 nm standard CMOS	76.68 kHz (V _{ex} = 0.5 V)	7.35 % (560 nm V _{ex} = 0.5 V)	~ 0 %	0.0084
This work	PQR	65 nm standard CMOS	23.697 kHz (V _{ex} = 0.9 V)	30 % (420 nm V _{ex} = 0.6 V)	~ 0 %	0.062

* Best value was selected instead of mean value.

** Based on the Equation 2-2, calculated with available parameters.

Compared to several recent reported SPADs, the designed SPAD has shown decent performance over the DCR and PDP. The calculated FoM_t achieves similar value as AQR-based SPADs. But when it comes to the application where timing

information is important, the dead time and timing jitter of AQR SPADs may have advantages. However, in this SPAD design, the implementation of output buffers also assists the PQR SPAD's potential in high-speed applications. The designed passive-quench SPADs with output buffers can not only be used in the short-wavelength ranges, but also have a great potential in the applications of near-infrared (NIR) range. The measured DCR and PDP of the fabricated SPADs were also compared with the proposed 1-D SPAD model and optimized 2-D SPAD model. For the DCR, the proposed 2-D model can achieve more accurate predictions. While for the PDP models, we believe that more efforts should be put in the improvement of simulating light transmissions. When comparing the measured DCR and PDP of 5 SPADs, there were certain differences between the modeled results and the measurements. The first reason is due to variations from multiple sources in the actual measurement, such as the voltage stability, temperature variation, and measurement setup. Especially, the effect of the measurement setup can have significant influence on the PDP measurement. Therefore, more investigations should be put on the fair comparison and perfect tuning of the measurement conditions.

Chapter 6

CONCLUSIONS AND FUTURE WORK

6.1. Conclusions

In the thesis research work, a comprehensive research process of Single-Photon Avalanche Diodes (SPADs) was explored, including motivation and applications, literature review, improved SPAD modeling process, design, fabrication, and measurement. SPADs are highly promising candidates in the single-photon-counting (SPC) techniques. Being able to integrate with front-end CMOS circuits and TDCs, SPADs have great potential in automotive applications like LiDAR systems. In the review of SPAD's performance in recent LiDAR applications, we developed FoMs to evaluate SPAD's performance as a sensor in the pulsed LiDAR systems. Based on the comparison, the influence of different technologies can have a huge impact on the total performance. However, there were few studies that focused on the SPAD modeling work and process. In this case, we continued to review the development of SPAD models in Chapter 2. From the review of SPAD models, we have found that the lack of technology-related parameter information, simplistic 1-D equations, and inefficient SPAD modeling process may count for the inaccurate SPAD models. In this case, we summarized several challenges in the SPAD modeling process according to the literature review in Chapter 2. Based on the research challenges in SPAD modeling, we proposed our own SPAD modeling method by combining TCAD and MATLAB for more accurate and efficient predictions on SPAD's important parameters: DCR and PDP.

In the development of SPAD models, we investigated the influence of each stage of the entire modeling process, starting with the modeling fundamentals. First, detailed equations regarding the DCR models were derived from actual physics. By considering various mechanisms, we simulated the avalanche triggering probability, generation rate

of SRH process and BTBT process. Due to the lack of trap information in the technology, the TAT was neglected to improve the reliability of the model. Based on the 65 nm standard CMOS technology used and previous research results from the group, initial values such as the doping concentration, size, and structures were adopted in the simulation. Those values were calibrated after the fabrication of the SPADs, which achieved improved accuracy. The simulation of the SPAD models include the I-V characteristics, generation rate due to SRH, BTBT, TAT, and photon absorption. To further improve the accuracy of the proposed SPAD models, we innovatively proposed a 2-D simulation which considered the edge effect. Specifically, the simulated DCR based on 2-D models were lower than the DCR simulated using traditional 1-D model due to the reduced avalanche triggering probability near the edge region. The distribution of the DCR and PDP along the active region was obtained by splitting the half structure of the active region into 25 parts. In addition to the simulation based on one device, 5 SPADs with different sizes were simulated and compared, indicating a higher influence of edge effect on the small SPADs. To solve the problem of low efficient modeling process, we further proposed a fully automated simulation process by utilizing the `tcl` commands in TCAD. As a result, with a range of parameters that are of interest specified, the simulation can be finished automatically without manual modifications. The desired output can also be stored and processed in MATLAB to generate figures and tables automatically with certain commands. The proposed 1-D SPAD model, 2-D SPAD model, and simulation automation can achieve higher accuracy and efficiency.

Following the modeling process of SPAD structures, the layouts of SPADs and related circuits were designed based on TSMC 65 nm standard CMOS technology. Detailed explanation of the design process and layer specifications were discussed. Octagonal SPADs were designed to achieve good symmetry and keep consistent with simulations in Chapter 3. The designed SPADs were measured to compare with simulation regarding the I-V characteristics, the I-V characteristics were used to calibrate the original SPICE model. By varying the SPAD resistance used in the SPICE model, the simulated I-V characteristics were closer to the measurement. However, capacitance should also be a reasonable value to have correct output waveforms. Based

on the simulations and measurement in Chapter 4, the major challenges for accurate SPICE models mainly include accurate resistance and capacitance.

The SPADs with output buffers were also measured using a high-speed oscilloscope 625-Zi. First, the BVs of the fabricated SPADs were measured using a semiconductor analyzer. The measured BVs of multiple SPAD replicas were used to calibrate the doping concentration value in the TCAD model. After the calibration on doping concentration, the simulated BV was very consistent with the measurement. Therefore, the simulated DCR and PDP could be closer to the realistic values. Based on the calibrated SPAD structure, the DCR and PDP were simulated and compared to the measured data. The comparison has shown a good agreement with SPAD's DCR. The simulated voltage dependence of DCR was consistent with the measured data, indicating BTBT has a dominant contribution on the total DCR. In general, the simulated DCR at various biasing voltages were higher than the measured data, which could be because of two reasons: the edge effect and the filtering effect due to the output buffers connected. In this case, the simulated DCR based on 2-D model was compared to 1-D DCR and measured DCR, showing an obvious improvement of accuracy while maintaining the good voltage dependence. In addition to the DCR comparison, the PDP comparison between the simulation and measurement was also conducted. The PDP was measured at different wavelengths and biasing voltages. However, due to the complex reflection between layers with unknown refractive indexes, there was a deviation between the simulation and measurement at some specific wavelengths. But the overall trend of the PDP wavelength dependence has shown a good consistency. Compared to DCR modeling, there are more efforts to be done in the future to improve the model accuracy, mainly related to the light transmission stage. In summary, the thesis work has proposed a complete and efficient SPAD modeling process with the consideration of edge effect. The proposed model achieved decent accuracy and certain improvements on DCR and PDP. Based on the literature review, modeling process, design procedure, and measurements explored, some important future directions can be summarized to further improve the development of SPADs.

6.2. Future Works

To develop suitable SPADs for certain applications based on advanced CMOS technologies, there still are some research challenges to be addressed. Consequently, this section highlights potential avenues for future exploration across various dimensions:

1. SPADs for Specific Applications

Although there are some FoMs available for evaluating the individual SPADs and even SPAD arrays, system-level FoMs are still needed to relate basic SPAD parameters to system performances. For example, in LiDAR applications, it is challenging to have accurate predictions on the system-level performance based on basic parameters. However, there are several simulation-based models that were proposed to simulate the performance of LiDAR systems under specific conditions [24], [179]–[181]. While some of the models were based on fixed environmental conditions, such as the reflectivity and illumination level, they are still very useful to provide guidance in sensor design for different applications. In the future, multiple factors may be introduced in the FoM of SPAD-based LiDAR systems to reflect the real environment, so that the FoM can predict the performance of the whole system at different conditions. Specifically, an FoM that combines laser's parameters, SPAD's basic parameters, TDC's performances, background illumination level will be very useful to evaluate a LiDAR system's resolution, frame rate, speed, and sensitivity.

2. Improvements on the Process, Voltage, and Temperature (PVT) Variations

The SPAD design may suffer from the PVT variations a lot, especially when SPADs are integrated into arrays. For instance, SPADs in an array can be designed to operate in different time windows to reduce the noise from undesired sources of the environment. However, the time window at different temperatures is affected by the PVT variations, as shown in Figure 6-1, which is a simulation of a specific time window. When it comes to the real operations, this variation can even be larger. The layout and the micrograph of the designed SPAD array is shown in Figure 6-2.

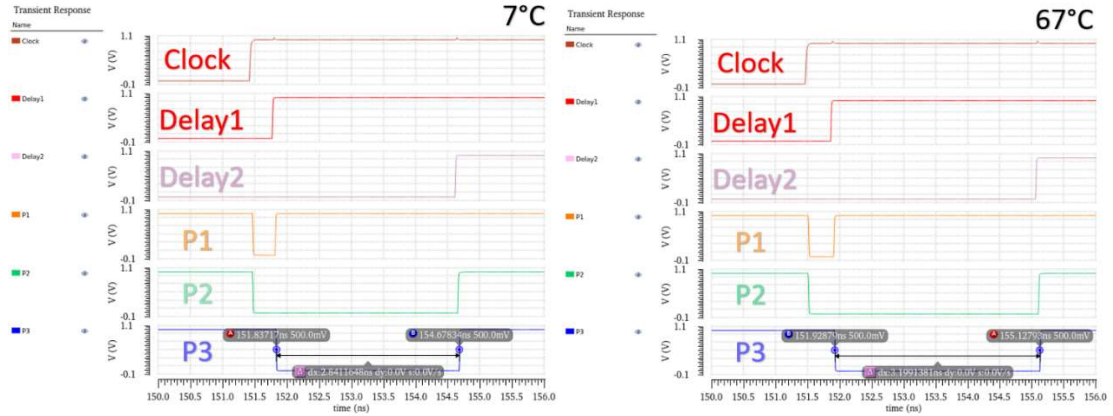


Figure 6-1. Simulation of time window at two different temperatures.

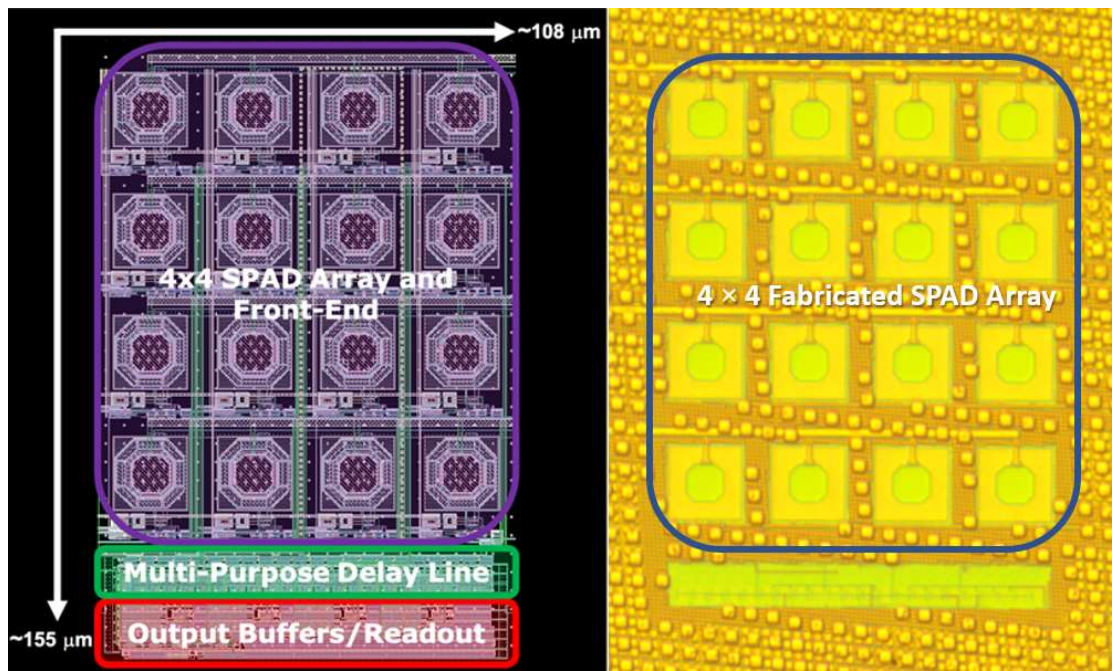


Figure 6-2. Layout and the micrograph of the designed SPAD array.

3. Novel SPAD Structures

With emerging technologies, the SPAD designs may vary a lot. While most of the SPADs discussed in the thesis are frontside-illuminated (FSI) SPADs, there are some emerging SPAD designs that are based on backside-illuminated (BSI) techniques. For the BSI SPAD shown in Figure 6-3 (a) and (b), the light is illuminated from the backside of the SPAD.

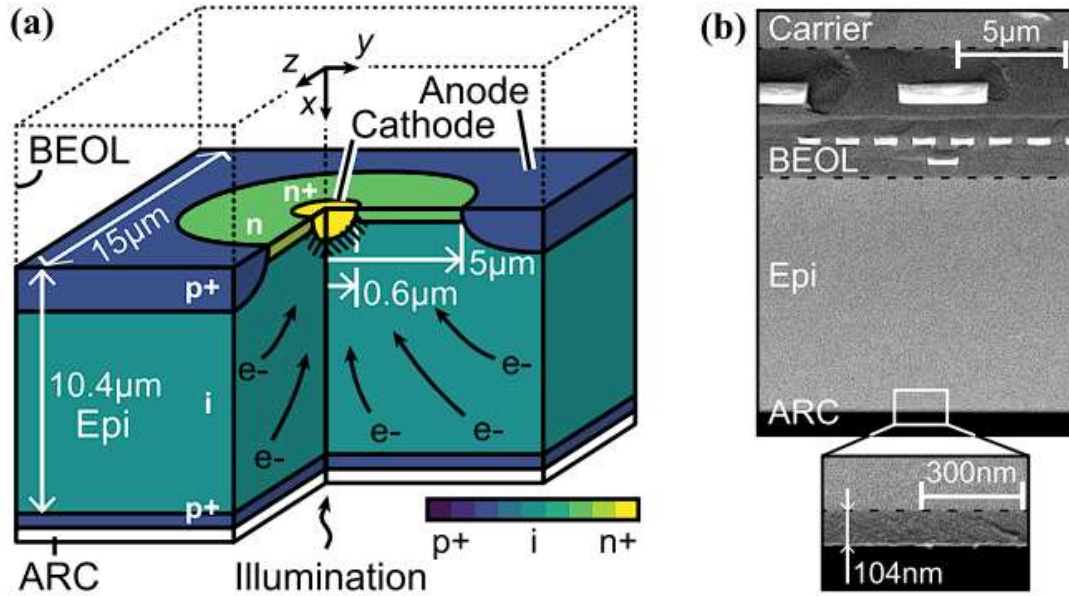


Figure 6-3. An example of (a) Cross-sectional view and (b) SEM image of a BSI SPAD [47],
Copyright © 2022, IEEE.

A thick epi-layer with lower doping concentration can increase the width of the depletion region, thus improving the absorption of photons. This thick epi-layer can also shift the PDP peak to a longer wavelength, which could be helpful for LiDAR applications operating in NIR wavelengths. With reduced reflections due to the anti-reflection-coating (ARC) layer, there is almost no ripple in the PDP versus wavelengths plot [136], [137], [182]. For BSI SPADs, the light comes in from the back side, so it will not affect the layout above the SPAD, which may improve the area efficiency and reduce the reflections. Therefore, more efforts may be needed to optimize SPAD design that is based on BSI technology in the future, especially when the SPADs are used in near-infrared (NIR) applications.

4. Optimized SPAD Models with Machine Learning

The 2-D SPAD model can improve the accuracy of simulations compared to 1-D SPAD models. However, when it comes to some SPAD structures that are not symmetric at all, a 3-D SPAD model may become necessary. One of the biggest challenges in the development of 3-D SPAD models is the convergence problem. The convergence issue can be more important due to the rapid change of physical parameters during the avalanche process. To avoid the convergence problem, sufficient data points are needed. However, the computational cost will hugely increase when extending from 2-D to 3-D. To overcome this problem, machine learning techniques

can be adopted in SPAD modeling processes. With machine learning, the design parameters like doping concentration, dimension or size, shape, as well as other parameters, can be investigated to see their influence on the specific performance of SPADs. With more data available from simulations, machine learning models can be more accurate. Therefore, predictions of SPAD performances based on different technologies can be made without the need for iterative modeling process again. And it can be more achievable to simulate 3-D structures with a lot more data points with the assistance of machine learning trained model.

5. Multi-physics Simulation

The TCAD-based simulation is convenient for modeling basic SPAD parameters like DCR and PDP. A further investigation may be necessary and possible to improve the accuracy of predictions. Currently, TCAD is commonly used for simulating electric parameters of SPADs including the electric field distributions, ionization coefficients, and breakdown voltage, but not their noise performance [153]. However, the temperature during the avalanche may vary a lot due to the heating effect of large current. And such temperature variations also affect the DCR and PDP a lot. Therefore, multi-physics simulations may be combined with traditional TCAD simulations. Some tools like the COMSOL Multiphysics can be used to simulate the real-time temperature properties of SPAD. In this case, the self-heating effect can be considered in the SPAD models.

6. Device-Circuit Combined Simulation

SPAD circuit models can only be used to simulate the electrical performance of SPADs in integrated circuits. It would be significant progress if SPAD device models and SPAD circuit models can be combined. In this case, the input can be a light signal in the simulation, instead of the electric stimuli used in existing SPAD circuit models (SPICE models). However, this method also requires the development of software, to include the function of simulating multi-physics in circuits.

REFERENCES

- [1] M. Gerstmaier, A. Melzer, A. Onic, and M. Huemer, “On the Safe Road Toward Autonomous Driving: Phase Noise Monitoring in Radar Sensors for Functional Safety Compliance,” *IEEE Signal Process Mag*, vol. 36, no. 5, pp. 60–70, Sep. 2019, doi: 10.1109/MSP.2019.2902914.
- [2] A. Iqbal, S. S. Ahmed, M. D. Tauqeer, A. Sultan, and S. Y. Abbas, “Design of Multifunctional Autonomous Car using Ultrasonic and Infrared Sensors,” *2017 International Symposium on Wireless Systems and Networks, ISWSN 2017*, vol. 2018-January, pp. 1–5, Jul. 2017, doi: 10.1109/ISWSN.2017.8250023.
- [3] R. Hussain and S. Zeadally, “Autonomous Cars: Research Results, Issues, and Future Challenges,” *IEEE Communications Surveys and Tutorials*, vol. 21, no. 2, pp. 1275–1313, Apr. 2019, doi: 10.1109/COMST.2018.2869360.
- [4] L. De Paula Veronese *et al.*, “Evaluating the Limits of a LiDAR for an Autonomous Driving Localization,” *IEEE Transactions on Intelligent Transportation Systems*, vol. 22, no. 3, pp. 1449–1458, Mar. 2021, doi: 10.1109/TITS.2020.2971054.
- [5] J. Lee, S. Hwang, W. J. Kim, and S. Lee, “SAM-Net: LiDAR Depth Inpainting for 3D Static Map Generation,” *IEEE Transactions on Intelligent Transportation Systems*, vol. 23, no. 8, pp. 12213–12228, Aug. 2022, doi: 10.1109/TITS.2021.3111046.
- [6] L. Liu, J. He, K. Ren, Z. Xiao, and Y. Hou, “A LiDAR-Camera Fusion 3D Object Detection Algorithm,” *Information 2022, Vol. 13, Page 169*, vol. 13, no. 4, p. 169, Mar. 2022, doi: 10.3390/INFO13040169.
- [7] J. Mendez, M. Molina, N. Rodriguez, M. P. Cuellar, and D. P. Morales, “Camera-LiDAR Multi-Level Sensor Fusion for Target Detection at the Network Edge,” *Sensors 2021*, vol. 21, no. 12, p. 3992, Jun. 2021, doi: 10.3390/S21123992.
- [8] N. Radwell, A. Selyem, L. Mertens, M. P. Edgar, and M. J. Padgett, “Hybrid 3D Ranging and Velocity Tracking System Combining Multi-View Cameras and Simple LiDAR,” *Scientific Reports 2019 9:1*, vol. 9, no. 1, pp. 1–7, Mar. 2019, doi: 10.1038/s41598-019-41598-z.
- [9] H. ; Yi *et al.*, “Extrinsic Calibration for LiDAR-Camera Systems Using Direct 3D-2D Correspondences,” *Remote Sensing 2022*, vol. 14, no. 23, p. 6082, Nov. 2022, doi: 10.3390/RS14236082.
- [10] C. Debeunne and D. Vivet, “A Review of Visual-LiDAR Fusion based Simultaneous Localization and Mapping,” *Sensors 2020*, vol. 20, no. 7, p. 2068, Apr. 2020, doi: 10.3390/S20072068.
- [11] D. J. Yeong, G. Velasco-hernandez, J. Barry, and J. Walsh, “Sensor and Sensor Fusion Technology in Autonomous Vehicles: A Review,” *Sensors 2021*, vol. 21, no. 6, p. 2140, Mar. 2021, doi: 10.3390/S21062140.
- [12] B. Behroozpour, P. A. M. Sandborn, M. C. Wu, and B. E. Boser, “Lidar System Architectures and Circuits,” *IEEE Communications Magazine*, vol. 55, no. 10, pp. 135–142, Oct. 2017, doi: 10.1109/MCOM.2017.1700030.
- [13] D. Wang, C. Watkins, and H. Xie, “MEMS Mirrors for LiDAR: A Review,” *Micromachines 2020*, vol. 11, no. 5, p. 456, Apr. 2020, doi: 10.3390/MI11050456.

- [14] N. Li *et al.*, “A Progress Review on Solid-State LiDAR and Nanophotonics-Based LiDAR Sensors,” *Laser Photon Rev*, vol. 16, no. 11, p. 2100511, Nov. 2022, doi: 10.1002/LPOR.202100511.
- [15] I. Kim *et al.*, “Nanophotonics for Light Detection and Ranging Technology,” *Nature Nanotechnology 2021 16:5*, vol. 16, no. 5, pp. 508–524, May 2021, doi: 10.1038/s41565-021-00895-3.
- [16] Y. Barkana and M. Belkin, “Laser Eye Injuries,” *Surv Ophthalmol*, vol. 44, no. 6, pp. 459–478, May 2000, doi: 10.1016/S0039-6257(00)00112-0.
- [17] F. Villa, F. Severini, F. Madonini, and F. Zappa, “SPADs and SiPMs Arrays for Long-Range High-Speed Light Detection and Ranging (LiDAR),” *Sensors 2021*, vol. 21, no. 11, p. 3839, Jun. 2021, doi: 10.3390/S21113839.
- [18] J. D. Spinhirne, “Micro Pulse Lidar,” *IEEE Transactions on Geoscience and Remote Sensing*, vol. 31, no. 1, pp. 48–55, 1993, doi: 10.1109/36.210443.
- [19] Y. Li and J. Ibanez-Guzman, “Lidar for Autonomous Driving: The Principles, Challenges, and Trends for Automotive Lidar and Perception Systems,” *IEEE Signal Process Mag*, vol. 37, no. 4, pp. 50–61, Jul. 2020, doi: 10.1109/MSP.2020.2973615.
- [20] J. P. Godbaz, M. J. Cree, and A. A. Dorrington, “Understanding and Ameliorating Non-Linear Phase and Amplitude Responses in AMCW Lidar,” *Remote Sensing 2012*, vol. 4, no. 1, pp. 21–42, Dec. 2011, doi: 10.3390/RS4010021.
- [21] B. Kim, S. Park, J. H. Chun, J. Choi, and S. J. Kim, “7.2 A 48 × 4013.5 mm Depth Resolution Flash LiDAR Sensor with In-Pixel Zoom Histogramming Time-to-Digital Converter,” *Dig Tech Pap IEEE Int Solid State Circuits Conf*, vol. 64, pp. 108–110, Feb. 2021, doi: 10.1109/ISSCC42613.2021.9366022.
- [22] S. Park, B. Kim, J. Cho, J. H. Chun, J. Choi, and S. J. Kim, “An 80×60 Flash LiDAR Sensor with In-Pixel Histogramming TDC Based on Quaternary Search and Time-Gated Δ -Intensity Phase Detection for 45m Detectable Range and Background Light Cancellation,” *Dig Tech Pap IEEE Int Solid State Circuits Conf*, vol. 2022-February, pp. 98–100, 2022, doi: 10.1109/ISSCC42614.2022.9731112.
- [23] W. Xu, C. Yan, W. Jia, X. Ji, and J. Liu, “Analyzing and Enhancing the Security of Ultrasonic Sensors for Autonomous Vehicles,” *IEEE Internet Things J*, vol. 5, no. 6, pp. 5015–5029, Dec. 2018, doi: 10.1109/IIOT.2018.2867917.
- [24] J. Kostamovaara, S. S. Jahromi, and P. Keränen, “Temporal and Spatial Focusing in SPAD-Based Solid-State Pulsed Time-of-Flight Laser Range Imaging,” *Sensors 2020*, vol. 20, no. 21, p. 5973, Oct. 2020, doi: 10.3390/S20215973.
- [25] P. Keränen and J. Kostamovaara, “256×8 SPAD Array with 256 Column TDCs for a Line Profiling Laser Radar,” *IEEE Transactions on Circuits and Systems I: Regular Papers*, vol. 66, no. 11, pp. 4122–4133, Nov. 2019, doi: 10.1109/TCSI.2019.2923263.
- [26] Z. Dai, A. Wolf, P. P. Ley, T. Glück, M. C. Sundermeier, and R. Lachmayer, “Requirements for Automotive LiDAR Systems,” *Sensors 2022*, vol. 22, no. 19, p. 7532, Oct. 2022, doi: 10.3390/S22197532.
- [27] “Innovation Matters 256 x 16 SPAD Array and 16-Channel Ultrashort Pulsed Laser Driver for Automotive LIDAR”, Accessed: Jul. 08, 2023. [Online]. Available: https://www.imagesensors.org/Past%20Workshops/2020%20ISSW/Andre_Srowig_ISW2020.pdf
- [28] “MAVIN™ with Perception Dynamic Range Performance with Object Detection, Classification, and Tracking,” 2023, Accessed: Jul. 08, 2023. [Online]. Available: https://microvision.com/resources/persistent/b79cf3758d8df73f3b1ace864eb05902b0534026/Productsheet_MAVIN%E2%84%A2_05.23.pdf

- [29] “Advanced LiDAR Technology for Autonomous Vehicles | Innoviz.”, 2023, Accessed: Jul. 08, 2023. [Online]. Available: <https://innoviz.tech/>.
- [30] “Surround Lidar | Velodyne Lidar.”, 2023, Accessed: Jul. 08, 2023. [Online]. Available: <https://velodynelidar.com/surround-lidar/>.
- [31] “IMX459 - Sony Semiconductor Solutions Corporation | CMOS Image Sensor.”, 2023, Accessed: Jul. 08, 2023. [Online]. Available: <https://www.gophotonics.com/products/cmos-image-sensors/sony-corporation/21-209-imx459>.
- [32] “Product Selector | ams OSRAM.”, 2023, Accessed: Jul. 08, 2023. [Online]. Available: https://ams-osram.com/products/product-selector?menu%5Bproduct_group%5D=Sensors&query=&refinementList%5Bproduct_type_content%5D%5B0%5D=Distance%20%26%20Proximity%20Sensors&page=1.
- [33] W. Jiang, Y. Chalich, and M. J. Deen, “Sensors for Positron Emission Tomography Applications,” *Sensors 2019*, vol. 19, no. 22, p. 5019, Nov. 2019, doi: 10.3390/S19225019.
- [34] A. I. Carswell, D. P. Donovan, and J. A. Whiteway, “Correction for Nonlinear Photon-Counting Effects in Lidar Systems,” *Applied Optics*, vol. 32, no. 33, pp. 6742–6753, Nov. 1993, doi: 10.1364/AO.32.006742.
- [35] Z. Zhang *et al.*, “Ranging Performance Model Considering the Pulse Pileup Effect for PMT-Based Photon-Counting Lidars,” *Optics Express*, vol. 28, no. 9, pp. 13586–13600, Apr. 2020, doi: 10.1364/OE.386107.
- [36] Y. Wang, Y. Xu, P. Chen, and K. Liang, “Remote Sensing of Seawater Temperature and Salinity Profiles by the Brillouin Lidar Based on a Fizeau Interferometer and Multichannel Photomultiplier Tube,” *Sensors 2023*, vol. 23, no. 1, p. 446, Dec. 2022, doi: 10.3390/S23010446.
- [37] D. A. Orlov, R. Glazeborg, R. Ortega, and E. Kernen, “UV/visible High-Sensitivity MCP-PMT Single-Photon GHz Counting Detector for Long-Range Lidar Instrumentations,” *CEAS Space Journal*, vol. 11, no. 4, pp. 405–411, Dec. 2019, doi: 10.1007/S12567-019-00260-0/FIGURES/7.
- [38] M. J. Deen and P. K. Basu, *Silicon Photonics: Fundamentals and Devices*. John Wiley and Sons Ltd, 2012. doi: 10.1002/9781119945161.
- [39] K. Wu *et al.*, “Blind Zone-Suppressed Hybrid Beam Steering for Solid-State Lidar,” *Photonics Research*, vol. 9, no. 9, pp. 1871–1880, Sep. 2021, doi: 10.1364/PRJ.424393.
- [40] Y.-C. Chang *et al.*, “2D Beam Steerer Based on Metalens on Silicon Photonics,” *Optics Express*, vol. 29, no. 2, pp. 854–864, Jan. 2021, doi: 10.1364/OE.409711.
- [41] G. Adamo and A. Busacca, “Time of Flight Measurements via Two LiDAR Systems with SiPM and APD,” *AEIT 2016 - International Annual Conference: Sustainable Development in the Mediterranean Area, Energy and ICT Networks of the Future*, 2016, doi: 10.23919/AEIT.2016.7892802.
- [42] Y. Li, X. Luo, G. Liang, and G. Q. Lo, “Demonstration of Ge/Si Avalanche Photodetector Arrays for Lidar Application,” *Optical Fiber Communication Conference (OFC) 2019 (2019), paper Tu3E.3*, p. Tu3E.3, Mar. 2019, doi: 10.1364/OFC.2019.TU3E.3.
- [43] S. Cova, A. Longoni, and A. Andreoni, “Towards Picosecond Resolution with Single-Photon Avalanche Diodes,” *Review of Scientific Instruments*, vol. 52, no. 3, p. 408, Jun. 1998, doi: 10.1063/1.1136594.

- [44] Y.-X. Lin *et al.*, “A 4-D FMCW LiDAR with Ultra-High Velocity Sensitivity,” *Journal of Lightwave Technology*, pp. 1–11, 2023, doi: 10.1109/JLT.2023.3292139.
- [45] X. Liu *et al.*, “High-Performance Cascaded Surface-Illuminated Ge-on-Si APD Array,” *IEEE Electron Device Letters*, vol. 44, no. 2, pp. 205–208, Feb. 2023, doi: 10.1109/LED.2022.3233038.
- [46] Z. Cheng and B. A. S. Xi, “CMOS Based Single Photon Avalanche Diode and Time-to-Digital Converter Towards PET Imaging Applications” 2016, Accessed: Mar. 11, 2023. [Online]. Available: <https://macsphere.mcmaster.ca/handle/11375/20472>
- [47] E. Van Sieleghem *et al.*, “A Backside-Illuminated Charge-Focusing Silicon SPAD with Enhanced Near-Infrared Sensitivity,” *IEEE Trans Electron Devices*, vol. 69, no. 3, pp. 1129–1136, Mar. 2022, doi: 10.1109/TED.2022.3143487.
- [48] R. Scott, W. Jiang, X. Qian, and M. J. Deen, “A Multi-Time-Gated SPAD Array with Integrated Coarse TDCs,” *Electronics 2022*, vol. 11, no. 13, p. 2015, Jun. 2022, doi: 10.3390/ELECTRONICS11132015.
- [49] W. Jiang, Y. Chalich, R. Scott, and M. J. Deen, “Time-Gated and Multi-Junction SPADs in Standard 65 nm CMOS Technology,” *IEEE Sens J*, vol. 21, no. 10, pp. 12092–12103, May 2021, doi: 10.1109/JSEN.2021.3063319.
- [50] W. Jiang, R. Scott, and M. J. Deen, “Differential Quench and Reset Circuit for Single-Photon Avalanche Diodes,” *Journal of Lightwave Technology*, vol. 39, no. 22, pp. 7334–7342, Nov. 2021, doi: 10.1109/JLT.2021.3111119.
- [51] W. Jiang, R. Scott, and M. J. Deen, “High-Speed Active Quench and Reset Circuit for SPAD in a Standard 65 nm CMOS Technology,” *IEEE Photonics Technology Letters*, vol. 33, no. 24, pp. 1431–1434, Dec. 2021, doi: 10.1109/LPT.2021.3124989.
- [52] M. Perenzoni, L. Pancheri, and D. Stoppa, “Compact SPAD-Based Pixel Architectures for Time-Resolved Image Sensors,” *Sensors 2016*, vol. 16, no. 5, p. 745, May 2016, doi: 10.3390/S16050745.
- [53] D. Bronzi, F. Villa, S. Tisa, A. Tosi, and F. Zappa, “SPAD Figures of Merit for Photon-Counting, Photon-Timing, and Imaging Applications: A Review,” *IEEE Sens J*, vol. 16, no. 1, pp. 3–12, Jan. 2016, doi: 10.1109/JSEN.2015.2483565.
- [54] D. P. Palubiak and M. J. Deen, “CMOS SPADs: Design Issues and Research Challenges for Detectors, Circuits, and Arrays,” *IEEE Journal of Selected Topics in Quantum Electronics*, vol. 20, no. 6, pp. 409–426, Nov. 2014, doi: 10.1109/JSTQE.2014.2344034.
- [55] X. Qian, W. Jiang, A. Elsharabasy, and M. J. Deen, “Modeling for Single-Photon Avalanche Diodes: State-of-the-Art and Research Challenges,” *Sensors 2023*, vol. 23, no. 7, p. 3412, Mar. 2023, doi: 10.3390/S23073412.
- [56] T. Baba *et al.*, “Development of an InGaAs SPAD 2D Array for Flash LIDAR,” *Quantum Sensing and Nano Electronics and Photonics XV*, vol. 10540, no. 26, pp. 81–94, Jan. 2018, doi: 10.1117/12.2289270.
- [57] S. W. Hutchings *et al.*, “A Reconfigurable 3-D-Stacked SPAD Imager with In-Pixel Histogramming for Flash LIDAR or High-Speed Time-of-Flight Imaging,” *IEEE J Solid-State Circuits*, vol. 54, no. 11, pp. 2947–2956, Nov. 2019, doi: 10.1109/JSSC.2019.2939083.
- [58] T. H. Sang, S. Tsai, and T. Yu, “Mitigating Effects of Uniform Fog on SPAD Lidars,” *IEEE Sens Lett*, vol. 4, no. 9, Sep. 2020, doi: 10.1109/LESENS.2020.3018708.
- [59] W. Jiang, R. Scott, and M. Jamal Deen, “Improved Noise Performance of CMOS Poly Gate Single-Photon Avalanche Diodes,” *IEEE Photonics J*, vol. 14, no. 1, Feb. 2022, doi: 10.1109/JPHOT.2021.3128055.

- [60] J. A. Richardson, E. A. G. Webster, L. A. Grant, and R. K. Henderson, "Scaleable Single-Photon Avalanche Diode Structures in Nanometer CMOS Technology," *IEEE Trans Electron Devices*, vol. 58, no. 7, pp. 2028–2035, Jul. 2011, doi: 10.1109/TED.2011.2141138.
- [61] E. A. G. Webster, J. A. Richardson, L. A. Grant, D. Renshaw, and R. K. Henderson, "A Single-Photon Avalanche Diode in 90-nm CMOS Imaging Technology with 44% Photon Detection Efficiency at 690 nm," *IEEE Electron Device Letters*, vol. 33, no. 5, pp. 694–696, May 2012, doi: 10.1109/LED.2012.2187420.
- [62] T. Leitner *et al.*, "Measurements and Simulations of Low Dark Count Rate Single Photon Avalanche Diode Device in a Low Voltage 180-nm CMOS Image Sensor Technology," *IEEE Trans Electron Devices*, vol. 60, no. 6, pp. 1982–1988, 2013, doi: 10.1109/TED.2013.2259172.
- [63] M. Moreno-García, L. Pancheri, M. Perenzoni, R. Del Río, Ó. Guerra Vinuesa, and Á. Rodríguez-Vázquez, "Characterization-Based Modeling of Retriggering and Afterpulsing for Passively Quenched CMOS SPADs," *IEEE Sens J*, vol. 19, no. 14, pp. 5700–5709, Jul. 2019, doi: 10.1109/JSEN.2019.2903937.
- [64] W. Jiang and M. J. Deen, "Random Telegraph Signal in n+/p-Well CMOS Single-Photon Avalanche Diodes," *IEEE Trans Electron Devices*, vol. 68, no. 6, pp. 2764–2769, Jun. 2021, doi: 10.1109/TED.2021.3070557.
- [65] L. Pancheri and L. Pancheri, "Characterization and Modeling of Displacement Damage in CMOS SPAD Sensors The International SPAD Sensor Workshop Online conference Outline," 2022.
- [66] S. M. Patanwala *et al.*, "A High-Throughput Photon Processing Technique for Range Extension of SPAD-Based LiDAR Receivers," *IEEE Open Journal of the Solid-State Circuits Society*, vol. 2, pp. 12–25, Oct. 2021, doi: 10.1109/OJSSCS.2021.3118987.
- [67] M. Beer, J. F. Haase, J. Ruskowski, and R. Kokozinski, "Background Light Rejection in SPAD-Based LiDAR Sensors by Adaptive Photon Coincidence Detection," *Sensors* 2018, vol. 18, no. 12, p. 4338, Dec. 2018, doi: 10.3390/S18124338.
- [68] J. Hu, B. Liu, R. Ma, M. Liu, and Z. Zhu, "A 32×32 -Pixel Flash LiDAR Sensor With Noise Filtering for High-Background Noise Applications," *IEEE Transactions on Circuits and Systems I: Regular Papers*, vol. 69, no. 2, pp. 645–656, Feb. 2022, doi: 10.1109/TCSI.2020.3048367.
- [69] S. Lindner, C. Zhang, I. M. Antolovic, M. Wolf, and E. Charbon, "A 252×144 SPAD Pixel Flash Lidar with 1728 Dual-Clock 48.8 ps TDCs, Integrated Histogramming and 14.9-to-1 Compression in 180nm CMOS Technology," *IEEE Symposium on VLSI Circuits, Digest of Technical Papers*, vol. 2018-June, pp. 69–70, Oct. 2018, doi: 10.1109/VLSIC.2018.8502386.
- [70] P. Padmanabhan *et al.*, "7.4 A 256×128 3D-Stacked (45nm) SPAD FLASH LiDAR with 7-Level Coincidence Detection and Progressive Gating for 100m Range and 10klux Background Light," *Dig Tech Pap IEEE Int Solid State Circuits Conf*, vol. 64, pp. 111–113, Feb. 2021, doi: 10.1109/ISSCC42613.2021.9366010.
- [71] C. Zhang, S. Lindner, I. M. Antolovic, J. Mata Pavia, M. Wolf, and E. Charbon, "A 30-frames/s, 252×144 SPAD Flash LiDAR with 1728 Dual-Clock 48.8-ps TDCs, and Pixel-Wise Integrated Histogramming," *IEEE J Solid-State Circuits*, vol. 54, no. 4, pp. 1137–1151, Apr. 2019, doi: 10.1109/JSSC.2018.2883720.
- [72] W. Jiang, Y. Chalich, and M. J. Deen, "Sensors for Positron Emission Tomography Applications," *Sensors* 2019, vol. 19, no. 22, p. 5019, Nov. 2019, doi: 10.3390/S19225019.

- [73] M. M. El-Desouki, D. Palubiak, M. J. Deen, Q. Fang, and O. Marinov, "A Novel, High-Dynamic-Range, High-Speed, and High-Sensitivity CMOS Imager using Time-Domain Single-Photon Counting and Avalanche Photodiodes," *IEEE Sens J*, vol. 11, no. 4, pp. 1078–1083, 2011, doi: 10.1109/JSEN.2010.2058846.
- [74] D. P. Palubiak and M. J. Deen, "CMOS SPADs: Design Issues and Research Challenges for Detectors, Circuits, and Arrays," *IEEE Journal of Selected Topics in Quantum Electronics*, vol. 20, no. 6, pp. 409–426, Nov. 2014, doi: 10.1109/JSTQE.2014.2344034.
- [75] R. J. McINTYRE, "Multiplication Noise in Uniform Avalanche Diodes," *IEEE Trans Electron Devices*, vol. ED-13, no. 1, pp. 164–168, 1966, doi: 10.1109/T-ED.1966.15651.
- [76] Y. Liu *et al.*, "Accurate Prediction of Photon-Detection-Probability based on the 2-D Dead-Space Model for SPADs," *IEEE Sens J*, Jan. 2022, doi: 10.1109/JSEN.2022.3226237.
- [77] C. H. Liu, C. A. Hsien, and S. Di Lin, "2-D Photon-Detection-Probability Simulation and a Novel Guard-Ring Design for Small CMOS Single-Photon Avalanche Diodes," *IEEE Trans Electron Devices*, vol. 69, no. 6, pp. 2873–2878, Jun. 2022, doi: 10.1109/TED.2021.3119264.
- [78] T. Knežević, L. Nanver, T. Suligoj, and L. K. Nanver, "2D Dark-Count-Rate Modeling of PureB Single-Photon Avalanche Diodes in a TCAD Environment," *SPIE* vol. 10526, no. 23, pp. 266–275, Feb. 2018, doi: 10.1117/12.2290757.
- [79] Y. Xu, P. Xiang, and X. Xie, "Comprehensive Understanding of Dark Count Mechanisms of Single-Photon Avalanche Diodes Fabricated in Deep Sub-Micron CMOS Technologies," *Solid State Electron*, vol. 129, pp. 168–174, Mar. 2017, doi: 10.1016/J.SSE.2016.11.009.
- [80] Y. Kang, H. X. Lu, Y. H. Lo, D. S. Bethune, and W. P. Risk, "Dark Count Probability and Quantum Efficiency of Avalanche Photodiodes for Single-Photon Detection," *Appl Phys Lett*, vol. 83, no. 14, pp. 2955, Sep. 2003, doi: 10.1063/1.1616666.
- [81] M. J. Lee *et al.*, "High-Performance Back-Illuminated Three-Dimensional Stacked Single-Photon Avalanche Diode Implemented in 45-nm CMOS Technology," *IEEE Journal of Selected Topics in Quantum Electronics*, vol. 24, no. 6, Nov. 2018, doi: 10.1109/JSTQE.2018.2827669.
- [82] A. Ronchini Ximenes, P. Padmanabhan, M. J. Lee, Y. Yamashita, D. N. Yaung, and E. Charbon, "A Modular, Direct Time-of-Flight Depth Sensor in 45/65-nm 3-D-Stacked CMOS Technology," *IEEE J Solid-State Circuits*, vol. 54, no. 11, pp. 3203–3214, Nov. 2019, doi: 10.1109/JSSC.2019.2938412.
- [83] F. Gramuglia *et al.*, "Engineering Breakdown Probability Profile for PDP and DCR Optimization in a SPAD Fabricated in a Standard 55 nm BCD Process," *IEEE Journal of Selected Topics in Quantum Electronics*, vol. 28, no. 2, 2022, doi: 10.1109/JSTQE.2021.3114346.
- [84] J. Zhao *et al.*, "On Analog Silicon Photomultipliers in Standard 55-nm BCD Technology for LiDAR Applications," *IEEE Journal of Selected Topics in Quantum Electronics*, vol. 28, no. 5, 2022, doi: 10.1109/JSTQE.2022.3161089.
- [85] Y. Liu *et al.*, "A Wide Spectral Response Single Photon Avalanche Diode for Backside-Illumination in 55-nm CMOS Process," *IEEE Trans Electron Devices*, vol. 69, no. 9, pp. 5041–5047, Sep. 2022, doi: 10.1109/TED.2022.3194488.

- [86] F. Nolet *et al.*, “Quenching Circuit and SPAD Integrated in CMOS 65 nm with 7.8 ps FWHM Single Photon Timing Resolution,” *Instruments* 2018, vol. 2, no. 4, p. 19, Sep. 2018, doi: 10.3390/INSTRUMENTS2040019.
- [87] O. Kumagai *et al.*, “A 189x600 Back-Illuminated Stacked SPAD Direct Time-of-Flight Depth Sensor for Automotive LiDAR Systems,” *Dig Tech Pap IEEE Int Solid State Circuits Conf*, vol. 64, pp. 110–112, Feb. 2021, doi: 10.1109/ISSCC42613.2021.9365961.
- [88] S. Shimada *et al.*, “A SPAD Depth Sensor Robust Against Ambient Light: The Importance of Pixel Scaling and Demonstration of a 2.5 μ m Pixel with 21.8% PDE at 940nm,” pp. 37.3.1-37.3.4, Jan. 2023, doi: 10.1109/IEDM45625.2022.10019414.
- [89] I. Vornicu, F. Bandi, R. Carmona-Galan, and A. Rodriguez-Vazquez, “Low-Noise and High-Efficiency Near-IR SPADs in 110nm CIS Technology,” *European Solid-State Device Research Conference*, vol. 2019-September, pp. 250–253, Sep. 2019, doi: 10.1109/ESSDERC.2019.8901757.
- [90] I. Vornicu, J. M. López-Martínez, F. N. Bandi, R. C. Galán, and Á. Rodríguez-Vázquez, “Design of High-Efficiency SPADs for LiDAR Applications in 110nm CIS Technology,” *IEEE Sens J*, vol. 21, no. 4, pp. 4776–4785, Feb. 2021, doi: 10.1109/JSEN.2020.3032106.
- [91] M.-J. Lee, U. Karaca, E. Kizilkan, C. Bruschini, and E. Charbon, “A 73% Peak PDP Single-Photon Avalanche Diode Implemented in 110 nm CIS Technology with Doping Compensation,” *IEEE Journal of Selected Topics in Quantum Electronics*, pp. 1–10, 2023, doi: 10.1109/JSTQE.2023.3288674.
- [92] A. T. Erdogan *et al.*, “A CMOS SPAD Line Sensor with Per-Pixel Histogramming TDC for Time-Resolved Multispectral Imaging,” *IEEE J Solid-State Circuits*, vol. 54, no. 6, pp. 1705–1719, Jun. 2019, doi: 10.1109/JSSC.2019.2894355.
- [93] D. Morrison, S. Kennedy, D. Delic, M. R. Yuce, and J. M. Redoute, “A 64 \times 64 SPAD Flash LIDAR Sensor Using a Triple Integration Timing Technique with 1.95 mm Depth Resolution,” *IEEE Sens J*, vol. 21, no. 10, pp. 11361–11373, May 2021, doi: 10.1109/JSEN.2020.3030788.
- [94] F. Severini, I. Cusini, D. Berretta, K. Pasquinelli, A. Incoronato, and F. Villa, “SPAD Pixel with Sub-NS Dead-Time for High-Count Rate Applications,” *IEEE Journal of Selected Topics in Quantum Electronics*, vol. 28, no. 2, 2022, doi: 10.1109/JSTQE.2021.3124825.
- [95] C. Zhang, S. Lindner, I. M. Antolovic, M. Wolf, and E. Charbon, “A CMOS SPAD Imager with Collision Detection and 128 Dynamically Reallocating TDCs for Single-Photon Counting and 3D Time-of-Flight Imaging,” *Sensors* 2018, vol. 18, no. 11, p. 4016, Nov. 2018, doi: 10.3390/S18114016.
- [96] K. Morimoto, K. Morimoto, and E. Charbon, “High fill-factor miniaturized SPAD arrays with a guard-ring-sharing technique,” *Optics Express*, vol. 28, no. 9, pp. 13068–13080, Apr. 2020, doi: 10.1364/OE.389216.
- [97] I. M. Morimoto *et al.*, “Megapixel time-gated SPAD image sensor for 2D and 3D imaging applications,” *Optica*, vol. 7, no. 4, pp. 346–354, Apr. 2020, doi: 10.1364/OPTICA.386574.
- [98] F. Gramuglia, M. Lo Wu, C. Bruschini, M. J. Lee, and E. Charbon, “A Low-Noise CMOS SPAD Pixel with 12.1 Ps SPTR and 3 Ns Dead Time,” *IEEE Journal of Selected Topics in Quantum Electronics*, vol. 28, no. 2, 2022, doi: 10.1109/JSTQE.2021.3088216.

- [99] F. Acerbi, G. Paternoster, A. Gola, N. Zorzi, and C. Piemonte, “Silicon Photomultipliers and Single-Photon Avalanche Diodes with Enhanced NIR Detection Efficiency at FBK,” *Nucl Instrum Methods Phys Res A*, vol. 912, pp. 309–314, Dec. 2018, doi: 10.1016/J.NIMA.2017.11.098.
- [100] F. Ceccarelli, G. Acconcia, I. Labanca, A. Gulinatti, M. Ghioni, and I. Rech, “152-dB Dynamic Range with a Large-Area Custom-Technology Single-Photon Avalanche Diode,” *IEEE Photonics Technology Letters*, vol. 30, no. 4, pp. 391–394, Feb. 2018, doi: 10.1109/LPT.2018.2792781.
- [101] R. Tobin *et al.*, “Long-range depth profiling of camouflaged targets using single-photon detection,” *SPIE*, vol. 57, no. 3, p. 031303, Dec. 2017, doi: 10.1117/1.OE.57.3.031303.
- [102] P. Vines *et al.*, “High Performance Planar Germanium-on-Silicon Single-Photon Avalanche Diode Detectors,” *Nature Communications* 2019 10:1, vol. 10, no. 1, pp. 1–9, Mar. 2019, doi: 10.1038/s41467-019-08830-w.
- [103] C. H. Jang, C. S. Kim, K. C. Jo, and M. Sunwoo, “Design Factor Optimization of 3D Flash Lidar Sensor based on Geometrical Model for Automated Vehicle and Advanced Driver Assistance System Applications,” *International Journal of Automotive Technology*, vol. 18, no. 1, pp. 147–156, Feb. 2017, doi: 10.1007/S12239-017-0015-7/METRICS.
- [104] B. Behroozpour, P. A. M. Sandborn, M. C. Wu, and B. E. Boser, “Lidar System Architectures and Circuits,” *IEEE Communications Magazine*, vol. 55, no. 10, pp. 135–142, Oct. 2017, doi: 10.1109/MCOM.2017.1700030.
- [105] N. Li *et al.*, “A Progress Review on Solid-State LiDAR and Nanophotonics-Based LiDAR Sensors,” *Laser Photon Rev*, vol. 16, no. 11, p. 2100511, Nov. 2022, doi: 10.1002/LPOR.202100511.
- [106] A. Tsikouras, P. Peronio, I. Rech, N. Hirmiz, M. J. Deen, and Q. Fang, “Characterization of SPAD Array for Multifocal High-Content Screening Applications,” *Photonics* 2016, vol. 3, no. 4, p. 56, Oct. 2016, doi: 10.3390/PHOTONICS3040056.
- [107] S. Cova, A. Longoni, and A. Andreoni, “Towards Picosecond Resolution with Single-Photon Avalanche Diodes,” *Review of Scientific Instruments*, vol. 52, no. 3, p. 408, Jun. 1998, doi: 10.1063/1.1136594.
- [108] “Sentaurus™ Device User Guide Version R-2020.09, September 2020.”
- [109] “Sentaurus™ Structure Editor User Guide Version R-2020.09, September 2020.”
- [110] N. Faramarzpour, M. J. Deen, S. Shirani, and Q. Fang, “Fully Integrated Single Photon Avalanche Diode Detector in Standard CMOS 0.18- μm Technology,” *IEEE Trans Electron Devices*, vol. 55, no. 3, pp. 760–767, Mar. 2008, doi: 10.1109/TED.2007.914839.
- [111] A. Arbat *et al.*, “High Voltage vs. High Integration: A Comparison Between CMOS Technologies for SPAD Cameras,” *SPIE*, vol. 7780, pp. 349–356, Aug. 2010, doi: 10.1117/12.860482.
- [112] G. A. M. Hurkx, D. B. M. Klaassen, and M. P. G. Knuvers, “A New Recombination Model for Device Simulation Including Tunneling,” *IEEE Trans Electron Devices*, vol. 39, no. 2, pp. 331–338, 1992, doi: 10.1109/16.121690.
- [113] G. A. M. Hurkx, H. C. De Graaff, W. J. Kloosterman, and M. P. G. Knuvers, “A New Analytical Diode Model Including Tunneling and Avalanche Breakdown,” *IEEE Trans Electron Devices*, vol. 39, no. 9, pp. 2090–2098, 1992, doi: 10.1109/16.155882.

- [114] W. J. Kindt and H. W. Van Zeijl, "Modelling and Fabrication of Geiger Mode Avalanche Photodiodes," *IEEE Trans Nucl Sci*, vol. 45, no. 3 PART 1, pp. 715–719, 1998, doi: 10.1109/23.682621.
- [115] A. Panglosse, P. Martin-Gonthier, O. Marcelot, C. Virmontois, O. Saint-Pe, and P. Magnan, "Dark Count Rate Modeling in Single-Photon Avalanche Diodes," *IEEE Transactions on Circuits and Systems I: Regular Papers*, vol. 67, no. 5, pp. 1507–1515, May 2020, doi: 10.1109/TCSI.2020.2971108.
- [116] M. Sicre *et al.*, "Dark Count Rate in Single-Photon Avalanche Diodes: Characterization and Modeling Study," *European Solid-State Device Research Conference*, vol. 2021-September, pp. 143–146, 2021, doi: 10.1109/ESSDERC53440.2021.9631797.
- [117] L. Pancheri, D. Stoppa, and G. F. Dalla Betta, "Characterization and Modeling of Breakdown Probability in Sub-Micrometer CMOS SPADs," *IEEE Journal of Selected Topics in Quantum Electronics*, vol. 20, no. 6, pp. 328–335, Nov. 2014, doi: 10.1109/JSTQE.2014.2327791.
- [118] E. A. G. Webster, L. A. Grant, and R. K. Henderson, "A High-Performance Single-Photon Avalanche Diode in 130-nm CMOS Imaging Technology," *IEEE Electron Device Letters*, vol. 33, no. 11, pp. 1589–1591, 2012, doi: 10.1109/LED.2012.2214760.
- [119] E. O. Kane, "Theory of Tunneling," *J Appl Phys*, vol. 32, no. 1, pp. 83, Jun. 2004, doi: 10.1063/1.1735965.
- [120] L. Qi, K. R. C. Mok, M. Aminian, E. Charbon, and L. K. Nanver, "UV-Sensitive Low Dark-Count PureB Single-Photon Avalanche Diode," *IEEE Trans Electron Devices*, vol. 61, no. 11, pp. 3768–3774, Nov. 2014, doi: 10.1109/TED.2014.2351576.
- [121] A. Schenk, "Finite-Temperature Full Random-Phase Approximation Model of Band Gap Narrowing for Silicon Device Simulation," *J Appl Phys*, vol. 84, no. 7, p. 3684, Oct. 1998, doi: 10.1063/1.368545.
- [122] R. Van Overstraeten and H. De Man, "Measurement of the Ionization Rates in Diffused Silicon P-N Junctions," *Solid State Electron*, vol. 13, no. 5, pp. 583–608, May 1970, doi: 10.1016/0038-1101(70)90139-5.
- [123] Y. Okuto and C. R. Crowell, "Threshold Energy Effect on Avalanche Breakdown Voltage in Semiconductor Junctions," *Solid State Electron*, vol. 18, no. 2, pp. 161–168, Feb. 1975, doi: 10.1016/0038-1101(75)90099-4.
- [124] T. Lackner, "Avalanche Multiplication in Semiconductors: A Modification of Chynoweth's Law," *Solid State Electron*, vol. 34, no. 1, pp. 33–42, Jan. 1991, doi: 10.1016/0038-1101(91)90197-7.
- [125] M. C. Vecchi and M. Rudan, "Modeling Electron and Hole Transport with Full-Band Structure Effects by Means of the Spherical-Harmonics Expansion of the BTE," *IEEE Trans Electron Devices*, vol. 45, no. 1, pp. 230–238, 1998, doi: 10.1109/16.658836.
- [126] A. G. Chynoweth, "Ionization Rates for Electrons and Holes in Silicon," *Physical Review*, vol. 109, no. 5, p. 1537, Mar. 1958, doi: 10.1103/PhysRev.109.1537.
- [127] C. L. Forrest Ma, M. J. Deen, L. E. Tarof, and J. C. H. Yu, "Temperature Dependence of Breakdown Voltages in Separate Absorption, Grading, Charge, and Multiplication InP/InGaAs Avalanche Photodiodes," *IEEE Trans Electron Devices*, vol. 42, no. 5, pp. 810–818, 1995, doi: 10.1109/16.381974.
- [128] C. L. F. Ma, M. J. Deen, and L. E. Tarof, "Multiplication in Separate Absorption, Grading, Charge, and Multiplication InP-InGaAs Avalanche Photodiodes," *IEEE J Quantum Electron*, vol. 31, no. 11, pp. 2078–2089, 1995, doi: 10.1109/3.469291.

- [129] A. Bandyopadhyay, M. Jamal Deen, L. E. Tarof, and W. Clark, “A Simplified Approach to Time-Domain Modeling of Avalanche Photodiodes,” *IEEE J Quantum Electron*, vol. 34, no. 4, pp. 691–699, Apr. 1998, doi: 10.1109/3.663452.
- [130] Y. Okuto and C. R. Crowell, “Ionization Coefficients in Semiconductors: A Nonlocalized Property,” *Phys Rev B*, vol. 10, no. 10, p. 4284, Nov. 1974, doi: 10.1103/PhysRevB.10.4284.
- [131] M. C. Teich and B. E. A. Saleh, “Effect of Dead Space on Gain and Noise of Double-Carrier-Multiplication Avalanche Photodiodes,” *IEEE Trans Electron Devices*, vol. 39, no. 3, pp. 546–552, 1992, doi: 10.1109/16.123476.
- [132] D. A. Ramirez, M. M. Hayat, A. S. Huntington, and G. M. Williams, “Non-Local Model for the Spatial Distribution of Impact Ionization Events in Avalanche Photodiodes,” *IEEE Photonics Technology Letters*, vol. 26, no. 1, pp. 25–28, Jan. 2014, doi: 10.1109/LPT.2013.2289974.
- [133] J. S. Cheong, M. M. Hayat, X. Zhou, and J. P. R. David, “Relating the Experimental Ionization Coefficients in Semiconductors to the Nonlocal Ionization Coefficients,” *IEEE Trans Electron Devices*, vol. 62, no. 6, pp. 1946–1952, Jun. 2015, doi: 10.1109/TED.2015.2422789.
- [134] A. Panglosse, P. Martin-Gonthier, O. Marcelot, C. Virmontois, O. Saint-Pé, and P. Magnan, “Modeling, Simulation Methods and Characterization of Photon Detection Probability in CMOS-SPAD,” *Sensors 2021*, vol. 21, no. 17, p. 5860, Aug. 2021, doi: 10.3390/S21175860.
- [135] C. A. Hsieh, C. M. Tsai, B. Y. Tsui, B. J. Hsiao, and S. Di Lin, “Photon-Detection-Probability Simulation Method for CMOS Single-Photon Avalanche Diodes,” *Sensors 2020*, vol. 20, no. 2, p. 436, Jan. 2020, doi: 10.3390/S20020436.
- [136] H. Mahmoudi, S. S. K. Poushi, B. Steindl, M. Hofbauer, and H. Zimmermann, “Optical and Electrical Characterization and Modeling of Photon Detection Probability in CMOS Single-Photon Avalanche Diodes,” *IEEE Sens J*, vol. 21, no. 6, pp. 7572–7580, Mar. 2021, doi: 10.1109/JSEN.2021.3051365.
- [137] H. Zimmermann, H. Mahmoudi, S. S. K. Poushi, B. Steindl, and M. Hofbauer, “Photon Detection Probability Enhancement using an Anti-Reflection Coating in CMOS-based SPADs,” *Applied Optics*, vol. 60, no. 25, pp. 7815–7820, Sep. 2021, doi: 10.1364/AO.432219.
- [138] Y. Xu, P. Xiang, X. Xie, and Y. Huang, “A New Modeling and Simulation Method for Important Statistical Performance Prediction of Single Photon Avalanche Diode Detectors,” *Semicond Sci Technol*, vol. 31, no. 6, p. 065024, May 2016, doi: 10.1088/0268-1242/31/6/065024.
- [139] A. Gulinatti, I. Rech, M. Assanelli, M. Ghioni, and S. Cova, “A Physically Based Model for Evaluating the Photon Detection Efficiency and the Temporal Response of SPAD Detectors,” *SPIE*, vol. 58, no. 3–4, pp. 210–224, Jan. 2010, doi: 10.1080/09500340.2010.536590.
- [140] A. Gulinatti *et al.*, “Modeling Photon Detection Efficiency and Temporal Response of Single Photon Avalanche Diodes,” *Photon Counting Applications, Quantum Optics, and Quantum Information Transfer and Processing II*, vol. 7355, pp. 161–177, May 2009, doi: 10.1117/12.820661.
- [141] M. J. Deen and P. K. Basu, *Silicon Photonics: Fundamentals and Devices*. John Wiley and Sons Ltd, 2012. doi: 10.1002/9781119945161.
- [142] S. S. Kohneh Poushi, H. Mahmoudi, B. Steindl, M. Hofbauer, and H. Zimmermann, “Comprehensive Modeling of Photon Detection Probability in CMOS-based SPADs,”

- Proceedings of IEEE Sensors*, vol. 2020-October, Oct. 2020, doi: 10.1109/SENSORS47125.2020.9278771.
- [143] M. Mazzillo *et al.*, “Single-Photon Avalanche Photodiodes with Integrated Quenching Resistor,” *Nucl Instrum Methods Phys Res A*, vol. 591, no. 2, pp. 367–373, Jun. 2008, doi: 10.1016/J.NIMA.2008.03.011.
- [144] G. Bonanno *et al.*, “Precision Measurements of Photon Detection Efficiency for SiPM Detectors,” *Nucl Instrum Methods Phys Res A*, vol. 610, no. 1, pp. 93–97, Oct. 2009, doi: 10.1016/J.NIMA.2009.05.117.
- [145] J. A. Richardson, L. A. Grant, and R. K. Henderson, “Low Dark Count Single-Photon Avalanche Diode Structure Compatible with Standard Nanometer Scale CMOS Technology,” *IEEE Photonics Technology Letters*, vol. 21, no. 14, pp. 1020–1022, Jul. 2009, doi: 10.1109/LPT.2009.2022059.
- [146] C. Niclass, M. Gersbach, R. Henderson, L. Grant, and E. Charbon, “A Single Photon Avalanche Diode Implemented in 130-nm CMOS Technology,” *IEEE Journal on Selected Topics in Quantum Electronics*, vol. 13, no. 4, pp. 863–869, Jul. 2007, doi: 10.1109/JSTQE.2007.903854.
- [147] E. A. G. Webster, J. A. Richardson, L. A. Grant, D. Renshaw, and R. K. Henderson, “A Single-Photon Avalanche Diode in 90-nm CMOS Imaging Technology with 44% Photon Detection Efficiency at 690 nm,” *IEEE Electron Device Letters*, vol. 33, no. 5, pp. 694–696, May 2012, doi: 10.1109/LED.2012.2187420.
- [148] D. Stoppa, D. Mosconi, L. Pancheri, and L. Gonzo, “Single-Photon Avalanche Diode CMOS Sensor for Time-Resolved Fluorescence Measurements,” *IEEE Sens J*, vol. 9, no. 9, pp. 1084–1090, Sep. 2009, doi: 10.1109/JSEN.2009.2025581.
- [149] E. Charbon, H. J. Yoon, and Y. Maruyama, “A Geiger mode APD Fabricated in Standard 65nm CMOS Technology,” *Technical Digest - International Electron Devices Meeting, IEDM*, pp. 27.5.1-27.5.4, 2013, doi: 10.1109/IEDM.2013.6724705.
- [150] M. A. Wolff *et al.*, “Broadband Waveguide-Integrated Superconducting Single-Photon Detectors with High System Detection Efficiency,” *Appl Phys Lett*, vol. 118, no. 15, p. 154004, Apr. 2021, doi: 10.1063/5.0046057.
- [151] M. Cohen *et al.*, “Fully optimized Cu based Process with Dedicated Cavity Etch for 1.75 μ m and 1.45 μ m Pixel Pitch CMOS Image Sensors,” *Technical Digest - International Electron Devices Meeting, IEDM*, 2006, doi: 10.1109/IEDM.2006.346976.
- [152] X. Qian, W. Jiang, and M. J. Deen, “Enhanced Photon Detection Probability Model for Single-Photon Avalanche Diodes in TCAD with Machine Learning,” *2022 IEEE International IOT, Electronics and Mechatronics Conference, IEMTRONICS 2022*, 2022, doi: 10.1109/IEMTRONICS55184.2022.9795802.
- [153] O. Marinov, M. J. Deen, and J. A. Jiménez-Tejada, “Low-Frequency Noise in Downscaled Silicon Transistors: Trends, Theory and Practice,” *Phys Rep*, vol. 990, pp. 1–179, Dec. 2022, doi: 10.1016/J.PHYSREP.2022.06.005.
- [154] W. J. Kindt and H. W. Van Zeijl, “Modelling and Fabrication of Geiger Mode Avalanche Photodiodes,” *IEEE Trans Nucl Sci*, vol. 45, no. 3 PART 1, pp. 715–719, 1998, doi: 10.1109/23.682621.
- [155] G. A. M. Hurkx, H. C. De Graaff, W. J. Kloosterman, and M. P. G. Knuvers, “A New Analytical Diode Model Including Tunneling and Avalanche Breakdown,” *IEEE Trans Electron Devices*, vol. 39, no. 9, pp. 2090–2098, 1992, doi: 10.1109/16.155882.

- [156] G. A. M. Hurkx, D. B. M. Klaassen, and M. P. G. Knuvers, "A New Recombination Model for Device Simulation Including Tunneling," *IEEE Trans Electron Devices*, vol. 39, no. 2, pp. 331–338, 1992, doi: 10.1109/16.121690.
- [157] A. Panglosse, P. Martin-Gonthier, O. Marcelot, C. Virmontois, O. Saint-Pe, and P. Magnan, "Dark Count Rate Modeling in Single-Photon Avalanche Diodes," *IEEE Transactions on Circuits and Systems I: Regular Papers*, vol. 67, no. 5, pp. 1507–1515, May 2020, doi: 10.1109/TCSI.2020.2971108.
- [158] X. Qian, W. Jiang, A. Elsharabasy, and M. J. Deen, "Modeling for Single-Photon Avalanche Diodes: State-of-the-Art and Research Challenges," *Sensors* 2023, vol. 23, no. 7, p. 3412, Mar. 2023, doi: 10.3390/S23073412.
- [159] D. L. Bailey, D. W. Townsend, P. E. Valk, and M. N. Maisey, *Positron Emission Tomography*. 2005. Accessed: Mar. 11, 2023. [Online]. Available: <https://link.springer.com/content/pdf/10.1007/b136169.pdf>
- [160] H. S. Bennett and C. L. Wilson, "Statistical Comparisons of Data on Band-Gap Narrowing in Heavily Doped Silicon: Electrical and Optical Measurements," *J Appl Phys*, vol. 55, no. 10, pp. 3582–3587, May 1984, doi: 10.1063/1.332950.
- [161] C. Canali, G. Majni, R. Minder, and G. Ottaviani, "Electron and Hole Drift Velocity Measurements in Silicon and Their Empirical Relation to Electric Field and Temperature," *IEEE Trans Electron Devices*, vol. 22, no. 11, pp. 1045–1047, 1975, doi: 10.1109/T-ED.1975.18267.
- [162] A. Schenk, "Rigorous Theory and Simplified Model of the Band-to-Band Tunneling in Silicon," *Solid State Electron*, vol. 36, no. 1, pp. 19–34, Jan. 1993, doi: 10.1016/0038-1101(93)90065-X.
- [163] "II. SPAD TEST STRUCTURE DESCRIPTION", Accessed: Jul. 18, 2023. [Online]. Available: <https://www.imagesensors.org/Past%20Workshops/2017%20Workshop/2017%20Papers/R21.pdf>
- [164] N. Kandpal, A. Singh, and A. Agarwal, "A Machine Learning Driven PVT-Robust VCO with Enhanced Linearity Range," *Circuits Syst Signal Process*, pp. 1–18, Mar. 2022, doi: 10.1007/S00034-022-02001-X/TABLES/3.
- [165] J. Chen *et al.*, "Powernet: SOI Lateral Power Device Breakdown Prediction with Deep Neural Networks," *IEEE Access*, vol. 8, pp. 25372–25382, 2020, doi: 10.1109/ACCESS.2020.2970966.
- [166] K. Ko, J. K. Lee, M. Kang, J. Jeon, and H. Shin, "Prediction of Process Variation Effect for Ultra scaled GAA Vertical FET Devices Using a Machine Learning Approach," *IEEE Trans Electron Devices*, vol. 66, no. 10, pp. 4474–4477, Oct. 2019, doi: 10.1109/TED.2019.2937786.
- [167] C. W. Teo, K. L. Low, V. Narang, and A. V. Y. Thean, "TCAD-Enabled Machine Learning Defect Prediction to Accelerate Advanced Semiconductor Device Failure Analysis," *International Conference on Simulation of Semiconductor Processes and Devices, SISPAD*, vol. 2019-September, Sep. 2019, doi: 10.1109/SISPAD.2019.8870440.
- [168] H. Mahmoudi, S. S. K. Poushi, B. Steindl, M. Hofbauer, and H. Zimmermann, "Optical and Electrical Characterization and Modeling of Photon Detection Probability in CMOS Single-Photon Avalanche Diodes," *IEEE Sens J*, vol. 21, no. 6, pp. 7572–7580, Mar. 2021, doi: 10.1109/JSEN.2021.3051365.
- [169] H. Zimmermann, H. Mahmoudi, S. S. K. Poushi, B. Steindl, and M. Hofbauer, "Photon Detection Probability Enhancement using an Anti-Reflection Coating in

- CMOS-based SPADs,” *Applied Optics*, vol. 60, no. 25, pp. 7815–7820, Sep. 2021, doi: 10.1364/AO.432219.
- [170] D. P. Palubiak and M. J. Deen, “CMOS SPADs: Design Issues and Research Challenges for Detectors, Circuits, and Arrays,” *IEEE Journal of Selected Topics in Quantum Electronics*, vol. 20, no. 6, pp. 409–426, Nov. 2014, doi: 10.1109/JSTQE.2014.2344034.
- [171] V. Savuskan, M. Javitt, G. Visokolov, I. Brouk, and Y. Nemirovsky, “Selecting Single Photon Avalanche Diode (SPAD) Passive-Quenching Resistance: An Approach,” *IEEE Sens J*, vol. 13, no. 6, pp. 2322–2328, 2013, doi: 10.1109/JSEN.2013.2253603.
- [172] F. Zappa, A. Tosi, A. Dalla Mora, and S. Tisa, “SPICE Modeling of Single Photon Avalanche Diodes,” *Sens Actuators A Phys*, vol. 153, no. 2, pp. 197–204, Aug. 2009, doi: 10.1016/j.sna.2009.05.007.
- [173] W. Jiang, R. Scott, and M. J. Deen, “Differential Quench and Reset Circuit for Single-Photon Avalanche Diodes,” *Journal of Lightwave Technology*, vol. 39, no. 22, pp. 7334–7342, Nov. 2021, doi: 10.1109/JLT.2021.3111119.
- [174] A. Lacaíta, C. Samori, F. Zappa, M. Ghioni, and S. Cova, “Avalanche Photodiodes and Quenching Circuits for Single-Photon Detection,” *Applied Optics*, vol. 35, no. 12, pp. 1956–1976, Apr. 1996, doi: 10.1364/AO.35.001956.
- [175] C. H. Liu, C. A. Hsien, and S. Di Lin, “2-D Photon-Detection-Probability Simulation and a Novel Guard-Ring Design for Small CMOS Single-Photon Avalanche Diodes,” *IEEE Trans Electron Devices*, vol. 69, no. 6, pp. 2873–2878, June 2022, doi: 10.1109/TED.2021.3119264.
- [176] D. P. Palubiak, Z. Li, and M. J. Deen, “Afterpulsing Characteristics of Free-Running and Time-Gated Single-Photon Avalanche Diodes in 130-nm CMOS,” *IEEE Trans Electron Devices*, vol. 62, no. 11, pp. 3727–3733, Nov. 2015, doi: 10.1109/TED.2015.2475126.
- [177] D. Palubiak, “CMOS Single Photon Avalanche Diodes and Time-to-Digital Converters for Time-Resolved Fluorescence Analysis,” 2016, Accessed: Jul. 29, 2023. [Online]. Available: <https://macsphere.mcmaster.ca/handle/11375/18695>
- [178] R. Scott, “Design of a Time-to-Digital Converter and Multi-Time-Gated SPAD Arrays Towards Biomedical Imaging Applications,” 2021, Accessed: Jul. 29, 2023. [Online]. Available: <https://macsphere.mcmaster.ca/handle/11375/26864>
- [179] P.-H. Chen, C.-H. Liu, C.-M. Tsai, T.-H. Sang, G. Lin, and S.-D. Lin, “Modeling and Verification of a Photon-Counting LiDAR,” *ITE Technical Report*, vol. 46, no. 41, December 2022, doi: 10.7567/ssdm.2017.g-3-03.
- [180] P. Padmanabhan, C. Zhang, and E. Charbon, “Modeling and Analysis of a Direct Time-of-Flight Sensor Architecture for LiDAR Applications,” *Sensors* 2019, vol. 19, no. 24, p. 5464, Dec. 2019, doi: 10.3390/S19245464.
- [181] J. Zhao, Y. Li, B. Zhu, W. Deng, and B. Sun, “Method and Applications of Lidar Modeling for Virtual Testing of Intelligent Vehicles,” *IEEE Transactions on Intelligent Transportation Systems*, vol. 22, no. 5, pp. 2990–3000, May 2021, doi: 10.1109/TITS.2020.2978438.
- [182] S. S. Kohneh Poushi, H. Mahmoudi, B. Steindl, M. Hofbauer, and H. Zimmermann, “Comprehensive Modeling of Photon Detection Probability in CMOS-based SPADs,” *Proceedings of IEEE Sensors*, vol. 2020-October, Oct. 2020, doi: 10.1109/SENSORS47125.2020.9278771.

Appendix A

Copyright Permission

A Backside-Illuminated Charge-Focusing Silicon SPAD With Enhanced Near-Infrared Sensitivity

Author: Edward Van Sieleghem

Publication: IEEE Transactions on Electron Devices

Publisher: IEEE

Date: March 2022

Copyright © 2022, IEEE

Thesis / Dissertation Reuse

The IEEE does not require individuals working on a thesis to obtain a formal reuse license, however, you may print out this statement to be used as a permission grant:

Requirements to be followed when using any portion (e.g., figure, graph, table, or textual material) of an IEEE copyrighted paper in a thesis:

- 1) In the case of textual material (e.g., using short quotes or referring to the work within these papers) users must give full credit to the original source (author, paper, publication) followed by the IEEE copyright line © 2011 IEEE.
- 2) In the case of illustrations or tabular material, we require that the copyright line © [Year of original publication] IEEE appear prominently with each reprinted figure and/or table.
- 3) If a substantial portion of the original paper is to be used, and if you are not the senior author, also obtain the senior author's approval.

Requirements to be followed when using an entire IEEE copyrighted paper in a thesis:

- 1) The following IEEE copyright/ credit notice should be placed prominently in the references: © [year of original publication] IEEE. Reprinted, with permission, from [author names, paper title, IEEE publication title, and month/year of publication]
- 2) Only the accepted version of an IEEE copyrighted paper can be used when posting the paper or your thesis online.

3) In placing the thesis on the author's university website, please display the following message in a prominent place on the website: In reference to IEEE copyrighted material which is used with permission in this thesis, the IEEE does not endorse any of [university/educational entity's name goes here]'s products or services. Internal or personal use of this material is permitted. If interested in reprinting/republishing IEEE copyrighted material for advertising or promotional purposes or for creating new collective works for resale or redistribution, please go to http://www.ieee.org/publications_standards/publications/rights/rights_link.html to learn how to obtain a License from RightsLink.

If applicable, University Microfilms and/or ProQuest Library, or the Archives of Canada may supply single copies of the dissertation.

Modeling for Single-Photon Avalanche Diodes: State-of-the-Art and Research Challenges

Author: Xuanyu Qian

Publication: MDPI Sensors

Sensors is an open access journal and we follow the conditions of the Creative Commons Attribution license (<http://creativecommons.org/licenses/by/4.0/>), which provides that published material can be re - used without obtaining permission as long as a correct citation to the original publication is given.

Single Photon Detectors for Automotive LiDAR Applications: State-of-the-Art and Research Challenges

Author: Xuanyu Qian

Publication: IEEE Journal of Selected Topics in Quantum Electronics

Publisher: IEEE

Date: Dec 31, 1969

Copyright © 1969, IEEE

Thesis / Dissertation Reuse

The IEEE does not require individuals working on a thesis to obtain a formal reuse license, however, you may print out this statement to be used as a permission grant: Requirements to be followed when using any portion (e.g., figure, graph, table, or textual material) of an IEEE copyrighted paper in a thesis:

- 1) In the case of textual material (e.g., using short quotes or referring to the work within these papers) users must give full credit to the original source (author, paper, publication) followed by the IEEE copyright line © 2011 IEEE.
- 2) In the case of illustrations or tabular material, we require that the copyright line © [Year of original publication] IEEE appear prominently with each reprinted figure and/or table.
- 3) If a substantial portion of the original paper is to be used, and if you are not the senior author, also obtain the senior author's approval.

Requirements to be followed when using an entire IEEE copyrighted paper in a thesis:

- 1) The following IEEE copyright/ credit notice should be placed prominently in the references: © [year of original publication] IEEE. Reprinted, with permission, from [author names, paper title, IEEE publication title, and month/year of publication]
- 2) Only the accepted version of an IEEE copyrighted paper can be used when posting the paper or your thesis online.
- 3) In placing the thesis on the author's university website, please display the following message in a prominent place on the website: In reference to IEEE copyrighted material which is used with permission in this thesis, the IEEE does not endorse any of [university/educational entity's name goes here]'s products or services. Internal or personal use of this material is permitted. If interested in reprinting/republishing IEEE copyrighted material for advertising or promotional purposes or for creating new collective works for resale or redistribution, please go to http://www.ieee.org/publications_standards/publications/rights/rights_link.html to learn how to obtain a License from RightsLink.

If applicable, University Microfilms and/or ProQuest Library, or the Archives of Canada may supply single copies of the dissertation.

Appendix B

Codes for Simulation Automation

Code for automation:

1. TCAD Automated Visualization (tcl codes)

For a specific simulation node (one streamline), note that the node number is automatically updated for different simulations. **(Comments)**

```
load_script_file/home/UserID/mydata/TED_2023/2D_Stuc_Simulation_testDoping/n1653_v1.s.tcl (Load specific script file at specific directory)
```

```
cd /home/ UserID /mydata/TED_2023/2D_Stuc_Simulation_testDoping (Open the design file)
```

```
load_file /home/ UserID /mydata/TED_2023/2D_Stuc_Simulation_testDoping/n1653_des.plt
```

```
create_plot -1d; select_plots {Plot_1} (create and select plots)
```

```
load_file /home/v56377/mydata/TED_2023/2D_Stuc_Simulation_testDoping/n1653_des.tdr
```

```
create_plot -dataset n1653_des_2
```

```
select_plots {Plot_n1653_des_2}
```

```
select_plots {Plot_n1653_des_2}
```

(Load structure and visualize the structure)

```
create_streamline -plot Plot_n1653_des_2 -field ElectricField-V -geom n1653_des_2 -point {0.2 0.2} -direction both -integ_initial_step 0.022 -integ_max_steps 53241 -integ_terminal_speed 0.01 -integ_max_propagation 1171.3 -dataset
```

(Create streamline following the electric field's direction)

```
set_field_prop eAlphaAvalanche -plot Plot_n1653_des_2 -geom n1653_des_2 -show_bands
```

```
extract_streamlines -plot Plot_n1653_des_2 {Streamline}
```

(Extract the electron impact ionization coefficient along the streamline)

```
create_curve -axisX Distance -axisY eAlphaAvalanche -dataset{Streamline(Plot_n1653_des_2)} -plot Plot_1
```

```
select_plots {Plot_1} (Visualize the extracted electron impact ionization coefficient)
```

```
export_curves {Curve_1} -plot Plot_1 -filename /home/ UserID
/mydata/TED_2023/CSVDATA_SingleLineTAT_dopingtest/ealpha5um-9v.csv -format csv
```

(Export the data to the excel file with user-defined naming style)

```
remove_plots {Plot_1}
```

(Remove the previous plot)

```
set_field_prop hAlphaAvalanche -plot Plot_n1653_des_2 -geom n1653_des_2 -show_bands
```

(Switch to the hole impact ionizations)

```
extract_streamlines -plot Plot_n1653_des_2 {Streamline}
```

```
create_plot -dataset Streamline(Plot_n1653_des_2)_2 -1d
```

```
create_curve -axisX Distance -axisY hAlphaAvalanche -dataset
{Streamline(Plot_n1653_des_2)_2} -plot Plot_Streamline(Plot_n1653_des_2)_2
```

```
export_curves {Curve_1} -plot Plot_Streamline(Plot_n1653_des_2)_2 -filename /home/
UserID /mydata/TED_2023/CSVDATA_SingleLineTAT_dopingtest/halpha5um-9v.csv -
format csv
```

(Export the data to the excel file with user-defined naming style)

```
remove_plots {Plot_Streamline(Plot_n1653_des_2)_2}
```

(Remove the previous plot)

```
set_field_prop srhRecombination -plot Plot_n1653_des_2 -geom n1653_des_2 -show_bands
```

(Switch to the Shockley-Read-hall generation rate)

```
extract_streamlines -plot Plot_n1653_des_2 {Streamline}
```

(Extract the SRH generation rate along the streamline)

```
create_curve -axisX Distance -axisY srhRecombination -dataset
{Streamline(Plot_n1653_des_2)_3} -plot Plot_Streamline(Plot_n1653_des_2)_3
```

```
export_curves {Curve_1} -plot Plot_Streamline(Plot_n1653_des_2)_3 -filename /home/
UserID /mydata/TED_2023/CSVDATA_SingleLineTAT_dopingtest/srh5um-9v.csv -format
csv
```

(Export the data to the excel file with user-defined naming style)

```
remove_plots {Plot_Streamline(Plot_n1653_des_2)_3} (Remove the previous plot)
```

```
set_field_prop Band2BandGeneration -plot Plot_n1653_des_2 -geom n1653_des_2 -
show_bands (Switch to the Band-to-Band generation rate)
```

```
extract_streamlines -plot Plot_n1653_des_2 {Streamline}
```

```
create_curve -axisX Distance -axisY Band2BandGeneration -dataset  
{Streamline(Plot_n1653_des_2)_4} -plot Plot_Streamline(Plot_n1653_des_2)_4
```

(Extract the BTBT generation rate along the streamline)

```
export_curves {Curve_1} -plot Plot_Streamline(Plot_n1653_des_2)_4 -filename /home/  
UserID/mydata/TED_2023/CSVDATA_SingleLineTAT_dopingtest/b2b5um-9v.csv -format  
csv. (Export the data to the excel file with user-defined naming style)
```

(End of the automated visualization in TCAD)

2. MATLAB codes for calculating triggering probability, DCR and PDP.

Please refer to: [MATLABCodes_2023](#)